



Lehrstuhl für Akustik Mobiler Systeme

Acoustic metamaterials and machinery noise: requirements, design, modelling, and experiments

Anton Melnikov

Vollständiger Abdruck der von der Fakultät für Maschinenwesen der Technischen Universität München zur Erlangung des akademischen Grades eines

Doktor-Ingenieurs (Dr.-Ing.)

genehmigten Dissertation.

Vorsitzender: Prof. Dr. Markus Zimmermann

Prüfer der Dissertation: 1. Prof. Dr.-Ing. Steffen Marburg
2. Assoc. Prof. Dr.-Ing. Jens Ahrens

Die Dissertation wurde am 16.04.2020 bei der Technischen Universität München eingereicht und durch die Fakultät für Maschinenwesen am 14.10.2020 angenommen.

In dedication to my parents,
Olga and Pavel Melnikov



"Silence" by Olga Melnikov

Abstract

This work contributes to the field of noise control and acoustic metamaterials. In following, the application of acoustic metamaterials to the stage machinery is studied, which includes an elaboration of noise requirements of stage machinery, the design of a metamaterial capsule for the reduction of noise emission from machines, and a theoretical and experimental investigation of the scattering properties of the metamaterial.

In the first part of this work, existing criteria for noise limits in auditoria are reviewed and new measurements of audience background noise are presented. The measurements are performed in three opera venues and one drama venue and add up to 22 hours of noise data from twelve different live performances with occupied auditoria. The audience noise data is extracted using three common metrics: minimum 1s-averaged level, Gaussian mixture model, and N% exceedance level. The metrics are discussed and their reproducibility is compared using two takes of the same piece measured on different days. The audience noise data is utilized to propose noise limits for operating stage machinery during live performance of opera, ballet and drama.

To improve the quality of performance spaces based on the proposed noise limits, acoustic metamaterials are considered for noise control of stage machinery. To reflect the sound waves a simple c-shape meta-atom is introduced and an air-permeable meta-grating is designed. Subsequently, the designed meta-grating is combined with absorbing material, and applied to develop a prototype of an acoustic metamaterial capsule, which attenuates noise in a distinct frequency band and allows for airflow. This prototype is verified numerically and experimentally, and shows promising results. Subsequently, a metamaterial capsule is designed to attenuate a single critical peak of the sound pressure spectrum of a gear-box used in a rope drive system. The metamaterial capsule is modelled numerically and, subsequently, manufactured and verified experimentally. The sound attenuation at the critical frequency is confirmed in the experiment. Furthermore, the cooling properties of the electric motor and the gear box inside the capsule are verified in a numerical simulation to fulfill the industrial cooling requirements. Additionally, the sound pressure spectra of three drive train types usually used for under-stage machinery are modelled using a series of different numerical approaches. To attenuate the resulting critical peaks at multiple frequencies simultaneously, multi-layer meta-gratings are proposed.

In the last part of this work, the introduced c-shape meta-atom is investigated with regards to its scattering properties and Willis coupling, an acoustic analogy of electromagnetic bianisotropy. The c-shape meta-atom is found to demonstrate Willis coupling due to strong asymmetry. Furthermore, it is shown that the losses inside the c-shape meta-atom are reduced in comparison to previously reported acoustic meta-atoms with comparable properties. Reduced losses combined with strong asymmetry result in a design, which is found to approach the theoretical bound of Willis coupling. The polarizability of the c-shape meta-atom, including Willis coupling terms, is modelled analytically and

numerically. Furthermore, a Willis coupling magnitude of 90 % of the theoretical bound is demonstrated experimentally.

Kurzfassung

Diese Arbeit liefert einen Beitrag auf dem Gebiet der Lärmbekämpfung und den akustischen Metamaterialien. Im Folgenden wird die Anwendung der Metamaterialien in der Bühnentechnik näher untersucht. Das beinhaltet eine Verfeinerung der Lärmanforderungen an die Bühnenmaschinerie, das Entwickeln einer Metamaterialkapsel zur Reduktion der Lärmemission von Maschinen und eine theoretische und experimentelle Untersuchung der Streueigenschaften des verwendeten Metamaterials.

Im ersten Teil dieser Arbeit werden die bestehenden Anforderungen an die Lärmmission im Auditorium besprochen und neue Messungen der durch die Zuschauer verursachten Hintergrundpegel werden vorgestellt. Die Messungen wurden in drei Opernhäusern und einem Sprechtheater durchgeführt und ergeben zusammen 22 Stunden Messdaten von Schalldruckpegeln, die in zwölf Vorstellungen mit Zuschauern aufgenommen wurden. Der durch die Zuschauer verursachte Schalldruckpegel wird mit Hilfe von drei bekannten Metriken extrahiert: das Minimum eines über eine Sekunde gemittelten Schalldruckpegels, die Gauss'sche Mischverteilung und N%-Überschreitungspegel. Die Metriken werden diskutiert und deren Wiederholbarkeit wird basierend auf einem Stück verglichen, welches an zwei verschiedenen Tagen aufgenommen wurde. Ausgehend von dem durch die Zuschauer verursachten Schalldruckpegel werden Anforderungen an die Schallemission für die Bühnentechnik während der Opern-, Ballett- und Theatervorstellung vorgeschlagen.

Zur Steigerung der Qualität der Bühnentechnik wird der Ansatz der akustischen Materialien zur Lärmbekämpfung betrachtet. Um Schallwellen zu reflektieren wird ein einfaches c-förmiges Metaatom für das Design eines luftdurchlässigen Metagitters verwendet. Nachfolgend wird mit Hilfe der Kombination des Metagitters mit einem absorbierenden Material der Prototyp einer Metakapsel entwickelt. Die Metakapsel reduziert die Schallemission einer eingekapselten Quelle bei einer bestimmten Frequenz, ermöglicht aber gleichzeitig den Luftaustausch mit der Umgebung. Der Prototyp wird experimentell und numerisch validiert und zeigt aussichtreiche Ergebnisse. Als nächster Schritt wird eine Metakapsel designt, um die Schallemissionen bei einem kritischen Peak im Emissionsspektrum eines Seilantriebsgetriebes zu reduzieren. Diese Metakapsel wird zuerst numerisch modelliert, danach gefertigt und in einem Experiment erfolgreich validiert. Des Weiteren werden die Kühleigenschaften des von der Metakapsel eingeschlossenen Elektromotors und des Getriebes durch eine numerische Simulation überprüft und die Erfüllung der typischen Anforderungen an die Kühlung von Elektromaschinen gesichert. Zusätzlich werden die Schallemissionsspektren von drei weiteren in der Untermaschinerie üblichen Antriebsarten in einer Kette von verschiedenen numerischen Modellieretechniken bestimmt. Basierend auf diesen Spektren werden mehrschichtige Metagitter designt, die die kritischen Peaks bei unterschiedlichen Frequenzen gleichzeitig reduzieren können.

Im letzten Teil dieser Arbeit wird das c-förmige Metaatom auf seine Streueigenschaften und die Willis-Kopplung untersucht. Die Willis-Kopplung ist eine akustische Analogie

der Bianisotropie im Elektromagnetismus und gewinnt immer mehr an Bedeutung für effiziente akustische Metamaterialien. Es wird in dieser Arbeit herausgefunden, dass das Metaatom eine starke Willis-Kopplung aufgrund seiner Asymmetrie aufweist. Zusätzlich wird gezeigt, dass die Geometrie wesentlich weniger verlustbehaftet im Vergleich zu anderen Designs mit vergleichbaren Eigenschaften ist. Die Kombination der reduzierten Verluste mit einer starken Asymmetrie resultiert in einem Design, das dem theoretischen Maximum an Willis-Kopplung sehr nahe kommt. Die Polarisierbarkeit des c-förmigen Metaatoms inklusive der für die Willis-Kopplung verantwortlichen Terme wird analytisch und numerisch modelliert. Des Weiteren wird ein Betrag der Willis-Kopplung von rd. 90 % des theoretisch erreichbaren Maximums experimentell nachgewiesen.

Acknowledgments

I wish to express my deepest gratitude to my supervisor, Steffen Marburg, for his guidance through each stage of the process, for the huge amount of time we spent on technical discussions, and for his interpersonal advice.

I would like to thank my wife, Anastasia Melnikov, and my daughter, Palina, for their patience and for their deepest support.

Furthermore, I wish to express my gratitude to Manfred Freimüller and Christian Freimüller, executive board of SBS Bühnentechnik GmbH, for the opportunity to work on this research project. I also would like to thank Jens Ahrens, associate professor at Chalmers University of Technology, for fruitful discussions, for great jam sessions at the DAGAs, and for examining this dissertation. I also would like to thank Markus Zimmermann, professor at Technical University of Munich, for taking the examination chair.

I would like to thank David Powell, senior lecturer at UNSW Canberra, for detailed introduction into metamaterials, for a lot of technical discussions, for revising the paper drafts, and for proofreading the papers. Furthermore, I would like to thank Sebastian Oberst, senior lecturer at UTS Sydney, for inviting me to Sydney and Canberra and for the guidance on scientific writing including revising the paper drafts. Furthermore, I would like to thank Michael Scheffler, professor at University of Applied Sciences Zwickau, for supporting me at the very initial stage of this project and for further collaboration.

I would like thank Steffen Nürnberger, engineering director at SBS Bühnentechnik GmbH, for his support and advice. Additionally, I would like to especially thank Niklas Friedrich, Michael Langgemach, and Alexander Maslov from SBS Bühnentechnik GmbH for their significant contribution to the research project. Furthermore, I would like to thank Georg Schnurr, Michael Schulz, and all colleagues from the departments *Projektierung* and *Konstruktion*.

I would like to thank Marcus Maeder, Lennart Moheit, Magdalena Scholz, Johannes Henneberg, Suhaib Koji Baydoun, and Monika Gatt, from the Chair of Vibroacoustics of Vehicles and Machines at TUM, for their contribution, their support, interesting discussions, and the enjoyable time.

I would like to thank Ingo Witew from the Institute of Technical Acoustics at RWTH Aachen University for his time and effort on revising my first paper and for introducing me to scientific writing. Furthermore, I would like to thank Christoph Höller, professor at Regensburg University of Applied Sciences, for proofreading the Applied Acoustics paper and the thesis.

I would like to thank my mentor, Hermann Schenk, managing director of Arioso Systems GmbH, for his support during the final stage of my thesis.

Finally, I would like to thank Bert Kaiser and Holger Conrad from Fraunhofer Institute for Photonic Microsystems for providing me with opportunities to finalize my thesis in parallel to my new position.

Appended papers

- [1] A. Melnikov, I. Witew, M. Maeder, M. Gatt, M. Scheffler, and S. Marburg. “Sound pressure level limits for stage machinery noise in operas and theaters”. In: *Applied Acoustics* 156 (Dec. 15, 2019), pp. 29–39.

Melnikov designed the study, conducted 9 live performance measurements, reverberation time measurements, and background noise measurements in venues located in Dresden and Leipzig, analyzed the raw data, developed and applied the analysis methods, derived the noise limits and wrote the paper. Maeder and Gatt conducted 3 measurements in Bayerische Staatsoper. Maeder conducted background noise measurement in Bayerische Staatsoper. Witew analyzed the reverberation time data. Maeder and Scheffler provided guidance on the choice of the measurement equipment. Witew and Marburg provided guidance on the analysis methods. Marburg supervised the work.

- [2] A. Melnikov, M. Maeder, N. Friedrich, Y. Pozhanka, A. Wollmann, M. Scheffler, S. Oberst, D. Powell, and S. Marburg. “Acoustic metamaterial capsule for reduction of stage machinery noise”. In: *The Journal of the Acoustical Society of America* 147.3 (Mar. 1, 2020). Publisher: Acoustical Society of America, pp. 1491–1503.

Melnikov conceived the meta-atom, developed the single and multilayer meta-gratings, designed, manufactured, and validated the metamaterial capsules experimentally and numerically, derived the impedance model, designed the machinery noise modelling chain, and wrote the paper. Melnikov and Friedrich created numerical models for the mesh fluctuation excitation; Melnikov and Maeder designed numerical models for structural vibrations; Maeder developed geometrical acoustics model. Melnikov and Pozhanka designed the CFD model; Pozhanka conducted the CFD simulations. Wollmann and Scheffler provided support during experimental validation of rope drive capsule. Powell provided guidance on the metamaterials and analytical modelling. Oberst and Powell provided guidance on the dynamic modelling. Marburg supervised the work.

- [3] A. Melnikov, Y. K. Chiang, L. Quan, S. Oberst, A. Alù, S. Marburg, and D. Powell. “Acoustic meta-atom with experimentally verified maximum Willis coupling”. In: *Nature Communications* 10.1 (July 17, 2019), p. 3148.

Melnikov conceived the meta-atom structure, and designed the experimental sample, validated the results experimentally, numerically and analytically, and wrote the paper. Melnikov and Powell developed the analytical model; Powell designed the experimental setup; Melnikov and Chiang designed and manufactured the final experimental sample; Chiang performed additional measurements to maximize the experimental performance. Quan performed the thermo-viscous FEM calculations and supported the numerical and analytical study. Marburg and Alù provided guidance on numerical and theoretical aspects of the study, respectively. Melnikov, Oberst, and Powell conceptualized the study. Powell and Marburg supervised the work.

Publications not appended to this work

- [4] A. Melnikov. “Geräuschlos bewegen, Ansätze zur Reduzierung der Schallemission der Untermaschinerie [Silent Movement, Approaches for Noise Reduction of understage Machinery]”. In: Bühnentechnische Rundschau Sonderband [Stage Machinery Review, Special Edition] (2015), pp. 36–39.
- [5] A. Melnikov, M. Scheffler, and S. Marburg. “Untersuchungen eines Bühnenpodiums hinsichtlich der Reduktion von Geräuschemission [Investigations of a Stage Elevator concerning Noise Reduction]”. In: DAGA 2017 Kiel (2017).
- [6] A. Melnikov, M. Scheffler, and S. Marburg. “Sound Radiation of Stage Elevators with ANSYS and Boundary Element Method”. In: Proc. of CADFEM ANSYS Simulation Conference (2017).
- [7] A. Melnikov, M. Maeder, M. Gatt, M. Scheffler, and S. Marburg. “Development of a novel sound pressure level requirement for characterizing noise disturbances from theater and opera stages”. In: Proceedings of Meetings on Acoustics 30.1 (2017), p. 030013.
- [8] A. Melnikov, I. Witew, M. Maeder, M. Gatt, M. Scheffler, and S. Marburg. “Limits for Stage Machinery Noise”. In: INTER-NOISE and NOISE-CON Congress and Conference Proceedings. Chicago, IL, 2018, 1672–1677(6).
- [9] A. Melnikov, I. B. Witew, M. Mäder, M. Gatt, M. Scheffler, and S. Marburg. “Stage machinery noise - What limits are appropriate?” In: Proceedings of the Institute of Acoustics. Auditorium Acoustics 2018. Vol. 40., Pt. 3. 2018. Hamburg, 2018, pp. 625–628.
- [10] J. Jordaán, S. Punzet, A. Melnikov, A. Sanches, S. Oberst, S. Marburg, and D. A. Powell. “Measuring monopole and dipole polarizability of acoustic meta-atoms”. In: Applied Physics Letters 113.22 (Nov. 26, 2018), p. 224102.
- [11] A. Melnikov, L. Quan, S. Oberst, A. Alù, S. Marburg, and D. Powell. “Acoustic meta-atom with maximum Willis coupling”. In: arXiv:1812.02318 [physics] (Dec. 5, 2018). arXiv: 1812.02318.

Contents

1	Introduction	1
1.1	State of the art	2
1.1.1	Stage machinery	2
1.1.2	Noise in auditoria	3
1.1.3	Stage machinery noise	4
1.1.4	Acoustic metamaterials	5
1.1.5	Noise control using acoustic metamaterials	5
1.1.6	Willis coupling in acoustic metamaterials	6
1.2	Contribution of this work	8
2	Methods	9
2.1	Audience noise measurement	9
2.2	Data analysis and noise limit derivation	9
2.2.1	Minimum 1 s-averaged (min1s) level	9
2.2.2	Gaussian Mixture Model (GMM)	10
2.2.3	N%-exceedance level (L_N)	11
2.2.4	Derivation of the noise limits	11
2.3	Analytical modeling of ideal plane wave transmission through the meta-grating	11
2.4	Design and fabrication of the metamaterial capsules	12
2.4.1	Prototype of the metamaterial capsule	12
2.4.2	Rope drive capsule	13
2.5	Numerical modelling of the metamaterial capsule properties	14
2.5.1	Plane wave transmission through the 2D meta-grating	14
2.5.2	Transmission through the capsule prototype	14
2.5.3	Transmission through the rope drive capsule	14
2.5.4	Cooling performance of the rope drive capsule	15
2.6	Experimental determination of transmission through the metamaterial capsules	15
2.7	Numerical modeling chain from meshing force fluctuation to Sound Pressure Level (SPL) in the middle of the first row	16
2.8	Extraction of polarizability tensor of the meta-atom	17
2.9	Numerical modelling of the meta-atom scattering	19
2.9.1	2D Boundary Element Method (BEM)	19
2.9.2	2D Finite Element Method (FEM) with thermo-viscous losses	20
2.10	Waveguide scattering experiment	20
2.11	Analytical modeling of the polarizability of acoustic meta-atoms	21
2.11.1	Coupling approach	21
2.11.2	Polarizability of a rigid cylinder	21
2.11.3	Polarizability of a Helmholtz resonator	22

3 Paper Summary	24
3.1 Paper [1]	24
3.2 Paper [2]	25
3.3 Paper [3]	26
4 Discussion of Results	27
4.1 Paper [1]	27
4.2 Paper [2]	28
4.3 Paper [3]	30
5 Conclusion	32
References	33
Appended Papers	43

1 Introduction

Noise goes along with us through all our life. We are exposed to noise every day, every hour, every second. Fortunately, our brains are powerful enough to keep our attention away from most noise events during the day. However, there are numerous situations where everyone would like to have some silence. For example, when you are in bed and try to sleep, but your neighbor plays the solo from Snarky Puppy's tune Atchafalaya on electric guitar. Where is the borderline between sound and noise? There is an entire field dedicated to our subjective perception of sound, called psychoacoustics. Despite years and years of research, it is still a philosophical question: what is sound, or even musical art; and what is noise?

One of the aims of this work is to separate music and machinery noise, however, not in a philosophical, but in a rational engineering way. Machinery noise is an issue found almost everywhere: industry, cars, airplanes, urban areas, households etc. Many effective means for sound mitigation already exist in most areas, however, some of them still require special attention. One such area concerns opera and drama performances, where the art has to be protected from noise distortions during the use of stage machinery. The progress of the modern stage performance art leads to more stringent requirements on the equipment. One of the most demanded properties is low noise emission, where Fig. 1 demonstrates a trend to more and more stringent requirements in the period from 2005 to 2014. However, the feasibility, the necessity, and the price of such an increase needs to be discussed. This is the topic of the first part of this work.

To improve the noise emission quality of machinery installations in the stage area it is common to use well-known noise control techniques. However, it is not always possible, since the special boundary conditions of stage machinery can be very challenging: financial restrictions from the project budget, noise below 1000 Hz, little space, and, additionally, the installations should look appropriate to the venue, in other words like a piece of art. Presumably, all these conditions can be fulfilled by proper design of acoustic metamaterials, a relatively new field of acoustics. Acoustic meta-materials are structures with periodic geometrical pattern which can provide promising properties concerning noise control. Interestingly, one of the origins of intense research in the field of acoustic metamaterials and sonic crystals is linked to an object of art, the famous sculpture created by Eusebio Sempere in Madrid [12]. This sculpture was found to attenuate sound waves at distinct frequency ranges [12]. Since then, further concepts of interconnections between acoustic metamaterials and art have been demonstrated [13, 14]. Furthermore, it has been shown that sound waves can be blocked with acoustic metamaterials of sub-wavelength thickness [15]. This is truly promising considering the requirement of noise attenuation at low frequencies at places with little space and the expectations on visual appearance in art performing venues. Therefore, a major part of this work is focused on the development of acoustic metamaterials for noise control of stage machinery.

Cummer *et al.* [16] reviews many different possibilities of sound wave control using acous-

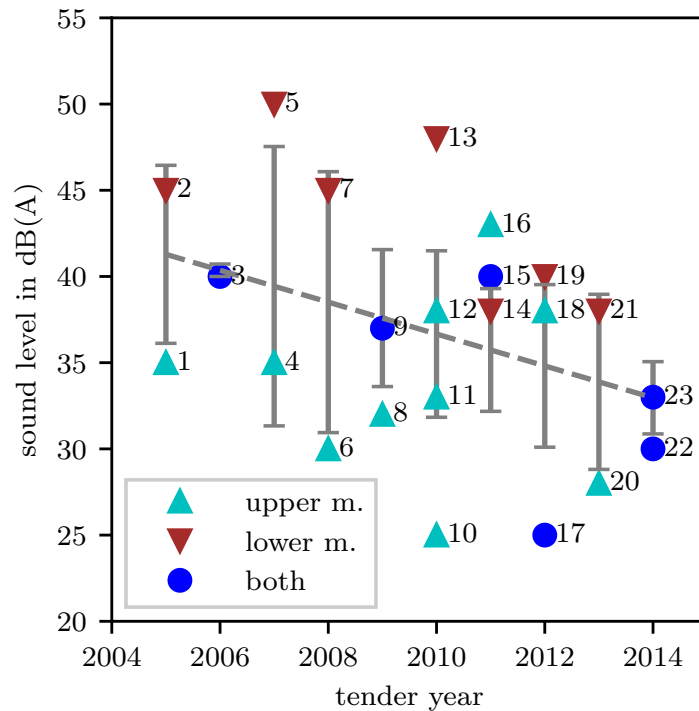


Figure 1: Sound level requirements at first auditorium row from tender documents between 2005 and 2014. For numbering legend see **Paper [1]**. Gray dashed regression line shows a decreasing trend. (adapted from **Paper [1]**).

tic metamaterials far beyond noise control applications, such as beam steering and cloaking. And of course it is always an aim of research to dig deeper for better understanding of the effects forming our world. Therefore, in the final part of this work the designed acoustic metamaterial geometry is investigated in detail revealing its polarizability properties and its Willis coupling.

1.1 State of the art

1.1.1 Stage machinery

Stage machinery is part of almost every modern opera and drama house [17, 18]. The main purpose of stage machinery is logistics of curtains, decorations, or staff. Most of the time the machinery is used in the breaks between the performances, where it should fulfill the usual requirements on logistics engineering, such as safety, reliability, versatility, and speed. Meanwhile, there is another more fascinating field of application, namely scenic application during the performance. This is where the artistic freedom and the scenic magic involving lights, action, drama, art, and scenic movements start. However, this introduces an additional requirement on the low noise emission of stage machinery. The noise during the movements provided by the stage machinery must not be perceived by the audience.

The stage machinery is divided into understage and overstage machinery. The required

high power of the stage elevators as a principal part of understage machinery requires powerful motors and gear boxes. These components are in general major sources of stage machinery noise [5, 6]. To make things worse, the transfer paths from these noise sources of the understage machinery to the auditoria are very short as the location of the engines driving the stage elevators is usually directly under the main stage (see Fig 2). The upper surface of the elevator shapes the stage floor. Commonly, the floor area of one stage elevator has a size of $12..16 \times 2..4 \text{ m}^2$ with the capability of vertical movement of $\pm 3 \text{ m}$ or more. The load is standardized with $250 \text{ kg} \cdot \text{m}^{-2}$ and the stage elevator itself weighs usually $25..45 \text{ t}$, which results in a total mass of up to 90 t . To move such a mass with commonly used speeds up to $0.3 \text{ m} \cdot \text{s}^{-1}$ a power of up to 30 kW is required. Subsequently, such installations have all prerequisites to emit low frequency noise at audible levels and require noise control.

Before any noise control approach can be investigated it is necessary to review the noise limits. For noise optimization of stage machinery it is required to know the limits as Sound Pressure Level (SPL) or sound power dependent on the frequency. In many noise control applications it is common to consider limits in octave bands, while it is possible to subdivide the octaves or to use narrow band spectra if necessary. If SPL is used, the reference location or the distance to the source should be specified. For stage machinery applications the reference location is commonly specified as the middle of the first row as shown in Fig. 2. In some cases the location behind the head of the conductor is considered and in some rare cases locations further away from the stage are defined [19].

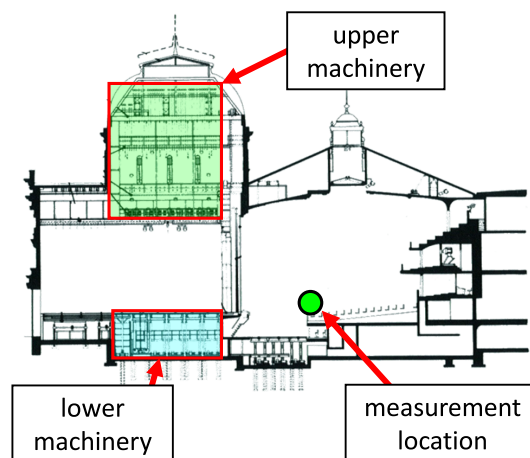


Figure 2: Longitudinal section of Zurich Opera House [17] with location of upper stage machinery, lower stage machinery, and measurement location (reference location).

1.1.2 Noise in auditoria

The noise present in auditoria is usually divided in two parts, 'technical background noise' and 'audience noise'. Technical background noise is generated by equipment such as Heating, Ventilation and Air Conditioning (HVAC) systems or traffic noise and is constant

or features moderate variance over time. This type of noise is sometimes referred to as 'static' background noise and can be predicted. In contrast the audience noise is the result of human activity like breathing, whispering, coughing, or moving around, and is more difficult to characterize. This type of noise is called 'dynamic' background noise. Both parts together result in 'mixed background noise' [20, 21].

Currently, the following requirements for technical background noise usually formulated in octave bands are in use: Noise Criterion (NC) [22, 23], Preferred Noise Criterion (PNC) [24], Noise Rating (NR) [25], Balanced Noise Criterion (NCB) [26, 27], and Room Criterion (RC) curves [28]. For opera houses and drama theaters limits of NC20 are commonly recommended in literature [22, 29, 30]. However, in some cases NC15 or PNC15 can be used separately for continuous building services noise. NC20 corresponds to a sound level of about 25 dB(A) and NC15 to 20 dB(A). It should be mentioned that these requirements serve as a basis for planners and architects designing rooms and buildings. Furthermore, these limits are primarily aimed at steady-state technical noise and do not consider audience noise and the live performance sound. However, for setting stage machinery noise limits such non-steady-state noise and sound sources should be considered.

Investigations in movie theaters [31] and lecture halls [32] have shown that audience noise depends on the situation and the intended use of the venue. Both studies have also shown that audience noise is not stationary but depends a lot on the presented 'action'. Measurements of audience noise focused on live performance situations in concert halls reveal levels around 32 dB(A) [20, 33, 34]. Furthermore, Ref. [20] points out that there is a correlation between background noise and audience noise. However, the data in venues, where the stage machinery is mainly used is sparse. To the author's best knowledge the only available opera and drama theater data is: Ref. [20] including a single opera house measurement (Copenhagen Opera house) and Ref. [21] presenting a series of measurements during theatrical performances (Gothenburg Town Theater). Subsequently, to conclude on stage machinery noise limits for opera and theater houses it is necessary to collect additional representative data.

1.1.3 Stage machinery noise

Despite the fact that there is not much research on audience noise in opera and theater houses, an eminent study on stage machinery noise was conducted by Tennhardt [35]. The sound levels of different stage machinery types in several German theaters were measured and correlated with subjective feedback of theater staff (stage directors, dramatic advisors, sound board operators). The outcomes are the following limits: drama theater, 35 dB(A) for lower machinery and 45 dB(A) for upper machinery; musical theater, 40 dB(A) for lower machinery and 45 dB(A) for upper machinery [17, 35]. Unfortunately, this study is based on total levels in dB(A), hence it does not provide any frequency dependent information required for appropriate noise optimization of stage machinery.

At the same time noise optimization in real engineering projects is motivated by levels that are imposed by tender documents. Presumably, the requirements are oriented at Ref. [35] or at NC20 (≈ 25 dB(A)) as recommended for opera and drama theaters [22, 29, 30]. Figure 1 gives an overview of requirements for the first row of auditorium from international data between 2005 and 2014 [4]. Against the expectations, the data scatters between 25 dB(A) and 50 dB(A) and there are no preferred limits observed. Additionally, a trend towards more stringent limits is present (gray dashed line). For that reason strict noise limits such as <35 dB(A) seems to be reasonable in the future. Comparing Fig. 1 with the limits from Ref. [35] shows that 34 % of the tenders underestimate the proposed limits, 9 % match it and 57 % overestimate it. This demonstrates that there is no general consensus between either known literature and tender requirements or the different tender documents itself. Moreover, there are reasons to doubt that limits below 30 dB(A) are feasible for the stage machinery of current state of the art [36–40].

To summarize the introduction on noise limits for stage machinery, it is observed that there are a number of noise criteria for background noise available [22–28]. While these criteria are focused on steady-state background noise, they do not consider real life performance sound and audience noise. The research conducted on audience noise in opera and theater houses is sparse and does not provide all significant information for setting noise limits [20, 31–35]. Furthermore, lacking consensus on noise limits observed in tender documents indicates that noise limits of stage machinery is still an open research question.

1.1.4 Acoustic metamaterials

Metamaterials are arrays of sub-wavelength structures, called meta-atoms or unit cells. A single layer of meta-atoms is usually called a meta-grating. The geometry of a single meta-atom is used to engineer its scattering properties, which causes a change of the dynamic behavior of the whole metamaterial.

In the last decade, acoustic metamaterials have attracted interest of a large international research community [16]. Acoustic metamaterials provide material properties not existing naturally, where the most prominent example are the negative bulk modulus [41] and negative dynamic mass density [42]. Owing to such properties a number of promising applications have been demonstrated: acoustic superlenses [43–45], noise barriers [15, 46–64], cloaking devices [65] and the enhancement of non-linear effects [66]. The application of acoustic metamaterials for noise barriers is particularly interesting for stage machinery.

1.1.5 Noise control using acoustic metamaterials

Recently, a lot of research have been done on sound barriers using acoustic metamaterials. Fard *et al.* [47] showed in a numerical study that noise attenuation is possible

over a frequency range of more than one octave. Henneberg *et al.* [48, 49] designed and verified a stop-band material and expanded the application to multiple frequencies. Claeys *et al.* [50, 67, 68] designed and verified a sound insulating capsule based on stop-band materials with elastic resonators. Marinova *et al.* [51] demonstrated a noise barrier based on a membrane-type metamaterial. Groby *et al.* [69] presented an effective attenuation of low frequency noise using Helmholtz resonators embedded in absorbing foam. These are airtight concepts, which blocks air flow required for cooling, if heat dissipative components, such as electric motors or gear boxes are placed inside.

To allow air flow, perforated membrane-type metamaterials have been shown by Ma *et al.* [52] and Langfeld *et al.* [53]. Furthermore, different space coiling metamaterials have been proposed [13, 15, 54–57]. Cheng *et al.* [15] realized 93 % insertion loss by a meta-grating having a thickness only 0.15 times the wavelength at 500 Hz. Shen *et al.* [58] created a full metacage and validated its ventilation properties experimentally.

Furthermore, air permeable acoustic absorbers have been demonstrated [59–62]. Wu *et al.* [59, 60] achieved an absorption of 88.9 % by a single layer of metamaterial using the viscosity of air in thin channels. Lee *et al.* [61] designed paired Helmholtz resonators with an absorption of 90 % providing additional degrees of freedom for air flow control. Xiang *et al.* [62] demonstrated a metamaterial absorber showing 60 % absorption over a broad frequency range. Furthermore, metamaterials have been applied to windows allowing for air-flow [63, 64].

Although the previous work covers a large range of ideas and designs, it does not match all the requirements for stage machinery noise control: cheap in production, sub-wavelength, air-permeable, robust etc. However, considering the formidable results of previous investigations, it looks promising to engineer a metamaterial suitable for stage machinery.

1.1.6 Willis coupling in acoustic metamaterials

To exploit more sophisticated metamaterial properties, as those usually used for noise control, a different view on the metamaterial is required. Recently, it has been shown that Willis coupling is a promising concept to improve efficiency of acoustic meta-materials [70–72]. Willis coupling couples potential and kinetic energy and is an analogy to the well-known bianisotropy parameter in electromagnetism [73–78]. Willis coupling of acoustic meta-atoms can be read from the polarizability tensor, whereas, the polarizability describes the scattering properties of a single meta-atom.

Willis coupling, as well as electromagnetic bianisotropy are only non-zero when the structures are not symmetric. It has been shown, that the bianisotropy can be tailored in a wide range for electromagnetic meta-atoms [79]. The range, in which Willis coupling is feasible or could be engineered is still not investigated. Recently, it has been demonstrated that Willis coupling has a theoretical maximum bound based on conservation of energy [71]. To reach the maximum bound, meta-atoms can be designed using space coiling structures involving long meander-shaped channels [15, 71, 80, 81]. However, manufacturing

of such structures can be very complicated, especially considering reproducibility and tolerances. Additionally, the scattering efficiency of such meta-atoms is reduced, since the long and thin channels results in an increase of thermo-viscous losses [10, 82, 83]. Quan *et al.* [71] demonstrated numerically how Willis coupling magnitude of space coiling meta-atoms is reduced, when thermo-viscous losses are considered.

Sieck *et al.* [84] have demonstrated the procedure to derive effective medium properties from the polarizability including Willis coupling of individual meta-atoms. Furthermore, Willis coupling was demonstrated in experiments [70, 85, 86], however, it was not tested, how close the theoretical limit [71] can be approached. Furthermore, no meta-atom designs have been proposed to reduce the thermo-viscous losses. If an easy manufacturable and robust geometry being suitable for stage machinery noise control can be successfully found, further investigations of its properties such as Willis coupling should be done. It is always desirable to find simple structures, which provides unique properties necessary to push the progress on metamaterial research.

1.2 Contribution of this work

This work contributes to the field of noise control and acoustic metamaterials. The following research questions are considered:

- What noise limits are appropriate for stage machinery? [1]
- How can the noise limits be fulfilled using acoustic metamaterials? [2]
- How can the efficiency of acoustic metamaterials be increased? [3]

The questions are addressed in the appended papers. The results offer the possibility to improve the quality of stage machinery and to realize acoustic metamaterials with properties beyond the state of the art concepts.

Paper [1]. The audience background noise was measured during 12 live performances in four different venues. The measured data was presented and analyzed with different methods and the results were discussed from the point of view of reproducibility and applicability. Furthermore, the likelihood of stage machinery operation was linked with the probability of the quietest moments during the performance. At the end of the manuscript standard and sensitive noise limits for stage machinery have been proposed.

Paper [2]. A 2D c-shape meta-grating was designed and validated numerically demonstrating strong transmission loss. The meta-grating design was extended to a 3D metamaterial capsule, which was validated numerically and experimentally. Furthermore, a metamaterial capsule was designed, manufactured and verified numerically and experimentally for a rope drive system. An analytical model was created for the 2D meta-grating based on basic dynamics of a Helmholtz resonator. This model was used to design multi-layer meta-gratings to fulfill noise requirements for simulated stage machinery noise spectra.

Paper [3]. The scattering properties of a single c-shape meta-atom were investigated. Its polarizability tensor including Willis coupling was analyzed. The c-shape meta-atom was designed to reduce thermo-viscous losses and to be easily manufacturable. Furthermore, it has been demonstrated how the Willis coupling magnitude can be tailored between zero and theoretical bound derived from conservation of energy. The Willis coupling properties of the c-shape have been verified analytically, numerically and experimentally. Due to increased efficiency of the meta-atom, the Willis coupling magnitudes obtained during the experiment reach far beyond the state of the art.

2 Methods

2.1 Audience noise measurement

For derivation of noise limits it is required to capture the background and audience noise under realistic performance conditions. This was done during 12 live performances in occupied venues. Following venues have been chosen for the measurements: Semperoper Dresden (opera), Leipzig Opera (opera), Bayerische Staatsoper (opera), and State Playhouse Dresden (drama theater). All venues fulfill the theater recommendation of NC20 and PNC20 [22, 29, 30, 87]. The measured pieces have been chosen to cover a broad range of styles and epochs (see the full list in **Paper [1]**).

The measurement location was in the middle of the first row [35–37, 40, 88] (see Fig. 3(a)). The measurement equipment was the handheld analyzer type 2270 from Bruel&Kjaer equipped with the 1/2-inch free-field microphone type 4189 and ZC-0032 preamplifier [89, 90] (see Fig. 3). The microphone was located 120 cm above the floor during the measurement [91].

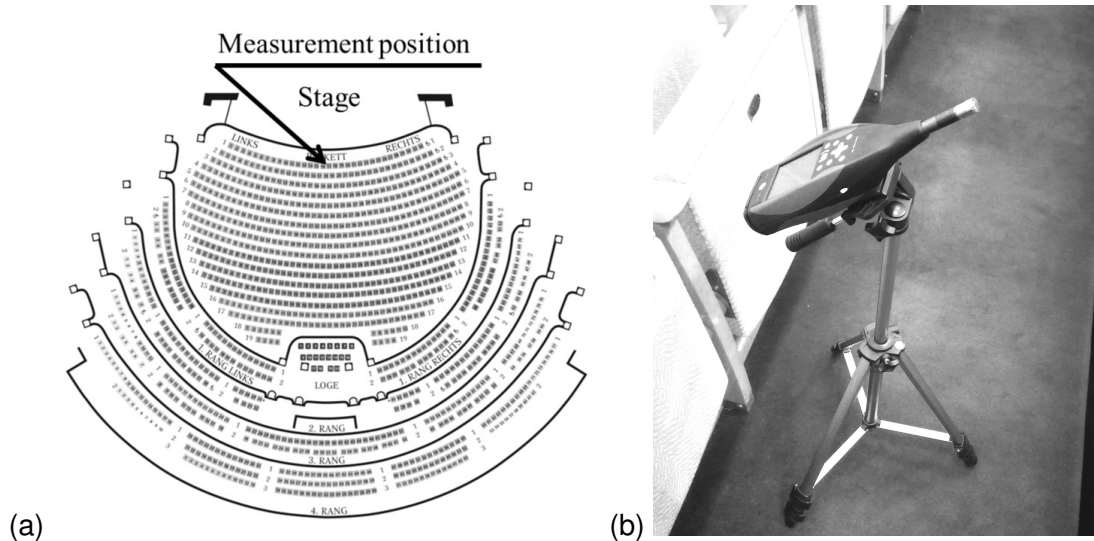


Figure 3: (a) Measurement location, which is usually defined in tender documents (adapted from Ref. [7]). (b) Used measurement setup: Handheld analyzer supported by tripod. Photograph taken in Leipzig Opera.

2.2 Data analysis and noise limit derivation

2.2.1 Minimum 1 s-averaged (min1s) level

The Minimum 1 s-Averaged Level (min1s) method looks for the quietest period of time with a defined length of 1 s [92]. For the SPL data in discrete time steps the min1s level can be determined by moving time average with a rectangular window function

$$L_{\min} = \min \left\{ 10 \lg \left(\frac{1}{n} \sum_{i=1}^n 10^{0.1 L_{j+i}} \right) \right\}, \quad (1)$$

with $\min\{\}$ as minimum operator, L_{j+i} as band filtered or broad band level at sample $j+i$, and n as number of samples in the window. Figure 4 shows an example SPL data with the identified min1s period.

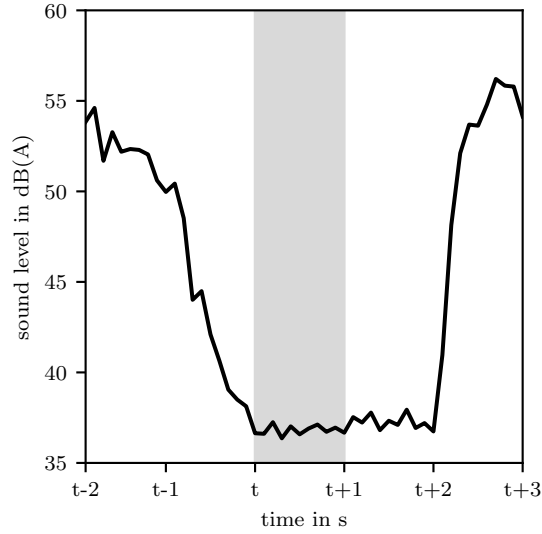


Figure 4: A-weighted total level of a short break during the performance. Solid black line is the level and the gray region indicates the averaging time for obtaining the min1s level. (adapted from **Paper [1]**)

2.2.2 Gaussian Mixture Model (GMM)

SPL is classified into discrete containers and their relative frequency (here from statistics point of view, not time-harmonic) is considered. Gaussian Mixture Model (GMM) [93] transforms the level distribution into a linear combination of normal distributions

$$\varphi_k(x) = \frac{1}{\sqrt{2\pi\sigma_k^2}} e^{-\frac{1}{2}\left(\frac{x-\mu_k}{\sigma_k}\right)^2}. \quad (2)$$

Subsequently, the single normal distribution can be combined to a global distribution by

$$p(x) = \sum_{k=1}^N w_k \varphi_k(x). \quad (3)$$

The mean value of the distribution with the lowest SPL defines the background noise. A similar method was applied for previously conducted background noise studies [20, 32]. The special character of the method applied here is the use of Bayesian Information Criterion (BIC) [94, 95] for the determination of the optimal number of distributions. Figure 5 shows an example result for a full length piece, where 6 normal distributions are identified.

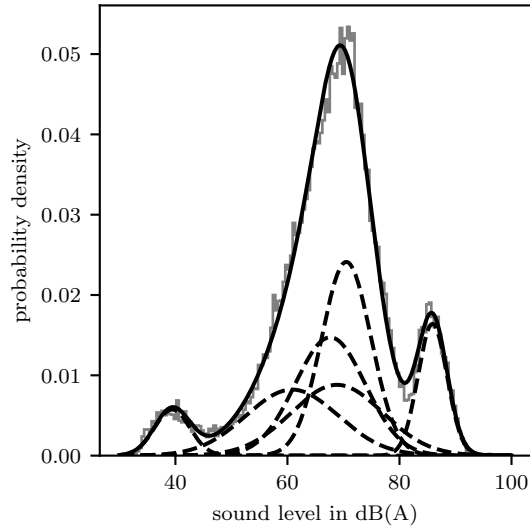


Figure 5: GMM (solid black line) applied to the measured PDF (solid gray line) of total level in the ballet piece Don Juan. BIC suggests 6 normal distributions (dotted lines) as suitable. (adapted from **Paper [1]**)

2.2.3 N%-exceedance level (L_N)

The N%-exceedance level states how often a specified level is exceeded over a defined time period [96, 97]. This type of metric is very common in noise studies of traffic noise, urban noise, or noise pollution [98–102]. The known quantile N of L_N can be directly used for subsequent probabilistic analyses. For determination of the audience background noise the quantiles 95 and 99 have been used.

2.2.4 Derivation of the noise limits

To check the stability of the applied metrics the reproducibility has been reviewed by measuring one piece twice. The metric results from two different measurements taken at different days have been compared. The complete measurement set-up was dismantled and mounted again and the audience was completely changed.

The likelihood of stage machinery operation has been estimated based on the prescribed intermittent duty S3 40% [103] and on the common stage machinery assumptions. Linking the estimated likelihood with the probability of SPL to be below the metric levels lead to the likelihood of stage machinery imperceptibility. Based on this consideration it was possible to derive standard and sensitive limits for stage machinery noise in the auditoria.

2.3 Analytical modeling of ideal plane wave transmission through the meta-grating

The meta-grating consists of c-shape meta-atoms, which can be considered as 2D Helmholtz resonators. From the dynamics of a Helmholtz resonator (see **Paper [3]**, Supplementary

Equation S37) an impedance model for acoustic filters can be derived [104, 105]. This results in

$$Z_{\text{MA}}(\omega) = \frac{2A_d}{A_w} \left(i\omega\rho_0 l_{\text{eff}} + b - \frac{i}{\omega} \frac{K}{V} A_w \right), \quad (4)$$

where A_d is the meta-grating cross section belonging to one meta-atom, A_w is the c-shape's aperture cross section, i is the imaginary unit, ω is the angular frequency, ρ_0 is the density of air, $l_{\text{eff}} = l + c_{\text{eff}}w$ is the effective aperture length [104], K is the bulk modulus of air, V is the c-shape's inner volume, and b is the damping. If the characteristic impedance $Z_0 = \rho_0 c$ is considered, the impedance of the meta-grating can be written as

$$Z_{\text{MG}}(\omega) = \left(\frac{1}{Z_{\text{MA}}(\omega)} + \frac{1}{Z_0} \right)^{-1}. \quad (5)$$

In the case, where multiple layers of the meta-grating are involved, this equation can be generalized to

$$Z_{\text{MG}}(\omega) = \left(\sum_{n=1}^N \frac{1}{Z_{\text{MA},n}(\omega)} + \frac{1}{Z_0} \right)^{-1}, \quad (6)$$

where N is the total number of layers and n is the layer identifier. Subsequently, the transmission loss is calculated as

$$\Delta L_p(\omega) = 20 \log_{10} \left(1 - \left| \frac{Z_{\text{MG}}(\omega) - Z_0}{Z_{\text{MG}}(\omega) + Z_0} \right| \right). \quad (7)$$

2.4 Design and fabrication of the metamaterial capsules

2.4.1 Prototype of the metamaterial capsule

The c-shape meta-atom with its dimension is shown in Fig. 6(a). For the prototype capsule following dimensions have been chosen: outer radius $a = 19$ mm, inner radius $r_i = 12$ mm and neck width $w = 5.5$ mm. The prototype capsule has three meta-gratings each consisting of three meta-atoms. Since the meta-grating can only reflect the wave, absorbing walls are placed at the sides opposite to each of the meta-gratings. Following this, the wave is reflected by the meta-grating and afterwards absorbed by the absorbing walls. The capsule structure and the schematic of the wave redirection to the absorbing boundary is sketched in Fig. 6(b).

The photograph of the final prototype is shown in Fig. 6(c) and its outer dimensions are $350 \text{ mm} \times 310 \text{ mm} \times 310 \text{ mm}$. The meta-atoms, the rigid walls and the base are 3D printed using selective laser sintering from polyamide. The assembly was done with bolted joints, where silicone was used to seal the gaps. The absorbing boundary was realized by a 40 mm layer of *Cellofoam 471/SK* [106] attached onto a rigid wall of 10 mm thickness.

2.4.2 Rope drive capsule

To attenuate a particular noise peak emitted by the gear-box of the rope drive system (see Fig. 6(d)) a meta-atom with the new dimensions has been designed: outer radius $a = 42.5$ mm, inner radius $r_i = 32.5$ mm, neck width $w = 10.6$ mm, and lattice constant $d = 110$ mm. The resulting capsule contains only one meta-grating, which is aligned perpendicularly to the motor shaft axis. The meta-grating consists of five meta-atoms, which are additionally separated to avoid vertical modes in the cavity. This results in a meta-grating with the size 590 mm \times 530 mm.

The photograph of the manufactured capsule with gear box and electric motor inside is shown in Fig. 6(e). The meta-atoms are printed from polyamide by selective laser sintering. The body of the capsule is made of 2 mm steel sheets, which are mounted together by bolted joints. All inner walls excluding the meta-grating are covered by *Cellofoam 471/SK* [106] of a thickness 40 mm to create the absorbing boundary similar to the prototype described above. The gaps between the meta-atoms allows for natural ventilation of the gear-box and the electrical motor.

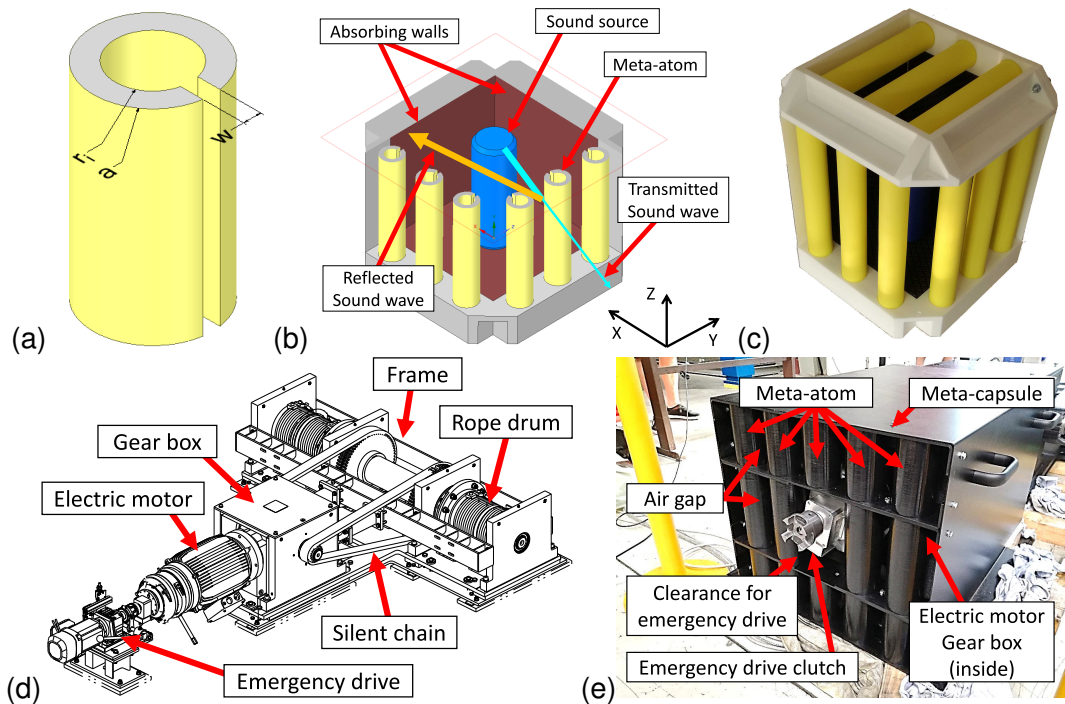


Figure 6: (a) c-shape meta-atom with dimensions. (b) Capsule concept: the sound wave is reflected by the meta-grating consisting of meta-atoms towards the absorbing wall. (c) Photograph of manufactured meta-capsule. (d) Rope drive system with labels. (e) Photograph of the meta-capsule with electric motor and gear box inside. (adapted from Paper [2])

2.5 Numerical modelling of the metamaterial capsule properties

2.5.1 Plane wave transmission through the 2D meta-grating

To determine the transmission of the 2D meta-grating the commercial Finite Element Method (FEM) code ANSYS Multiphysics [107] was used. Only the normally incident plane wave was considered. No lossy impedance boundary conditions have been specified and the thermo-viscous losses have been neglected. The element type was a 20-node fluid element with a quadratic interpolation function. The element size was 1 mm in the neck, in the cavity, and close to the outer walls of the meta-atom. The surrounding domain was meshed with elements of size 3 mm.

2.5.2 Transmission through the capsule prototype

The transmission of the capsule prototype was determined using the in-house 3D Boundary Element Method (BEM) code Akusta [108–110]. The element type was a continuous element with a quadratic interpolation function. The density and acoustic velocity of air were set to $\rho_0 = 1.2 \text{ kg} \cdot \text{m}^{-3}$ and $c = 343 \text{ m} \cdot \text{s}^{-1}$, respectively. As the sound source the geometry of the commercial loudspeaker *Ultimate Ears Boom 2* was modeled and a uniform normal velocity of $1 \text{ m} \cdot \text{s}^{-1}$ was applied. The shape of the loudspeaker is a chamfered cylinder with a diameter of 65 mm and height of 180 mm. Two scenarios have been compared to determine the transmission: the bottom plate with the loudspeaker on it and the loudspeaker inside the capsule. To determine the transmission sound pressure was compared at the reference point $\mathbf{r}_{\text{ref}} = [-1, 0, 0] \text{ m}$. The coordinate axes are shown in Fig. 6(c) and the origin was at the center of the loudspeaker. Furthermore, the source radiated power and the farfield radiated power have been calculated using [111, 112]

$$P = \frac{1}{2} \Re \left\{ \int_{\Gamma} p(x) v_n^*(x) d\Gamma \right\}, \quad (8)$$

where $p(x)$ is sound pressure, $v_n^*(x)$ is the complex conjugate of the normal surface velocity of the fluid and Γ is the fluid-structure interface.

2.5.3 Transmission through the rope drive capsule

The transmission through the rope drive capsule was determined comparing the pressure in the situation with and without the meta-grating mounting. To obtain the sound pressure the in-house BEM code Akusta was applied [108–110]. To model the sound source, a uniform normal surface velocity of $v_n = 1 \text{ m} \cdot \text{s}^{-1}$ was applied over the motor and gear box surfaces. The density and acoustic velocity of air were set to $\rho_0 = 1.2 \text{ kg} \cdot \text{m}^{-3}$ and $c = 343 \text{ m} \cdot \text{s}^{-1}$, respectively. The reference point was located at a distance of 1 m from the meta-grating and was aligned with the motor shaft axis.

2.5.4 Cooling performance of the rope drive capsule

The ventilation performance of the rope drive capsule was determined using the commercial 3D Computational Fluid Dynamics (CFD) code ANSYS Fluent [107]. The heating power was calculated based on the nominal power of the electric motor of 27 kW and the margin of safety $S = 2$ prescribed by the DIN 56950-1:2012-05 stage machinery standard [113]. Application of the efficiency factor of $\eta = 0.94$ for the electric motor results in a heating power of 810 W. Additionally, the gear box has the efficiency factor $\eta = 0.97$, which leads to an additional heating power of 381 W. Modelling a steady state scenario, the steady state heating power is reduced by 0.4 according to periodic duty S3 40% [103], which is common for stage machinery drive trains.

Two situations are compared modelling natural convection induced by the heating power: an airtight capsule and an air-permeable metamaterial capsule. The steady state scenario is considered and the $k-\omega$ SST turbulence model [114, 115] was applied, where the constants have been set as: $\alpha_{\text{inf}} = 1$, $\alpha_{\text{inf}}^* = 0.52$, $\beta_{\text{inf}}^* = 0.09$, $a_1 = 0.31$, $\beta_i^{\text{Inner}} = 0.075$, and $\beta_i^{\text{Outer}} = 0.0828$. The temperature in the environment has been set to 20 °C. The heat transfer coefficient of the acoustic absorber has been set to $0.04 \text{ W} \cdot \text{m}^{-1} \cdot \text{K}^{-1}$ according to the data sheet [106].

The temperature on the surface of the electric model was chosen as the representative parameter. This temperature was compared with Tab. 7 in Ref. [103].

2.6 Experimental determination of transmission through the metamaterial capsules

Capsule prototype. To determine the transmission through the capsule prototype two scenarios have been compared: the bottom plate with the loudspeaker on it and the loudspeaker inside the capsule. The sound pressure was measured using the Bruel&Kjaer hand-held analyzer type 2270, equipped with an 1/2-inch free-field microphone type 4189 and a ZC-0032 preamplifier. The background noise have been checked to stay at least 10 dB below the measured SPL values. The microphone was located at the reference point $\mathbf{r}_{\text{ref}} = [-1, 0, 0] \text{ m}$, which is the same as the one used in numerical simulation. The sound excitation was realized by the commercial loudspeaker *Ultimate Ears Boom 2*.

Rope drive capsule. To determine the transmission through the rope drive capsule two scenarios have been compared: capsule with the meta-grating and capsule with an open side instead of the meta-grating. The sound pressure was measured using the 1/4-inch free-field PCB microphone combined with the Squadriga Frontend (Head Acoustics). The background noise have been checked to stay at least 10 dB below the measured SPL values. The microphone location was 1 m away from the meta-grating and was aligned with the motor shaft axis. The sound excitation was realized by the operation of the motor at rotational speed of approximately 1490 min^{-1} .

2.7 Numerical modeling chain from meshing force fluctuation to Sound Pressure Level (SPL) in the middle of the first row

This modelling chain was applied on three typical stage machinery types: push chain system (see Fig. 7(a)), gear rack system (see Fig. 7(b)), and spiralift system (see Fig. 7(c)). To determine the gear induced excitation the gear meshing process was modelled using the commercial FEM code ANSYS Multiphysics [107]. During the meshing process, the mesh stiffness changes and results in fluctuation of the meshing force [116, 117]. The dynamic bearing forces were determined during quasi-static non-linear structural analysis, where the gear mesh was modelled including non-linear contacts. Subsequently, these forces including time-dependent fluctuations were transferred to frequency domain with harmonic time dependence.

In the subsequent harmonic FEM analysis, the determined time-harmonic forces were used to model the excitation. The modal superposition technique with a preceding modal analysis up to 5000 Hz was used to determine the structural response including the surface velocities up to 2500 Hz. The used material was steel with a Young's modulus of $E_{St} = 200$ GPa, a Poisson ratio of $\nu_{St} = 0.3$ and a density of $\rho_{St} = 7850 \text{ kg} \cdot \text{m}^{-3}$. A representative damping ratio of $\xi = 3 \times 10^{-2}$ was applied in accordance with common recommendations [118]. The critical vibration modes of the modelled stage machinery systems are shown in Fig. 7.

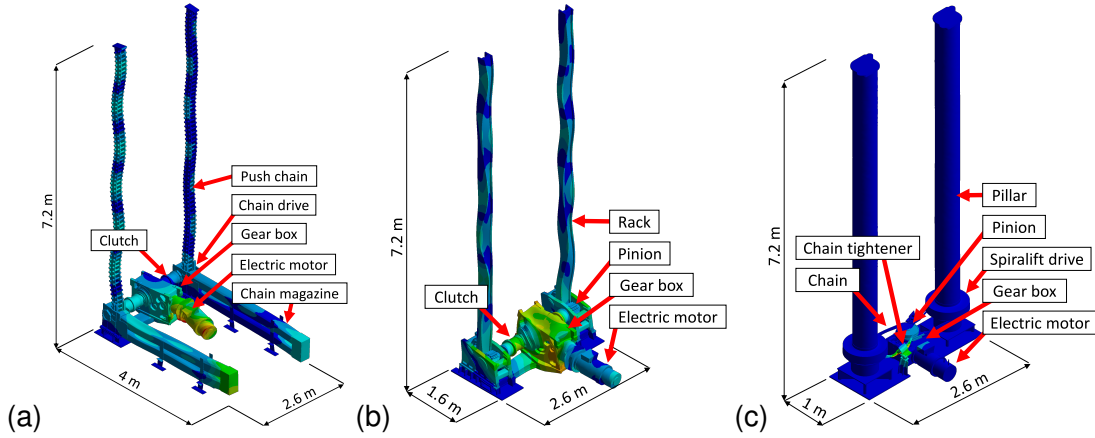


Figure 7: (a) Push chain system showing a vibration mode at 273 Hz. (b) Gear rack system showing a vibration mode at 545 Hz. (c) Spiralift system showing a local vibration mode at 282 Hz. (adapted from **Paper [2]**)

The resulting surface velocities are used to calculate the sound power using the Lumped Parameter Model (LPM) approximation, which is based on the approximation of the Rayleigh integral [111, 119–121]. The discretized version writes as

$$P_{LPM} = \frac{1}{2} k \rho c \sum_{\mu} \sum_{\nu} \frac{\sin(k |\mathbf{r}_{\mu} - \mathbf{r}_{\nu}|)}{2\pi |\mathbf{r}_{\mu} - \mathbf{r}_{\nu}|} \Re \{v_{\mu} v_{\nu}^*\} A_{\mu} A_{\nu}, \quad (9)$$

where k is wave number, ρ is medium density, c is speed of sound, \mathbf{r} is position vector, v is normal velocity at the surface, and A is the surface element area.

The radiated sound power is used in the subsequent geometrical acoustics analysis using the Acoustics Module of COMSOL Multiphysics [122]. This lead to SPL distribution in the auditory and, following this, the transfer function between the drive trains (sound source) and the first row of auditoria (reference point for noise limits). The venue Kraftwerk Mitte in Dresden (Germany) was chosen as the reference object and the 3D geometry of its auditory including stage tower was created using Computed-aided Design (CAD) tools (see the cross-section in Fig. 8). To represent the real reverberation times the absorption coefficients of the walls and chairs have been updated. Furthermore, the model contains additional experimentally determined transmission loss, which results from closing the stage elevator pit when the stage elevator is aligned with the stage [17, 18].

Finally, the determined SPL in the middle of the first row is transferred to octave bands. This is necessary for comparison of the modelled noise emission with the octave band noise limits derived from analog measurements in **Paper [1]**.

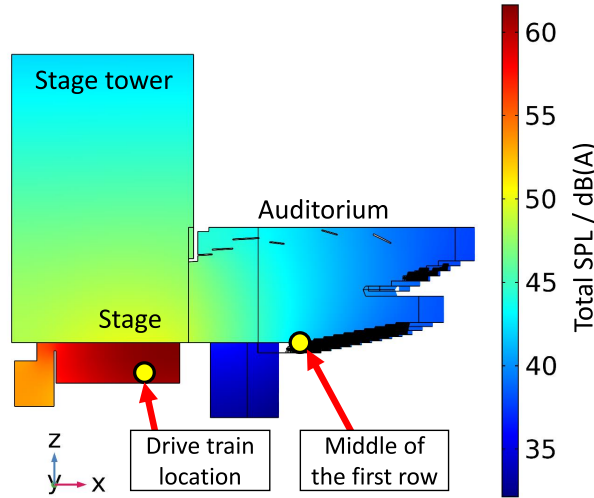


Figure 8: Sound level distribution in the venue Kraftwerk Mitte (Dresden) calculated by geometrical acoustics. (adapted from **Paper [2]**)

2.8 Extraction of polarizability tensor of the meta-atom

The scattering properties of a meta-atom can be described by its polarizability tensor. The polarizability tensor links the properties of the incident wave with monopole and dipole moments

$$\begin{bmatrix} M \\ \mathbf{D} \end{bmatrix} = \boldsymbol{\alpha} \begin{bmatrix} \check{p}^{\text{inc}} \\ \check{\mathbf{v}}^{\text{inc}} \end{bmatrix} = \begin{bmatrix} \alpha^{pp} & \alpha^{pv} \\ \alpha^{vp} & \alpha^{vv} \end{bmatrix} \begin{bmatrix} \check{p}^{\text{inc}} \\ \check{\mathbf{v}}^{\text{inc}} \end{bmatrix}, \quad (10)$$

where M is the scalar monopole moment, \mathbf{D} is the vector dipole moment, $\boldsymbol{\alpha}$ is the polarizability tensor, \check{p}^{inc} and $\check{\mathbf{v}}^{\text{inc}}$ are the incident pressure and the velocity at the center of the meta-atom [71]. The Willis coupling can be read from the off-diagonal terms α^{pv}

and α^{vp} , which represents the cross couplings: velocity vector to monopolar moment and pressure to dipolar vector moment, respectively.

The following extraction method was applied to obtain the polarizability from experiments and from numerical simulations. For simplicity 2D case is considered only and the reduced polarizability relation writes as

$$\begin{bmatrix} M \\ D_x \\ D_y \end{bmatrix} = \begin{bmatrix} \alpha^{pp} & \alpha_x^{pv} & \alpha_y^{pv} \\ \alpha_x^{vp} & \alpha_{xx}^{vv} & \alpha_{xy}^{vv} \\ \alpha_y^{vp} & \alpha_{yx}^{vv} & \alpha_{yy}^{vv} \end{bmatrix} \begin{bmatrix} \check{p}^{\text{inc}} \\ \check{v}_x^{\text{inc}} \\ \check{v}_y^{\text{inc}} \end{bmatrix}. \quad (11)$$

The cylindrical function expansion is used to define the incident pressure p_{inc} by

$$p_{\text{inc}} = \sum_{n=-\infty}^{\infty} \beta_n J_n(kr) e^{in\theta} \quad (12)$$

and scattered pressure p_{scat} by

$$p_{\text{scat}} = \sum_{n=-\infty}^{\infty} \gamma_n H_n^{(1)}(kr) e^{in\theta}, \quad (13)$$

where β_n is incident field coefficient, γ_n is scattered field coefficient, $J_n(kr)$ is Bessel function of order n , $H_n^{(1)}(kr)$ is Hankel function of first kind of order n and r and θ are cylindrical coordinates [10]. Since only monopole and dipole components are considered, the problem reduces to the terms $n = -1, 0, 1$. Subsequently, the incident pressure at the meta-atom center simplifies to

$$\check{p}^{\text{inc}} = \beta_0 \quad (14)$$

and the particle velocity to

$$\check{v}_{x,y}^{\text{inc}} = \frac{\beta_1 \mp \beta_{-1}}{2c\rho_0}. \quad (15)$$

The scattered field allows to obtain the monopole moment as

$$M = \frac{-4\gamma_0}{ik^2c^2} \quad (16)$$

and the dipole moments as

$$D_{x,y} = \frac{-4(\gamma_1 \mp \gamma_{-1})}{ik^3c^2}. \quad (17)$$

Owing to orthogonality of the exponential functions $e^{in\theta}$ the coefficients β_n and γ_n can be calculated directly from experimentally or numerically determined pressure $p_{\text{scat}}(r, \theta)$ as

$$\beta_n = \frac{1}{2\pi J_n(kR^{\text{inc}})} \int_0^{2\pi} p_{\text{inc}}(R^{\text{inc}}, \theta) e^{-in\theta} d\theta \quad (18)$$

and

$$\gamma_n = \frac{1}{2\pi H_n^{(1)}(kR^{\text{scat}})} \int_0^{2\pi} p_{\text{scat}}(R^{\text{scat}}, \theta) e^{-in\theta} d\theta, \quad (19)$$

where R^{inc} and R^{scat} are the constant radii [10]. The incident pressure and velocity from Eqs. (14) and (15) is arranged in an incident matrix Υ of the size $m \times 3$

$$\Upsilon = \begin{bmatrix} \check{p}^{\text{inc}}(\theta_1) & \check{v}_x^{\text{inc}}(\theta_1) & \check{v}_y^{\text{inc}}(\theta_1) \\ \vdots & \vdots & \vdots \\ \check{p}^{\text{inc}}(\theta_m) & \check{v}_x^{\text{inc}}(\theta_m) & \check{v}_y^{\text{inc}}(\theta_m) \end{bmatrix}, \quad (20)$$

with $m \geq 3$. The same procedure is applied on the moments from Eqs. (16) and (17) creating the moment matrix Ξ

$$\Xi = \begin{bmatrix} M(\theta_1) & D_x(\theta_1) & D_y(\theta_1) \\ \vdots & \vdots & \vdots \\ M(\theta_m) & D_x(\theta_m) & D_y(\theta_m) \end{bmatrix}. \quad (21)$$

Finally, the polarizability tensor α is obtained from Υ and Ξ using least squares in matrix form

$$\alpha = (\Upsilon^T \Upsilon)^{-1} \Upsilon^T \Xi. \quad (22)$$

Since \check{p}^{inc} and \check{v}^{inc} , as well as M and \mathbf{D} have different units, it is common to use the normalized polarizability tensor α' , which is defined as

$$\begin{bmatrix} -\sqrt{2}M \\ ikD_x \\ ikD_y \end{bmatrix} = \underbrace{\begin{bmatrix} -2\alpha^{pp} & \frac{-\sqrt{2}}{\rho c} \alpha^{pv} & \frac{-\sqrt{2}}{\rho c} \alpha^{py} \\ ik\sqrt{2}\alpha_x^{vp} & \frac{ik}{\rho c} \alpha_{xx}^{vv} & \frac{ik}{\rho c} \alpha_{xy}^{vv} \\ ik\sqrt{2}\alpha_y^{vp} & \frac{ik}{\rho c} \alpha_{yx}^{vv} & \frac{ik}{\rho c} \alpha_{yy}^{vv} \end{bmatrix}}_{\alpha'} \begin{bmatrix} \frac{1}{\sqrt{2}}\check{p}^{\text{inc}} \\ \rho c \check{v}_x^{\text{inc}} \\ \rho c \check{v}_y^{\text{inc}} \end{bmatrix}, \quad (23)$$

where the off-diagonal terms are anti-symmetric and therefore $\alpha' = \alpha'^T$ [71].

2.9 Numerical modelling of the meta-atom scattering

2.9.1 2D Boundary Element Method (BEM)

One way to determine the polarizability of an arbitrarily shaped meta-atom is to find its scattering properties and to use Eq. (22). The scattering problem was solved using the in-house 2D BEM code written by the author based on the Refs. [108–110, 123]. The element type is a continuous element with quadratic interpolations functions [112]. The discretization is done using the collocation method [123] in combination with an adaptive integration scheme [110]. After collocation following system of equations is solved for \mathbf{p}

$$\mathbf{H}\mathbf{p} = \mathbf{G}\mathbf{v}_{\text{inc}}, \quad (24)$$

where \mathbf{H} and \mathbf{G} are system matrices [110, 123], \mathbf{p} is pressure vector at the boundary, and \mathbf{v}_{inc} is incident velocity vector at the boundary. The boundaries were considered as rigid walls, which explains the missing admittance matrix term in Eq. (24). The used medium density and speed of sound are $\rho_0 = 1.2 \text{ kg} \cdot \text{m}^{-3}$ and $c = 343 \text{ m} \cdot \text{s}^{-1}$.

2.9.2 2D Finite Element Method (FEM) with thermo-viscous losses

The influence of the thermo-viscous losses on the polarizability tensor were determined using the commercial 2D FEM code COMSOL Multiphysics (Acoustics Module) [122]. The used element type is a triangular element with quadratic interpolation functions with the size of approximately 28 elements per wavelength at 2500 Hz. The walls are modelled as acoustically rigid. The air was modelled using the following thermal and viscous coefficients: $\rho_0 = 1.2043 \text{ kg} \cdot \text{m}^{-3}$, $c = 343.14 \text{ m} \cdot \text{s}^{-1}$, $\mu = 1.814 \times 10^{-5} \text{ Pa} \cdot \text{s}$, $\mu_B = 1.0884 \times 10^{-5} \text{ Pa} \cdot \text{s}$, $k = 0.025768 \text{ W} \cdot \text{m}^{-1} \cdot \text{K}^{-1}$, $C_p = 1005.4 \text{ J} \cdot \text{kg}^{-1} \cdot \text{K}^{-1}$, $\alpha_p = 0.0034112 \text{ K}^{-1}$, $\gamma = 1.4$, and $\beta_T = 9.8692 \times 10^{-6} \text{ Pa}^{-1}$.

2.10 Waveguide scattering experiment

To obtain the scattered and incident wave properties from an experiment the 2D anechoic waveguide chamber [10] is used (see Fig. 9(b)). The chamber has a height of 66 mm and supports a single propagation mode below 2600 Hz. Therefore, the system behaves as a 2D waveguide in the frequency range of interest. The sound wave was excited by a speaker and measured by a movable microphone. The microphone was moved between the measurement points in two axes by stepper motors.

The meta-atom sample was manufactured from stainless steel to realize the condition of rigid walls for acoustic waves. The maximum surface roughness was $4 \mu\text{m}$ (Rz4). Rubber sealing was attached to the top and bottom surfaces of the meta-atom to prevent air leakage from the inner cavity. The measurement radius was $R^{\text{inc}} = 40 \text{ mm}$ for the incident field and $R^{\text{scat}} = 200 \text{ mm}$ for the scattered field. The scattered field was measured at 12 different angles of incidence: 0° , 30° , 60° , 90° , 120° , 150° , 180° , 210° , 240° , 270° , 300° , and 330° .

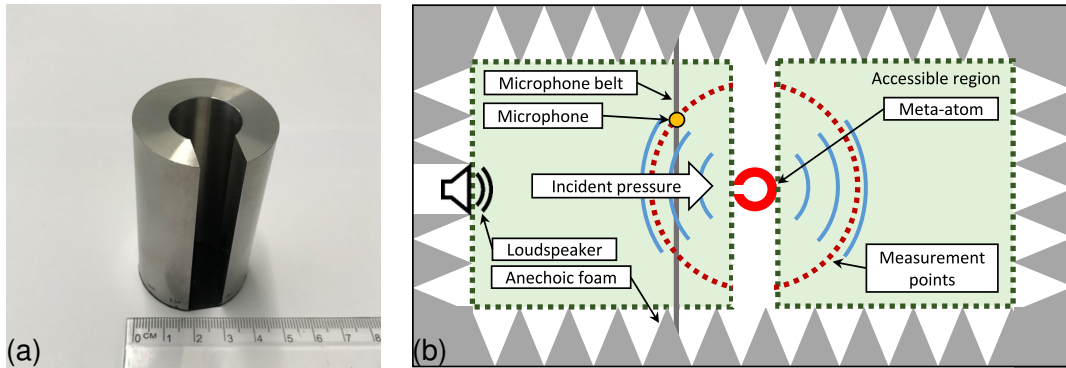


Figure 9: (a) Meta-atom sample made of stainless steel with $a = 20 \text{ mm}$, $r_i = 10 \text{ mm}$, $w = 12 \text{ mm}$ and $h = 66 \text{ mm}$. (b) Schematic of the waveguide scattering experiment. (adapted from **Paper [3]**)

2.11 Analytical modeling of the polarizability of acoustic meta-atoms

2.11.1 Coupling approach

The polarizability of the c-shape meta-atom can be derived analytically introducing the coupling of two different scattering objects: a rigid cylinder (cyl) and a Helmholtz resonator (res)

$$\begin{aligned} \check{p}_{\text{cyl}}^{\text{inc}} &= \check{p}^{\text{inc}} + \check{p}_{\text{res}}^{\text{scat}} \\ \check{p}_{\text{res}}^{\text{inc}} &= \check{p}^{\text{inc}} + \check{p}_{\text{cyl}}^{\text{scat}}. \end{aligned} \quad (25)$$

This approach requires full analytical solution for the scattered field of a cylinder and of a Helmholtz resonator, in other words it requires their polarizability tensors α^{cyl} and α^{res} , respectively. When α^{cyl} and α^{res} are known, Eq. (25) is rearranged to obtain the monopole and dipole moments as

$$\begin{bmatrix} M^{\text{cyl}} \\ D^{\text{cyl}} \\ M^{\text{res}} \\ D^{\text{res}} \end{bmatrix} = \begin{bmatrix} \mathbf{I} & -\alpha^{\text{cyl}}\mathbf{E} \\ -\alpha^{\text{res}}\mathbf{E} & \mathbf{I} \end{bmatrix}^{-1} \begin{bmatrix} \alpha^{\text{cyl}}\mathbf{u}^{\text{inc}} \\ \alpha^{\text{res}}\mathbf{u}^{\text{inc}} \end{bmatrix} \quad (26)$$

with

$$\mathbf{u}^{\text{inc}} = \begin{bmatrix} \check{p}^{\text{inc}} \\ \check{v}_x^{\text{inc}} \end{bmatrix} \quad (27)$$

and

$$\mathbf{E} = \begin{bmatrix} -\frac{ik^2c^2}{4}H_0^{(1)}(ka) & 0 \\ 0 & -\frac{k^2c}{4a\rho_0}H_1^{(1)}(ka) \end{bmatrix}. \quad (28)$$

Finally, from the addition of the monopole and dipole moments of the rigid cylinder and the Helmholtz resonator the polarizability tensor can be obtained

$$\begin{bmatrix} M^{\text{tot}} \\ D^{\text{tot}} \end{bmatrix} = \begin{bmatrix} M^{\text{cyl}} + M^{\text{res}} \\ D^{\text{cyl}} + D^{\text{res}} \end{bmatrix} = \alpha^{\text{tot}}\mathbf{u}^{\text{inc}}. \quad (29)$$

2.11.2 Polarizability of a rigid cylinder

A rigid cylinder scatters a plane wave according to the expansion

$$p^{\text{scat}}(r, \theta) = -p_0 \sum_{n=-\infty}^{\infty} i^n \frac{\frac{d}{d(ka)}J_n(ka)}{\frac{d}{d(ka)}H_n^{(1)}(ka)} H_n^{(1)}(kr) e^{in(\theta-\theta_0)} \quad (30)$$

where $J_n(z)$ is Bessel functions of n -th order, $H_n^{(1)}(z)$ is Hankel function of the second kind of n -th order, a is cylinder radius, θ_0 is angle of incidence, k is wave number, and r and θ are cylindrical coordinates. Since the meta-atom itself and, therefore, the rigid cylinder are small compared to the wavelength only $n = -1, 0, 1$ terms need to be considered

and Eq. (30) simplifies to

$$p^{\text{scat}}(r, \theta) = -p_0 \left(-i \frac{J'_{-1}(ka)}{H_{-1}^{(1)'}(ka)} H_{-1}^{(1)}(kr) e^{-i(\theta-\theta_0)} + \frac{J'_0(ka)}{H_0^{(1)'}(ka)} H_0^{(1)}(kr) + i \frac{J'_1(ka)}{H_1^{(1)'}(ka)} H_1^{(1)}(kr) e^{i(\theta-\theta_0)} \right) \quad (31)$$

or

$$p^{\text{scat}}(r, \theta) = \gamma_{-1} H_{-1}^{(1)}(kr) e^{-i(\theta-\theta_0)} + \gamma_0 H_0^{(1)}(kr) + \gamma_1 H_1^{(1)}(kr) e^{i(\theta-\theta_0)}. \quad (32)$$

Since the scattered field coefficients γ are given, combining Eqs. (11), (16), and (17) leads to the closed form of the polarizability tensor of a rigid cylinder

$$\alpha^{\text{cyl}} = \begin{bmatrix} \frac{4}{ik^2 c^2} \frac{J_1(ka)}{H_1^{(1)}(ka)} & 0 \\ 0 & \frac{8\rho_0}{k^3 c} \frac{J'_1(ka)}{H_1^{(1)'}(ka)} \end{bmatrix}. \quad (33)$$

2.11.3 Polarizability of a Helmholtz resonator

The dynamical behavior of A Helmholtz resonator is described by the differential equation

$$c_n^{\text{rad}} \frac{\rho_0 A_n}{8\pi c} \frac{d^3 \xi_n}{dt^3} - \rho_0 l_n^{\text{eff}} \frac{d^2 \xi_n}{dt^2} - \frac{K}{V} \sum_m A_m \xi_m = p_n^{\text{ext}}, \quad (34)$$

which is converted to an algebraic equation using $e^{-i\omega t}$

$$i\omega^3 c_n^{\text{rad}} \frac{\rho_0 A_n}{c} \xi_n + \omega^2 \rho_0 l_n^{\text{eff}} \xi_n - \frac{K}{V} \sum_m A_m \xi_m = p_n^{\text{ext}}, \quad (35)$$

where ξ_n is outward directed particle displacement at aperture n , p_n^{ext} is external pressure at aperture n , ρ_0 is medium density, c is speed of sound, $A_n = w_n$ is cross-section of the aperture, $K = c^2 \rho_0$ is bulk modulus, V is inner cavity volume, $l_n^{\text{eff}} = l + c_n^{\text{eff}}$ is effective neck length [104], and c_n^{rad} is radiative loss coefficient. Equation (35) can be rearranged to

$$\mathbf{K}_{\text{eq}} \boldsymbol{\xi} = \mathbf{p}^{\text{ext}}, \quad (36)$$

where \mathbf{K}_{eq} is the dynamic stiffness matrix. After several steps, which are described in the Supplementary Information accompanying **Paper [3]** in detail, the polarizability tensor is obtained. For a Helmholtz resonator with two apertures it writes as

$$\alpha^{\text{res}} = \rho_0 \begin{bmatrix} A_1 & A_2 \\ x_1 A_1 & x_2 A_2 \end{bmatrix} \mathbf{K}_{\text{eq}}^{-1} \begin{bmatrix} 1 & -ia\rho_0\omega \\ 1 & ia\rho_0\omega \end{bmatrix} \quad (37)$$

and for one with a single aperture as

$$\boldsymbol{\alpha}^{\text{res}} = \frac{\rho_0 \begin{bmatrix} A_1 & -ia\rho_0\omega A_1 \\ x_1 A_1 & -ia\rho_0\omega x_1 A_1 \end{bmatrix}}{i\omega^3 c^{\text{rad}} \frac{\rho_0 A_1}{\pi c} + \omega^2 \rho_0 l_1^{\text{eff}} - \frac{K}{V} A_1}. \quad (38)$$

Coupling of the polarizability of the Helmholtz resonator with a single aperture with the rigid cylinder using Eqs. (26)-(29) gives the polarizability of c-shape meta-atom.

3 Paper Summary

3.1 Paper [1]

“Sound pressure level limits for stage machinery noise in operas and theaters”

Introduction. In the introduction of this paper the noise conditions in auditoria are discussed. The widespread noise criteria are revisited and their application to stage machinery is discussed. Recent research particularly on stage machinery noise is reviewed and compared with noise requirements of tender documents.

Method. The measurement technique and equipment for measurements during live performances in occupied halls are demonstrated. The choice of proper venues to achieve a quality standard from the acoustics points of view is elaborated. Furthermore, the selected pieces demonstrating a variety in styles and epochs are listed. Three possible techniques for background noise identification of collected data are proposed: minimum 1s-averaged level, Gaussian mixture model and N% exceedance level. The details about applicability of these methods are given including their drawbacks and benefits.

Results. The collected data of 12 performances with an overall duration of 22 h is separated into opera, ballet and drama performance type. The previously discussed metrics are applied on each performance and on each piece type separately. The cumulative density of the noise and the metric results are presented in figures and tables. Additionally, the background noise of unoccupied halls is included in the figures.

Discussion. The reproducibility of the level metrics is analyzed based on comparison of the two takes of one piece on two different days. The stage machinery imperceptibility probability is analyzed from the point of view of realistic stage machinery usage rate. Considering practical implications, background spectra obtained from minimum 1s-averaged metric and N% exceedance metric are proposed as stage machinery noise limits. The limiting factors of the proposed approach are discussed.

3.2 Paper [2]

“Acoustic metamaterial capsule for reduction of stage machinery noise”

Introduction. This paper starts with brief information on typical noise control issues linked to machinery noise. The concept of acoustic metamaterials is presented and their promising properties are pointed out. Recent developments particularly in noise control by air permeable acoustic metamaterials are reviewed. However, there is a lack of application in industrial noise control projects, where one of the reasons could be the complexity of the geometry. Therefore, an easily manufacturable c-shape meta-atom is used in the following to apply a metamaterial noise capsule on stage machinery.

Meta-capsule prototype. In this section a 2D meta-grating with the transmission loss peak at 1500 Hz is designed. The simple c-shape structure allows to derive an analytical model and to calculate the transmission based on impedance modeling. Subsequently, the 2D design is expanded to a full 3D meta-capsule. The transmission properties of the meta-capsule are determined numerically. Furthermore, the meta-capsule is manufactured using 3D printing techniques and investigated experimentally showing good agreement with the numerical results. The presence of the acoustic Purcell effect is demonstrated, where additional broad band attenuation is the result.

Design and experimental validation in application. In the following, a meta-capsule is designed to reduce the noise caused by the gear-box of the rope drive system. The transmission loss of the meta-capsule is calculated numerically. A prototype is manufactured and its transmission properties are determined experimentally demonstrating the existence of the transmission loss peak caused by the meta-grating. The cooling properties of the meta-capsule are verified by numerical fluid dynamics showing the feasibility of the design for cooling of the covered electric drive by natural convection only.

Modelling of stage machinery noise. This section presents numerical modelling of the noise emission of three typical stage machinery drive trains. The numerical modeling chain includes quasi-static gear mesh, harmonic response of the whole drive assembly, sound power determination by lumped parameter model, and projection from the machinery location to the middle of the first row in auditoria by geometrical acoustics. The comparison of the noise emission reveals several limit violations, which can be tracked back to distinct noise peaks in the frequency spectra. Multilayer meta-capsules are designed and tailored to block critical peaks, hence the limits violation is resolved in most cases.

Discussion. The deviations between the results from the BEM simulation and from experiments in the case of the meta-capsule for the rope drive system are discussed. Additionally, the meta-grating performance is compared to the sonic crystal approach using the same c-shape geometry. Although the performance of the sonic crystal can be improved, its thickness being bigger as the wavelength makes it less attractive for the noise control of machinery. It is noted that the designed meta-grating is only 0.15λ .

3.3 Paper [3]

“Acoustic meta-atom with experimentally verified maximum Willis coupling”

Introduction. This paper starts with a review of exciting properties of acoustic metamaterials beyond simple noise control applications. The concept of Willis coupling and its function in constitutive relation of elastic and acoustic waves is briefly described. The Willis coupling magnitude has a bound resulting from conservation of energy, however, this limit was not tested experimentally.

Results.

Meta-atom design. In this section the derivation of the c-shape structure is presented. This structure is easily manufacturable, avoids thin channels and can reach Willis coupling up-to the theoretical bound.

Experimental verification. The polarizability of the c-shape meta-atom is determined experimentally by the waveguide scattering experiment. The sample demonstrates strong Willis coupling achieving 90 % of the theoretical bound.

Polarizability theory. The polarizability theory of the c-shape meta-atom is derived. This allows to calculate the polarizability tensor from Helmholtz resonator dynamics. Experiment, BEM simulation, and polarizability theory shows great agreement in the Willis coupling magnitude.

Discussion. Numerically calculated Willis coupling results for lossy and lossless scenarios are compared. Furthermore, the performance of the c-shape meta-atom in the lossy case is compared with another design showing strong Willis coupling. In addition, the tailoring capabilities of the double aperture meta-atom are demonstrated and discussed.

Methods. The extraction method of polarizability tensor from the experiment and numerical simulation is described. The used numerical modeling techniques and modeling parameters are reported. The details on waveguide scattering experiment are given.

Paper C is accompanied by Supplementary Notes including the complete derivation of the analytical model.

4 Discussion of Results

4.1 Paper [1]

“Sound pressure level limits for stage machinery noise in operas and theaters”

Review of previous research on audience noise demonstrates, that the data on opera theaters, where stage machinery is usually supposed to act, is sparse [20, 21, 31–34, 92]. Although Ref. [20] contains a single opera venue measurement, it is not sufficient to draw reasonable conclusions on stage machinery noise limits. Therefore, the presented audience noise measurements during 12 live performances with occupied auditory are a significant contribution to the research on audience noise and venue acoustics.

Furthermore, stage machinery noise is underrepresented in the research area of technical acoustics in general. The proposed stage machinery noise limits reach beyond the previous studies [35, 38, 39] by providing octave limits in a broad frequency range comparable with the state of the art noise criteria [22–28]. Ref. [35] formulates limits in total levels and is based on subjective evaluation of the noise of stage machinery installations build before 1998. Subsequently, there are some doubts if these results can still match the expectations of the modern opera and drama venues.

One of the most important limitations of the presented study is the small number of measurements. It is challenging to get access to the middle of the first row of almost fully occupied auditoria during day-to-day business of performing venues. Although the considered performance number is bigger or comparable to the numbers in relevant publications [20, 21, 34, 92], it is still relatively small from the statistical point of view. It is desirable to increase this number and to include additional venues and pieces in future contributions.

An additional aspect, which can be targeted in future work is the perceptual evaluation of the stage machinery noise in the presence of performance sound or continuous building noise. Furthermore, the ability of the human brain to separate multiple sound sources through binaural hearing was not considered in this study and can be investigated to improve the proposed requirements.

4.2 Paper [2]

“Acoustic metamaterial capsule for reduction of stage machinery noise”

This paper demonstrates the design, modelling and simulation of acoustic metamaterial capsules applied on noise control of stage machinery. A lot of work has been done on acoustic metamaterials, where a broad range of wave manipulating opportunities have been demonstrated [16, 41–51, 124, 125]. Particularly in the context of noise control of machinery, three additional aspect besides the transmission loss are of high importance: economic manufacturing, power train cooling, and required space.

Economic manufacturing. To facilitate economic manufacturing, a meta-grating consisting of simple c-shape meta-atoms has been proposed. This is a significant improvement comparing to meta-atoms with meander shape structures from the view of manufacturability and of viscous boundary losses [10, 15, 71, 80–83]. The proposed structure can be fabricated using 3D-printing techniques, milled from a bulk material, or produced by slicing a pipe profile.

Power train cooling. To enable cooling of the active machinery components it is necessary to allow air flow through the noise barrier. Acoustic metamaterials linked with air flow capabilities have been proposed in recent studies [15, 52–64], however, none of them consider specific characteristics of machinery noise and have been approved in realistic application environment. The metamaterial capsule proposed here combines reduced transmission with sufficient air flow for cooling of real power train, which is a novelty compared to the literature. Additionally, the effect of meta-grating could be shown on a real stage machinery drive train.

Space requirements. To meet the space requirements only a single layer of c-shape meta-atoms has been used to design the sound barrier with sufficient attenuation performance. The resulting meta-grating thickness is only 0.15 times the wavelength of the acoustic wave and is therefore comparable with the meander shape geometries of deep sub-wavelength size [15]. The proposed design shows excellent performance-to-space ratio in comparison to the sonic crystal approach, which requires much more space [46].

An additional aspect resulting from the simplicity of the structure is the capability of analytical modelling. The response of the meta-atom can be described by the Helmholtz resonator dynamics and the transmission loss of the meta-grating can be calculated by the network theory. In the Section *Modelling of stage machinery noise* an additional novel aspect is presented: the complex multi-physics model chain. This chain includes nonlinear structural mechanics including large deformation and contacts, time-harmonic structural dynamics, time-harmonic acoustics (FEM and BEM), lumped parameter modelling of radiated sound power, impedance modelling of sound transmission, and geometrical acoustics. This approach allowed to model the sound radiation of the stage machinery to the point, where it can be compared with real noise requirements. Finally, this demonstrates a way to engineer a metamaterial sound barrier based on the noise spectra and noise requirements to make it usable in application.

The most important limitation of this approach is that the strong transmission loss properties can be reached only in a narrow band region. To solve this a tailored multi-layer meta-grating design is proposed and modelled. If the critical peaks of the noise spectra can be identified or at least predicted, the required meta-grating can be designed using the impedance model proposed in this manuscript.

4.3 Paper [3]

“Acoustic meta-atom with experimentally verified maximum Willis coupling”

This paper focuses on a c-shape meta-atom and demonstrates its unique property of maximum Willis coupling numerically, analytically and experimentally. Willis coupling is a constitutive relation term, which couples kinetic and potential energy in a medium [73–75]. Furthermore, it is an acoustic analog to the bianisotropy in electromagnetism, which can enhance exotic properties of electromagnetic metamaterials [76–79].

Experimental evidence of Willis coupling has been reported [70, 85, 86] and it has been shown that Willis coupling has a theoretical bound by conservation of energy [71]. However, none of these studies demonstrates Willis coupling approaching its maximum in an experiment. A design with meander shape geometry has been numerically demonstrated to reach the theoretical bound [71], however, due to thin channels its performance is reduced particularly in the sub-wavelength range [82, 83]. Due to the reduced boundary layer losses in the c-shape geometry, the proposed meta-atom can outperform the previous design in a numerical simulation including thermo-viscous losses. Subsequently, the c-shape has been shown to reach 90% of the theoretical bound of Willis coupling in a waveguide scattering experiment [10]. To this point such values haven't been demonstrated and it was unknown, if it is possible to achieve such strong Willis coupling in real structures including losses, imperfections and manufacturing tolerances.

An additional novel aspect of this work is the analytical modeling of the polarizability tensor including Willis coupling terms. Due to the simplicity of the proposed c-shape meta-atom the response properties can be derived based on Helmholtz resonator dynamics. This allows to calculate the polarizability of the meta-atom starting from its geometry with a single or with multiple apertures. Introducing a second aperture and varying its neck width was shown to effectively tailor the Willis coupling magnitude from zero to its theoretical maximum. It also should be noted, that the manufacturability of the c-shape structure facilitates further experimental investigation of Willis coupling in acoustic media.

Recently, a novel numerical approach was developed allowing for the analysis of normal modes of the acoustic meta-atoms in infinite domain [126–128]. This approach is particularly interesting when finite arrays of meta-atoms have to be studied [128]. Additionally, it allows to consider boundary admittance of the meta-atom walls. In the preprint version [11] of **Paper [3]** it has been shown, that boundary admittance can change the performance of the meta-atoms. Reference [128] demonstrates the potential of the technique for c-shape geometries in open space. In future work it could be beneficial to further investigate the properties of c-shape meta-atoms and finite meta-grating using this method.

In an ongoing research the bianisotropy of acoustic media has been used to design low-frequency acoustic antennas [129] and cloaking devices [130]. Furthermore, Willis coupling has also been demonstrated in moving media [131]. The coupling possibilities of constitutive relations have been further elaborated and an engineered electro-momentum

coupling has been proposed [132]. A review paper on non-traditional wave manipulation including a discussion on Willis coupling was recently published [133].

5 Conclusion

This work contributes to the field of noise control and acoustic metamaterials. The aim is to increase the quality of the stage machinery considering noise emission using acoustic metamaterials and to improve the performance of the acoustic metamaterials.

The state of the art in noise requirements in auditoria has been reviewed and was considered as not sufficient for stage machinery noise limits. Measurements during live performances have been conducted and the quietest moments during the performance have been characterized using different noise metrics. Finally, sound pressure limits for stage machinery have been derived.

To fulfill the noise limits, an acoustic metamaterial capsule concept using c-shape meta-atoms was proposed. Two different designs have been manufactured and validated numerically and experimentally providing promising results. Furthermore, an analytical model was derived from the single meta-atom as part of the metamaterial. This model allowed to design multi-layer meta-gratings to tailor the transmission loss spectra to the simulated emission spectra of three common stage machinery installations. The resulting sound pressure level in the first row of auditoria fulfills the noise limits stated previously.

For a deeper understanding of the properties of a single c-shape meta-atom its polarizability was investigated analytically, numerically and experimentally. The thermo-viscous losses are reduced due to the avoidance of long and thin channels and the c-shape meta-atom demonstrates better scattering efficiency. Subsequently, the Willis coupling of the c-shape meta-atom was demonstrated to reach 90 % of theoretical bound in an experiment.

The derived stage machinery noise limits provide a detailed criterion for the optimization of stage machinery, but also of other stage equipment or HVAC. Such criterion is a tool, which helps engineers, planners, and theater directors during the project and design process of stage machinery installation. The acoustic metamaterial capsule concept gives an approach how the noise emission spectra of stage machinery can be engineered, while the cooling by natural convection is still possible. It demonstrates a novel noise control method for stage machinery, which helps to improve the quality of stage logistics and, subsequently, of the art performance itself. The c-shape meta-atom is easily manufacturable and can be modelled analytically. As shown in this work, the simple c-shape demonstrates strong properties, which are useful for noise control and other extraordinary metamaterial designs. The simplicity of the geometry helps to use acoustic metamaterials in industrial applications and increases the general accessibility of metamaterials in experiments.

References

- [1] A. Melnikov, I. Witew, M. Maeder, M. Gatt, M. Scheffler, and S. Marburg. “Sound pressure level limits for stage machinery noise in operas and theaters”. In: *Applied Acoustics* 156 (Dec. 15, 2019), pp. 29–39.
- [2] A. Melnikov, M. Maeder, N. Friedrich, Y. Pozhanka, A. Wollmann, M. Scheffler, S. Oberst, D. Powell, and S. Marburg. “Acoustic metamaterial capsule for reduction of stage machinery noise”. In: *The Journal of the Acoustical Society of America* 147.3 (Mar. 1, 2020). Publisher: Acoustical Society of America, pp. 1491–1503.
- [3] A. Melnikov, Y. K. Chiang, L. Quan, S. Oberst, A. Alù, S. Marburg, and D. Powell. “Acoustic meta-atom with experimentally verified maximum Willis coupling”. In: *Nature Communications* 10.1 (July 17, 2019), p. 3148.
- [4] A. Melnikov. “Geräuschlos bewegen, Ansätze zur Reduzierung der Schallemission der Untermaschinerie [Silent Movement, Approaches for Noise Reduction of understage Machinery]”. In: *Bühnentechnische Rundschau Sonderband [Stage Machinery Review, Special Edition]* (2015), pp. 36–39.
- [5] A. Melnikov, M. Scheffler, and S. Marburg. “Untersuchungen eines Bühnenpodiums hinsichtlich der Reduktion von Geräuschemission [Investigations of a stage elevator concerning noise reduction]”. In: *Proceedings of DAGA2017 Kiel* (2017).
- [6] A. Melnikov, M. Scheffler, and S. Marburg. “Sound Radiation of Stage Elevators with ANSYS and Boundary Element Method”. In: *Proc. of CADFEM ANSYS Simulation Conference* (2017).
- [7] A. Melnikov, M. Maeder, M. Gatt, M. Scheffler, and S. Marburg. “Development of a novel sound pressure level requirement for characterizing noise disturbances from theater and opera stages”. In: *Proceedings of Meetings on Acoustics* 30.1 (2017), p. 030013. eprint: <http://asa.scitation.org/doi/pdf/10.1121/2.0000638>.
- [8] A. Melnikov, I. Witew, M. Maeder, M. Gatt, M. Scheffler, and S. Marburg. “Limits for Stage Machinery Noise”. In: *INTER-NOISE and NOISE-CON Congress and Conference Proceedings*. Chicago, IL, 2018, 1672–1677(6).
- [9] A. Melnikov, I. B. Witew, M. Mäder, M. Gatt, M. Scheffler, and S. Marburg. “Stage machinery noise - What limits are appropriate?” In: *Proceedings of the Institute of Acoustics*. Auditorium Acoustics 2018. Vol. 40., Pt. 3. 2018. Hamburg, 2018, pp. 625–628.
- [10] J. Jordaan, S. Punzet, A. Melnikov, A. Sanches, S. Oberst, S. Marburg, and D. A. Powell. “Measuring monopole and dipole polarizability of acoustic meta-atoms”. In: *Applied Physics Letters* 113.22 (Nov. 26, 2018), p. 224102.
- [11] A. Melnikov, L. Quan, S. Oberst, A. Alù, S. Marburg, and D. Powell. “Acoustic meta-atom with maximum Willis coupling”. In: *arXiv:1812.02318 [physics]* (Dec. 5, 2018). arXiv: 1812.02318.

- [12] R. Martínez-Sala, J. Sancho, J. V. Sánchez, V. Gómez, J. Llinares, and F. Meseguer. “Sound attenuation by sculpture”. In: *Nature* 378.6554 (Nov. 1995). Number: 6554 Publisher: Nature Publishing Group, pp. 241–241.
- [13] A. O. Krushynska. “Between Science and Art: Thin Sound Absorbers Inspired by Slavic Ornaments”. In: *Frontiers in Materials* 6 (2019). Publisher: Frontiers.
- [14] A. O. Krushynska, A. Amendola, F. Bosia, C. Daraio, N. M. Pugno, and F. Fraternali. “Accordion-like metamaterials with tunable ultra-wide low-frequency band gaps”. In: *New Journal of Physics* 20.7 (July 2018). Publisher: IOP Publishing, p. 073051.
- [15] Y. Cheng, C. Zhou, B. G. Yuan, D. J. Wu, Q. Wei, and X. J. Liu. “Ultra-sparse metasurface for high reflection of low-frequency sound based on artificial Mie resonances”. In: *Nature Materials* 14.10 (Oct. 2015), pp. 1013–1019.
- [16] S. A. Cummer, J. Christensen, and A. Alù. “Controlling sound with acoustic metamaterials”. In: *Nature Reviews Materials* 1.3 (Mar. 2016), p. 16001.
- [17] B. Grösel. *Bühnentechnik: Mechanische Einrichtungen [Stage Machinery: Mechanical Installations]*. De Gruyter, 2015.
- [18] T. Ogawa. *Theatre Engineering and Stage Machinery*. Consultancy series. Entertainment Technology Press, 2001.
- [19] H. Ren, J. Zhang, W. Jiang, and Z. Su. “Measurement Method of Background Noise in Theatre Based on Stage Machinery”. In: *2010 Third International Joint Conference on Computational Science and Optimization*. 2010 Third International Joint Conference on Computational Science and Optimization. Vol. 2. ISSN: null. May 2010, pp. 452–455.
- [20] C.-H. Jeong, P. Marie, J. Brunskog, and C. Møller Petersen. “Audience noise in concert halls during musical performances”. In: *The Journal of the Acoustical Society of America* 131.4 (Apr. 1, 2012), pp. 2753–2761.
- [21] M. Kleiner. “On the Audience Induced Background Noise Level in Auditoria”. In: *Acta Acustica united with Acustica* 46.1 (Sept. 1, 1980), pp. 82–88.
- [22] L. L. Beranek. “Revised Criteria for Noise in Buildings”. In: *Noise Control* 3.1 (Jan. 1, 1957), pp. 19–27.
- [23] L. Vér I. and L. Beranek L. *Noise and vibration control engineering: principles and applications*. John Wiley & Sons, 2006.
- [24] L. Beranek L., E. Blazier W., and J. Figwer J. “Preferred Noise Criterion (PNC) Curves and Their Application to Rooms”. In: *The Journal of the Acoustical Society of America* 50.5A (1971), pp. 1223–1228. eprint: <https://doi.org/10.1121/1.1912760>.
- [25] *ISO 1996-1:2016-03: Acoustics - Description, measurement and assessment of environmental noise - Part 1: Basic quantities and assessment procedures*. ISO International Organization for Standardization, 2016.

- [26] L. L. Beranek. "Balanced noise-criterion (NCB) curves". In: *Journal of the Acoustical Society of America* 86.2 (1989), pp. 650–664.
- [27] *ANSI S12.2:1995 Criteria for Evaluating Room Noise*. American National Standard Institute, 1995.
- [28] W. E. Blazier. "Revised noise criteria for design and rating of HVAC systems". In: *Noise Control Engineering Journal* 16 (1981), pp. 64–73.
- [29] M. Barron. *Auditorium Acoustics and Architectural Design*. Taylor & Francis, 2009.
- [30] T. D. Rossing. *Springer Handbook of Acoustics*. Springer New York, 2014.
- [31] A. Mueller W. "Audience noise as a limitation to the permissible volume range of dialog in sound motion pictures". In: *Journal of the Society of Motion Picture Engineers* 35.7 (1940), pp. 48–58.
- [32] M. Hodgson, R. Rempel, and S. Kennedy. "Measurement and prediction of typical speech and background-noise levels in university classrooms during lectures". In: *Journal of the Acoustical Society of America* 105.1 (Jan. 1999), pp. 226–233.
- [33] J. C. Steinberg. "The Stereophonic Sound Film System - Pre- and Post-Equalization of Compandor Systems". In: *Journal of the Acoustical Society of America* 13.2 (1941), pp. 107–114.
- [34] P. Marie. "Background noise requirements and audience noise in performance spaces". MA thesis. Technical University of Denmark, 2009.
- [35] H.-P. Tennhardt. "Grenzwerte der Schallimmission buehnentechnischer Anlagen [Limits for Noise Immission of Stage Machinery Installations]". In: *IEMB Infoblaetter* 5 (1998).
- [36] W. Schirmer and O. Ulrich. "Beating technology noise". In: *ABTT* 3 (2002).
- [37] W. Schirmer. "Zur Ermittlung des Standes der Technik für geräuscharme Bühnenpodien [Review of low-noise Stage Elevators]". In: *DAGA Proceedings* (2003).
- [38] Z. Su, B. Liu, J. Liu, H. Ren, and F. Wei. "Research on emission noise measurement of stage machinery in performing place". In: *AIP Conference Proceedings* 2036.1 (Nov. 12, 2018). Publisher: AIP Publishing LLC, p. 030034.
- [39] J. J. Zhang, Y. J. Jiang, Z. B. Su, and H. Ren. "Measurement and Research on Stage Machinery Noise in Theatre". In: *Advanced Materials Research*. Conference Name: Manufacturing Process and Equipment ISBN: 9783037856932 ISSN: 1662-8985 Library Catalog: www.scientific.net Pages: 399-402 Publisher: Trans Tech Publications Ltd Volume: 694-697. 2013.
- [40] R. Harris. "The drama of the silent move: control of noise from stage machinery in the Operaen Copenhagen". In: *Proceedings of the Institute of Acoustics* 27.2 (2005).
- [41] N. Fang, D. Xi, J. Xu, M. Ambati, W. Srituravanich, C. Sun, and X. Zhang. "Ultra-sonic metamaterials with negative modulus". In: *Nature Materials* 5.6 (June 2006), pp. 452–456.

- [42] Z. Liu, X. Zhang, Y. Mao, Y. Y. Zhu, Z. Yang, C. T. Chan, and P. Sheng. “Locally Resonant Sonic Materials”. In: *Science* 289.5485 (Sept. 8, 2000), pp. 1734–1736.
- [43] M. Ambati, N. Fang, C. Sun, and X. Zhang. “Surface resonant states and super-lensing in acoustic metamaterials”. In: *Physical Review B* 75.19 (May 31, 2007).
- [44] S. Zhang, L. Yin, and N. Fang. “Focusing Ultrasound with an Acoustic Metamaterial Network”. In: *Physical Review Letters* 102.19 (May 15, 2009), p. 194301.
- [45] D. Torrent and J. Sánchez-Dehesa. “Acoustic metamaterials for new two-dimensional sonic devices”. In: *New Journal of Physics* 9.9 (2007), p. 323.
- [46] D. P. Elford, L. Chalmers, F. V. Kusmartsev, and G. M. Swallowe. “Matryoshka locally resonant sonic crystal”. In: *The Journal of the Acoustical Society of America* 130.5 (Nov. 2011), pp. 2746–2755.
- [47] S. M. B. Fard, H. Peters, S. Marburg, and N. Kessissoglou. *Acoustic Performance of a Barrier Embedded With Helmholtz Resonators Using a Quasi-Periodic Boundary Element Technique*. June 2017. URL: <https://www.ingentaconnect.com/content/dav/aaau/2017/00000103/00000003/art00012> (visited on 07/21/2019).
- [48] J. Henneberg, A. Gerlach, H. Storck, H. Cebulla, and S. Marburg. “Reducing mechanical cross-coupling in phased array transducers using stop band material as backing”. In: *Journal of Sound and Vibration* 424 (June 23, 2018), pp. 352–364.
- [49] J. Henneberg, A. Gerlach, H. Cebulla, and S. Marburg. “The potential of stop band material in multi-frequency ultrasonic transducers”. In: *Journal of Sound and Vibration* 452 (July 21, 2019), pp. 132–146.
- [50] C. Claeys, E. Deckers, B. Pluymers, and W. Desmet. “A lightweight vibro-acoustic metamaterial demonstrator: Numerical and experimental investigation”. In: *Mechanical Systems and Signal Processing* 70-71 (Mar. 1, 2016), pp. 853–880.
- [51] P. Marinova, S. Lippert, and O. von Estorff. “On the numerical investigation of sound transmission through double-walled structures with membrane-type acoustic metamaterials”. In: *The Journal of the Acoustical Society of America* 142.4 (Oct. 1, 2017), pp. 2400–2406.
- [52] G. Ma, M. Yang, Z. Yang, and P. Sheng. “Low-frequency narrow-band acoustic filter with large orifice”. In: *Applied Physics Letters* 103.1 (July 1, 2013), p. 011903.
- [53] F. Langfeldt, H. Kemsies, W. Gleine, and O. von Estorff. “Perforated membrane-type acoustic metamaterials”. In: *Physics Letters A* 381.16 (Apr. 25, 2017), pp. 1457–1462.
- [54] Z. Chen, L. Fan, S.-y. Zhang, H. Zhang, X.-j. Li, and J. Ding. “An open-structure sound insulator against low-frequency and wide-band acoustic waves”. In: *Applied Physics Express* 8.10 (Sept. 30, 2015), p. 107301.
- [55] H.-l. Zhang, Y.-f. Zhu, B. Liang, J. Yang, J. Yang, and J.-c. Cheng. “Omnidirectional ventilated acoustic barrier”. In: *Applied Physics Letters* 111.20 (Nov. 13, 2017), p. 203502.

- [56] R. Ghaffarivardavagh, J. Nikolajczyk, S. Anderson, and X. Zhang. “Ultra-open acoustic metamaterial silencer based on Fano-like interference”. In: *Physical Review B* 99.2 (Jan. 4, 2019), p. 024302.
- [57] X. Yu, Z. Lu, T. Liu, L. Cheng, J. Zhu, and F. Cui. “Sound transmission through a periodic acoustic metamaterial grating”. In: *Journal of Sound and Vibration* 449 (June 9, 2019), pp. 140–156.
- [58] C. Shen, Y. Xie, J. Li, S. A. Cummer, and Y. Jing. “Acoustic metacages for sound shielding with steady air flow”. In: *Journal of Applied Physics* 123.12 (Mar. 23, 2018), p. 124501.
- [59] X. Wu, C. Fu, X. Li, Y. Meng, Y. Gao, J. Tian, L. Wang, Y. Huang, Z. Yang, and W. Wen. “Low-frequency tunable acoustic absorber based on split tube resonators”. In: *Applied Physics Letters* 109.4 (July 25, 2016), p. 043501.
- [60] X. Wu, K. Y. Au-Yeung, X. Li, R. C. Roberts, J. Tian, C. Hu, Y. Huang, S. Wang, Z. Yang, and W. Wen. “High-efficiency ventilated metamaterial absorber at low frequency”. In: *Applied Physics Letters* 112.10 (Mar. 5, 2018), p. 103505.
- [61] T. Lee, T. Nomura, E. M. Dede, and H. Iizuka. “Ultrasparse Acoustic Absorbers Enabling Fluid Flow and Visible-Light Controls”. In: *Physical Review Applied* 11.2 (Feb. 8, 2019), p. 024022.
- [62] X. Xiang, X. Wu, X. Li, P. Wu, H. He, Q. Mu, S. Wang, Y. Huang, and W. Wen. “Ultra-open High-efficiency Ventilated Metamaterial Absorbers with Customized Broadband Performance”. In: *arXiv:1911.05969 [physics]* (Nov. 14, 2019). arXiv: 1911.05969.
- [63] S.-H. Kim and S.-H. Lee. “Air transparent soundproof window”. In: *AIP Advances* 4.11 (Nov. 1, 2014), p. 117123.
- [64] Y. Ge, H.-x. Sun, S.-q. Yuan, and Y. Lai. “Switchable omnidirectional acoustic insulation through open window structures with ultrathin metasurfaces”. In: *Physical Review Materials* 3.6 (June 11, 2019), p. 065203.
- [65] S. Zhang, C. Xia, and N. Fang. “Broadband Acoustic Cloak for Ultrasound Waves”. In: *Physical Review Letters* 106.2 (Jan. 10, 2011), p. 024301.
- [66] L. Quan, X. Liu, and X. Gong. “Quasi-phase-matched backward second-harmonic generation by complementary media in nonlinear metamaterials”. In: *The Journal of the Acoustical Society of America* 132.4 (Oct. 1, 2012), pp. 2852–2856.
- [67] C. C. Claeys, K. Vergote, P. Sas, and W. Desmet. “On the potential of tuned resonators to obtain low-frequency vibrational stop bands in periodic panels”. In: *Journal of Sound and Vibration* 332.6 (Mar. 18, 2013), pp. 1418–1436.
- [68] C. C. Claeys, P. Sas, and W. Desmet. “On the acoustic radiation efficiency of local resonance based stop band materials”. In: *Journal of Sound and Vibration* 333.14 (July 7, 2014), pp. 3203–3213.

- [69] J.-P. Groby, C. Lagarrigue, B. Brouard, O. Dazel, V. Tournat, and B. Nennig. “Enhancing the absorption properties of acoustic porous plates by periodically embedding Helmholtz resonators”. In: *The Journal of the Acoustical Society of America* 137.1 (Jan. 1, 2015), pp. 273–280.
- [70] J. Li, C. Shen, A. Díaz-Rubio, S. A. Tretyakov, and S. A. Cummer. “Systematic design and experimental demonstration of bianisotropic metasurfaces for scattering-free manipulation of acoustic wavefronts”. In: *Nature Communications* 9.1 (Apr. 9, 2018), p. 1342.
- [71] L. Quan, Y. Ra’di, D. L. Sounas, and A. Alù. “Maximum Willis Coupling in Acoustic Scatterers”. In: *Physical Review Letters* 120.25 (June 20, 2018).
- [72] Y. Ra’di, D. L. Sounas, and A. Alù. “Metagratings: Beyond the Limits of Graded Metasurfaces for Wave Front Control”. In: *Physical Review Letters* 119.6 (Aug. 10, 2017), p. 067404.
- [73] J. R. Willis. “Variational principles for dynamic problems for inhomogeneous elastic media”. In: *Wave Motion* 3.1 (Jan. 1, 1981), pp. 1–11.
- [74] J. R. Willis. “The nonlocal influence of density variations in a composite”. In: *International Journal of Solids and Structures*. Topics in Continuum Mechanics 21.7 (Jan. 1, 1985), pp. 805–817.
- [75] J. R. Willis. “Effective constitutive relations for waves in composites and metamaterials”. In: *Proceedings of the Royal Society of London A: Mathematical, Physical and Engineering Sciences* 467.2131 (July 8, 2011), pp. 1865–1879.
- [76] D. K. Cheng and J.-A. Kong. “Covariant descriptions of bianisotropic media”. In: *Proceedings of the IEEE* 56.3 (Mar. 1968), pp. 248–251.
- [77] J. A. Kong. “Theorems of bianisotropic media”. In: *Proceedings of the IEEE* 60.9 (Sept. 1972), pp. 1036–1046.
- [78] A. Serdyukov, I. Semchenko, S. A. Tretyakov, and A. Sihvola. *Electromagnetics of Bi-Anisotropic Materials: Theory and Applications*. Amsterdam: Gordon and Breach Science Publishers, 2001.
- [79] V. S. Asadchy, A. Díaz-Rubio, and S. A. Tretyakov. “Bianisotropic Metasurfaces: Physics and Applications”. In: *Nanophotonics* 7.6 (2018), pp. 1069–1094.
- [80] Y. Li, B. Liang, X. Tao, X.-f. Zhu, X.-y. Zou, and J.-c. Cheng. “Acoustic Focusing by Coiling up Space”. In: *Applied Physics Letters* 101.23 (Dec. 2012), p. 233508.
- [81] G. Lu, E. Ding, Y. Wang, X. Peng, J. Cui, X. Liu, and X. Liu. “Realization of acoustic wave directivity at low frequencies with a subwavelength Mie resonant structure”. In: *Applied Physics Letters* 110.12 (Mar. 20, 2017), p. 123507.
- [82] K. Attenborough. “Acoustical characteristics of rigid fibrous absorbents and granular materials”. In: *The Journal of the Acoustical Society of America* 73.3 (Mar. 1, 1983), pp. 785–799.

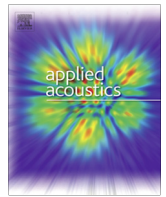
- [83] M. R. Stinson. "The propagation of plane sound waves in narrow and wide circular tubes, and generalization to uniform tubes of arbitrary cross-sectional shape". In: *The Journal of the Acoustical Society of America* 89.2 (Feb. 1, 1991), pp. 550–558.
- [84] C. F. Sieck, A. Alù, and M. R. Haberman. "Origins of Willis coupling and acoustic bianisotropy in acoustic metamaterials through source-driven homogenization". In: *Physical Review B* 96.10 (Sept. 11, 2017), p. 104303.
- [85] S. Koo, C. Cho, J.-h. Jeong, and N. Park. "Acoustic omni meta-atom for decoupled access to all octants of a wave parameter space". In: *Nature Communications* 7 (Sept. 30, 2016), p. 13012.
- [86] M. B. Muhlestein, C. F. Sieck, P. S. Wilson, and M. R. Haberman. "Experimental evidence of Willis coupling in a one-dimensional effective material element". In: *Nature Communications* 8 (June 13, 2017), p. 15625.
- [87] L. Beranek. *Concert Halls and Opera Houses: Music, Acoustics, and Architecture*. Google-Books-ID: N6Zxl6Zqmv0C. Springer Science & Business Media, Nov. 3, 2003. 700 pp.
- [88] *Bühnen Köln Sanierung; Zusätzliche Technische Vertragsbedingungen (ZTV) Teil 3 - Akustische Anforderungen [Renovation of Bühnen Köln; Additional Technical Terms Part 3 - Acoustic Requirements]*. 2013.
- [89] *Product Data: Hand-held Analyzer Types 2250 and 2270*. Bruel & Kjaer. 2016.
- [90] *User Manual: Hand-held Analyzer Types 2250 and 2270*. Bruel & Kjaer. Feb. 2017.
- [91] *ISO 3382-1:2009-06 Acoustics - Measurement of room acoustic parameters - Part 1: Performance spaces*. International Organization for Standardization, 2009.
- [92] J. P. Newton and A. W. James. "Audience noise - How low can you get?" In: *Proc. Inst. Acoust.* 14 (1992), pp. 65–72.
- [93] H. G. Sung. "Gaussian mixture regression and classification". PhD thesis. Rice University, Houston, Texas, 2004.
- [94] H. Akaike. "Information Theory and an Extension of the Maximum Likelihood Principle". In: *Selected Papers of Hirotugu Akaike*. Ed. by E. Parzen, K. Tanabe, and G. Kitagawa. New York, NY: Springer New York, 1998, pp. 199–213.
- [95] G. Schwarz. "Estimating the Dimension of a Model". In: *The Annals of Statistics* 6.2 (1978), pp. 461–464.
- [96] *ISO 20906:2009: Acoustics - Unattended monitoring of aircraft sound in the vicinity of airports*. ISO International Organization for Standardization, 2009.
- [97] A. Schick. *Schallbewertung: Grundlagen der Lärmforschung [Sound Assessment: Fundamentals of Noise Research]*. Springer Berlin Heidelberg, 2013.
- [98] A. Garcia and L. Faus. "Statistical Analysis of Urban Noise Levels". In: *Journal de Physique Colloques* 51.C2 (1990), pp. 281–284.

- [99] A. García and L. Faus. “Statistical analysis of noise levels in urban areas”. In: *Applied Acoustics* 34.4 (1991), pp. 227–247.
- [100] O. S. Olayinka and S. A. Abdullahi. “A Statistical Analysis of the Day-time and Night-time Noise Levels in Ilorin Metropolis, Nigeria”. In: *Trends in Applied Sciences Research* 3 (2008), pp. 253–266.
- [101] H. Ryu, I. K. Park, B. S. Chun, and S. I. Chang. “Spatial statistical analysis of the effects of urban form indicators on road-traffic noise exposure of a city in South Korea”. In: *Applied Acoustics* 115 (2017), pp. 93–100.
- [102] S. H. Park, P. J. Lee, and B. K. Lee. “Levels and sources of neighbour noise in heavyweight residential buildings in Korea”. In: *Applied Acoustics* 120 (2017), pp. 148–157.
- [103] *IEC 60034-1:2010 Rotating electrical machines - Part 1: Rating and performance*. International Electrotechnical Commission, 2010.
- [104] L. E. Kinsler. *Fundamentals of acoustics*. Google-Books-ID: 76IRAQAIAAJ. Wiley, 2000. 568 pp.
- [105] K. T. Chen, Y. H. Chen, K. Y. Lin, and C. C. Weng. “The improvement on the transmission loss of a duct by adding Helmholtz resonators”. In: *Applied Acoustics* 54.1 (May 1, 1998), pp. 71–82.
- [106] *Cellofoam 471 data sheet*.
- [107] *ANSYS Multiphysics, Release 19.2, Help System, ANSYS Inc.*
- [108] S. Marburg and S. Schneider. “Influence of Element Types on Numeric Error for Acoustic Boundary Elements”. In: *Journal of Computational Acoustics* 11.3 (Sept. 1, 2003), pp. 363–386.
- [109] S. Marburg. “The Burton and Miller Method: Unlocking Another Mystery of Its Coupling Parameter”. In: *Journal of Computational Acoustics* 24.1 (June 3, 2015), p. 1550016.
- [110] S. Marburg. *Boundary Element Method for Time-Harmonic Acoustic Problems*. Springer, Cham, 2018.
- [111] G. H. Koopmann and J. B. Fahnlne. *Designing Quiet Structures: A Sound Power Minimization Approach*. Google-Books-ID: 9EFgGTi2r5cC. Elsevier, Oct. 13, 1997. 261 pp.
- [112] S. Marburg and B. Nolte. *Computational Acoustics of Noise Propagation in Fluids - Finite and Boundary Element Methods*. Berlin Heidelberg: Springer-Verlag, 2008.
- [113] *DIN 56950-1:2012-05, Entertainment technology - Machinery installations - Part 1: Safety requirements and inspections*. 2012.
- [114] D. C. Wilcox. “Reassessment of the scale-determining equation for advanced turbulence models”. In: *AIAA Journal* 26.11 (1988), pp. 1299–1310.

- [115] F. R. Menter. “Two-equation eddy-viscosity turbulence models for engineering applications”. In: *AIAA Journal* 32.8 (1994), pp. 1598–1605.
- [116] R. Müller. “Schwingungs- und Geräuschanregung bei Stirnradgetrieben”. PhD thesis. Fakultät für Maschinenwesen, TU München, DE, 1991.
- [117] J. Zhou and S. Wenlei. “Vibration and Noise Radiation Characteristics of Gear Transmission System”. In: *Journal of Low Frequency Noise, Vibration and Active Control* 33.4 (Dec. 1, 2014), pp. 485–502.
- [118] V. Adams and A. Askenazi. *Building Better Products with Finite Element Analysis*. OnWord Press, 1999.
- [119] J. B. Fahline and G. H. Koopmann. “A lumped parameter model for the acoustic power output from a vibrating structure”. In: *The Journal of the Acoustical Society of America* 100.6 (Dec. 1, 1996), pp. 3539–3547.
- [120] D. Fritze, S. Marburg, and H.-J. Hardtke. “Estimation of Radiated Sound Power: A Case Study on Common Approximation Methods”. In: *Acta Acustica united with Acustica* 95.5 (Sept. 1, 2009), pp. 833–842.
- [121] M. Klaerner, M. Wuehrl, L. Kroll, and S. Marburg. “Accuracy of vibro-acoustic computations using non-equidistant frequency spacing”. In: *Applied Acoustics* 145 (Feb. 1, 2019), pp. 60–68.
- [122] *COMSOL Multiphysics, v. 5.4, COMSOL AB*.
- [123] T. W. Wu. *Boundary element acoustics: fundamentals and computer codes*. Google-Books-ID: nqJRAAAAMAAJ. WIT, 2000. 270 pp.
- [124] J. V. Sánchez-Pérez, D. Caballero, R. Martínez-Sala, C. Rubio, J. Sánchez-Dehesa, F. Meseguer, J. Linares, and F. Gálvez. “Sound Attenuation by a Two-Dimensional Array of Rigid Cylinders”. In: *Physical Review Letters* 80.24 (June 15, 1998), pp. 5325–5328.
- [125] F. Langfeldt, W. Gleine, and O. von Estorff. “Analytical model for low-frequency transmission loss calculation of membranes loaded with arbitrarily shaped masses”. In: *Journal of Sound and Vibration* 349 (Aug. 4, 2015), pp. 315–329.
- [126] L. Moheit and S. Marburg. “Infinite Elements and Their Influence on Normal and Radiation Modes in Exterior Acoustics”. In: *Journal of Computational Acoustics* 25.4 (Mar. 14, 2017). Publisher: World Scientific Publishing Co., p. 1650020.
- [127] L. Moheit and S. Marburg. “Normal Modes and Modal Reduction in Exterior Acoustics”. In: *Journal of Theoretical and Computational Acoustics* 26.3 (July 11, 2018). Publisher: World Scientific Publishing Co., p. 1850029.
- [128] L. Moheit, S. Anthis, J. Heinz, F. Kronowetter, and S. Marburg. “Analysis of scattering by finite sonic crystals in free field with infinite elements and normal modes”. In: *Journal of Sound and Vibration* (Mar. 6, 2020), p. 115291.

- [129] Y. Jia, Y. Luo, D. Wu, Q. Wei, and X. Liu. “Enhanced Low-Frequency Monopole and Dipole Acoustic Antennas Based on a Subwavelength Bianisotropic Structure”. In: *Advanced Materials Technologies* (2020), p. 1900970.
- [130] Y. Achaoui, A. Diatta, M. Kadic, and S. Guenneau. “Cloaking In-Plane Elastic Waves with Swiss Rolls”. In: *Materials* 13.2 (Jan. 2020). Number: 2 Publisher: Multidisciplinary Digital Publishing Institute, p. 449.
- [131] L. Quan, D. L. Sounas, and A. Alù. “Nonreciprocal Willis Coupling in Zero-Index Moving Media”. In: *Physical Review Letters* 123.6 (Aug. 9, 2019). Publisher: American Physical Society, p. 064301.
- [132] R. Pernas-Salomón and G. Shmuel. “Symmetry breaking creates electro-momentum coupling in piezoelectric metamaterials”. In: *Journal of the Mechanics and Physics of Solids* 134 (Jan. 1, 2020), p. 103770.
- [133] J. Park, D. Lee, and J. Rho. “Recent Advances in Non-Traditional Elastic Wave Manipulation by Macroscopic Artificial Structures”. In: *Applied Sciences* 10.2 (Jan. 2020). Number: 2 Publisher: Multidisciplinary Digital Publishing Institute, p. 547.

Appended Papers



Sound pressure level limits for stage machinery noise in operas and theaters



Anton Melnikov^{a,b,*}, Ingo Witew^c, Marcus Maeder^a, Monika Gatt^a, Michael Scheffler^d, Steffen Marburg^a

^aVibroacoustics of Vehicles and Machines, Technical University of Munich, Garching 85748, Germany

^bSBS Bühnentechnik GmbH, Dresden, Saxony 01259, Germany

^cInstitute of Technical Acoustics, RWTH Aachen University, Aachen 52074, Germany

^dApplied Mechanics Group, University of Applied Sciences, Zwickau 08056, Germany

ARTICLE INFO

Article history:

Received 8 January 2019

Received in revised form 1 June 2019

Accepted 20 June 2019

Available online 2 July 2019

ABSTRACT

The absence of disturbing background noise is a fundamental minimum requirement for performances in opera houses and theaters. Although the acoustic design of such venues has reached some maturity and specifications for maximum allowable background levels can be found in almost every other textbook on auditorium design, it can be observed that tender documents show a noteworthy variance in published requirements. Oftentimes, the levels that need to be achieved fall significantly below commonly quoted reference values. In order to keep the specifications at a reasonable level and to reduce costs for the (public) developer and builder it seems reasonable to review long-serving guidelines and determine if they suffice for today's performance practice.

This work presents limits for the stage machinery based on measurements conducted during live performances at four well-known performance art spaces in Germany. To ensure inaudibility of the stage machinery, the limits refer to the quietest performance moments without stage machinery noise, music, speech, or other noise events. Based on these limits the stage machinery developer receives a guideline, which helps to design high-quality machinery in terms of noise. Furthermore, these limits help to refine the noise requirements for stage machinery in tender documents.

© 2019 The Authors. Published by Elsevier Ltd. This is an open access article under the CC BY license (<http://creativecommons.org/licenses/by/4.0/>).

1. Introduction

Administrations of opera houses and theaters strive to impress their audiences with great performances using lights, sounds, drama, and much more. To be able to enjoy the performance, the attendees should be exposed as little as possible to disturbances like blocked sight lines, uncomfortable chairs, blinding light, or noise. Depending on the origin of the disturbance, finding a solution to fix the problem can be challenging at times. Especially the noise produced by the machines or spotlights can be very annoying and difficult to resolve.

Occasionally, the only possible solutions are replacing the disturbing equipment with quieter products or avoiding the scenic use of noisy hardware in the first place. This may not always be possible, especially for bigger machines like turntable stages, stage wagons and stage elevators [1,2], especially if those are essential for providing important scenic movements. For this reason, noise should be considered in the design process of stage equipment.

Such a development process presupposes appropriate noise requirements.

In the following, different existing requirements and standards for noise in auditoria are discussed, especially concerning applicability to stage machinery. Also the available sources to machinery noise, particularly stage elevators, are analyzed. This is done to answer the question:

- Which noise limits should be applied to stage machinery?

1.1. Noise in auditoria

The requirements for technical background noise in auditoria are commonly mapped by the Noise Criterion (NC) [3,4], Preferred Noise Criterion (PNC) [5], Noise Rating (NR) [6], Balanced Noise Criterion (NCB) [7,8], or Room Criterion (RC) curves [9]. For opera houses and drama theaters similar limits of NC20 have been recommended by Beranek [3], Barron [10], or Gade/Rossing (ed.) [11], but sometimes NC15 or PNC15 is used separately for continuous building services noise. This corresponds to a sound level of about 20 dB(A). These limits are primarily aimed at steady-state technical noise, but not at non-steady-state stage machinery noise.

* Corresponding author at: Vibroacoustics of Vehicles and Machines, Technical University of Munich, Garching 85748, Germany.

E-mail address: anton.melnikov@tum.de (A. Melnikov).

Stage machinery usually provides very short operating durations and interacts with the audience noise. Therefore, the audience noise has to be considered for stage machinery noise requirements.

One of the first mentions of the audience noise levels in live concert halls reveals a minimum level of 33 dB(A) [12]. Later measurements e.g. in Sýnderborg Alslion hall similarly indicate 32 dB(A) (L_{90} of audience noise distribution, sum over octaves [13]), however Malmý concert hall, Odense Carl Nielsen hall, and Copenhagen Queen's hall show lower levels [13,14]. Moreover, this study points out the correlation between audience noise and background noise [13]. Though concert halls are regularly equipped with stage machinery, in the vast majority its scenic use during the performance is neither intended nor possible. This is different in operas and theaters, where the machinery movement can be part of the performance.

Unfortunately, data of audience noise measured in opera houses or theaters is sparse. One of the few investigations besides that in Copenhagen Opera house [13,14] was conducted in the Gothenburg Town Theater [15]. During a series of theatrical live performances with 600 visitors on average a level of 35.5 dB(A) was measured. To provide better insights, it makes sense to collect additional measurement data with broader spectral range and more performance art spaces included.

1.2. Stage machinery noise

In case of stage machinery, noise optimization is motivated by levels that are imposed by tender documents or literature. The limits required by a wide selection of tenders between 2005 and 2014 shown in Fig. 1 give an overview of the current market situation. The data contains requirements (triangles and circles) between 25 dB(A) and 50 dB(A), measured in the first row of auditoria. The linear regression over time (dashed gray line) shows a decreasing trend. Such a trend demonstrates an increased demand for quiet stage machinery. It seems therefore reasonable to expect strict noise limits such as < 35 dB(A) rather than lenient limits (see Fig. 1, points 5 and 13) in future tenders. The presented data shows a large range of levels and cannot be used to derive a general limit. This constrains the limit derivation to the available literature.

The requirements valid specially for stage machinery noise in theaters and operas are not represented in the international literature. Nevertheless, to get an overview national literature can be used. One of the few available publications proposes the following limits: drama theater, 35 dB(A) for lower machinery and 45 dB(A) for upper machinery; musical theater, 40 dB(A) for lower machinery and 45 dB(A) for upper machinery [17]. Comparing the outcomes of this study with the tender documents in Fig. 1 shows that 34% of the tenders underestimate the proposed limits, only 9% match it exactly and a majority of 57% overestimate it. Even though 9% of the shown tender values match the proposed level in the literature exactly, there is no general consensus between tender and literature.

The limits from tenders and literature feature an additional aspect requiring clarification, namely its technical feasibility. In an experiment Schirmer and Ulrich [18,19] compared the levels generated by 8 different power train systems of stage elevators moving at 0.3 m/s, measured in the first row of auditoria. Their recorded levels range from 35 dB(A) for an electric motor with ropes to 71 dB(A) for an electric motor with screw jack. Values in between cover 37 dB(A) and 40 dB(A) for two systems with hydraulic motor and ropes, 40 dB(A) for two systems with hydraulic cylinder and ropes, and 40 dB(A) and 47 dB(A) for two systems with electric motor and gear racks. In light of the understage machinery limits proposed by Tennhardt [17], there is only one power train that barely accomplishes the published drama theater limit of 35 dB(A). Half of the tested systems meet the suggested

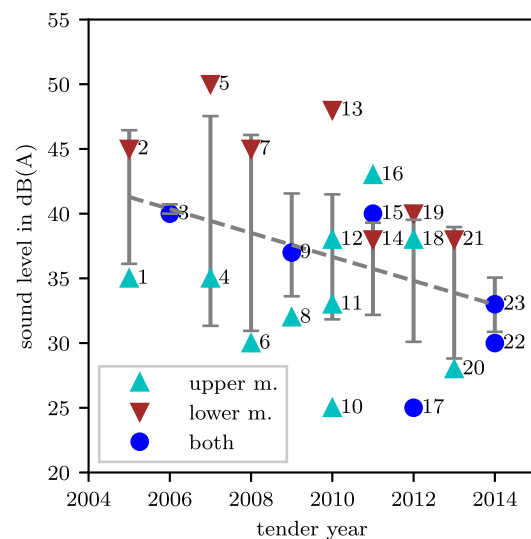


Fig. 1. Sound level requirements at first auditorium row from tender documents between 2005 and 2014 [16], separated by limits for upper machinery (light-blue triangles), lower machinery (flipped brown triangles) and one limit for both machinery types (blue circles). Gray dashed regression line shows a decreasing trend. Error bars illustrate the standard deviation with respect to the regression line. 2005: Großes Haus Gera (1) upper and (2) lower machinery (unspecified); 2006: (3) National Opera and Ballet of Belarus (unspecified); 2007: House of Musical Arts Muscat (4) upper and (5) lower machinery (unspecified); 2008: Mariinsky Theater St. Petersburg (6) upper and (7) lower machinery (unspecified); 2009: (8) Das Meininger Theater upper machinery (L_{Aeq}), (9) Kammerspiele Paderborn (unspecified); 2010: (10) Classical Theatre of Opera and Ballet Astana upper machinery (L_{Aeq}), (11) Schauspiel Frankfurt upper machinery (L_{Aeq}), Musiktheater Linz (12) upper and (13) lower machinery (unspecified); 2011: (14) Berlin State Opera lower machinery (unspecified); (15) Yanka Kupala National Academic Theatre Minsk (unspecified); (16) Berlin State Opera upper machinery (unspecified); 2012: (17) Grande Auditório Gulbekian (unspecified); Artpalace 'Neftjanik' Surgut (18) upper and (19) lower machinery (unspecified); 2013: Saarländisches Staatstheater (20) upper and (21) lower machinery (unspecified); 2014: (22) Deutsche Oper Berlin (L_{Aeq}), (23) Bühnen der Stadt Köln (L_{Aeq}).

musical theater limit of 40 dB(A). It should be mentioned that the informative value of measurements from 2002 may have changed due to improved gear and electric motor technology. At present, appropriate boundary conditions inside the building and sufficient design effort can lead to extraordinarily quiet stage elevator installations, such as in Operaen Copenhagen with 27 dB(A)–30 dB(A) during one operation cycle [20]. However, there is no further evidence known in literature for the technical feasibility of stage elevators generating noise levels under 30 dB(A) during a whole operation cycle.

Finally, the topic of stage machinery noise needs to be discussed from an economic and artistic point of view. It must be clear to all involved parties that a continuous reduction in the permissible noise levels (in tender documents) leads to a (presumably exponential) increase in costs for the customer. It is certainly difficult or impossible to determine the price of artistic freedom, but nevertheless it is desirable to have a perspective that can be quantified. In terms of machinery noise limits, this can be achieved by collecting data that shows how often a given SPL occurs during a performance without machinery noise. Setting the limits for machinery noise at an appropriately low SPL will ensure that the any machinery noise will be masked by naturally occurring background noise.

All this stresses the need for more detailed data, which can be obtained only by conducting new measurements. Measurements of the noise during a performance can reveal an answer to the refined research objective:

- Which spectral noise limits should be applied to stage machinery in operas and theaters?

This study reports on acoustic measurements during live performances in 4 venues (opera houses and theater). The collected data extends previous knowledge of the spectral composition and the likelihood of occurrence of a given Sound Pressure Level (SPL) during opera, ballet and theatrical performances. Different evaluation methods are discussed which allow a differentiated approach to limits for background noise that goes beyond single-value parameters currently available in the literature. The determined background noise limits for stage machinery are independent of the particular stage machinery at the venues that were part of this study, since the stage machinery was inactive during the periods that were investigated. The discussion addresses aspects that are unique to noise from stage machinery that is transient in nature and consists of short term events.

2. Method

2.1. Measurements

With the goal to collect performance noise data including spectral content acoustical measurements were conducted under realistic conditions and under normal operation. The noise was measured directly during live performances from the receiver perspective. The measurement position was in the middle of the first row of audience seating [21]. This is a typical measurement position used for quality acceptance tests during the handover phase of newly built or renovated performance art spaces. This is in line with current tender documents [21] and previous investigations [17–20] discussing stage machinery noise. Compared to other possible listener positions this is the most critical one due to the shortest distance to the noise source. The placement of the microphone was 120 cm above the floor according to ISO 3382-1 [22].

To cover the complete audible frequency range, the SPL was measured over the frequency range from 12.5 Hz to 20 kHz. To capture low SPL accurately a microphone with an intrinsic noise of less than 20 dB was chosen. To be able to catch the short breaks during the music or actor speech, the data was recorded in 100 ms intervals.

2.1.1. Equipment

The handheld analyzer type 2270 from Brüel&Kjær was used for measurements. The specifications for the 1/2-inch free-field microphone type 4189 with ZC-0032 preamplifier are given in the Brüel&Kjær product manuals [23,24]. The microphone was calibrated with the Brüel&Kjær pistonphone type 4228 before and after every measurement.

2.1.2. Measurement venues

The measurements were conducted during 12 performances at 4 different venues. In the case of day-to-day business of the venues it is challenging to get permission to measure live opera performances at the required measurement position. This leads to significant limitations concerning sample size. In this study, the sample size is comparable to well-known studies on audience noise [15,13,14,25].

The venues were selected to obtain a variety in program at a quality standard that is 'setting the tone' on an international scale [26] and are shown in Table 1. Since opera is the performance type, where it is more common to expect occasional stage machinery operation, the choice of venues and pieces is focused on it. Additionally, a drama theater was included, which is a middle-sized typical theater house that reflects the wide-spread state of technology and artistic performance practice.

In addition to the performance measurements, stationary background noise measurements were conducted at the surveyed

Table 1

Places for measurements including the type, the year of last significant renovation or refurbishment, and the number of seats.

Venue	Type	Renovation	Seats
(a) Semperoper Dresden	Opera	1985	1270
(b) Leipzig Opera	Opera	2007	1267
(c) Bayerische Staatsoper	Opera	1963	2101
(d) State Playhouse Dresden	Theater	1990	785

venues. These were done over at least 60 s for each venue during full operation of potential noise sources such as Ventilation and Air Conditioning (HVAC). All included venues fulfill NC20 and PNC20, which is appropriate for opera houses and drama theaters [3,10,11]. The spectrum of the background noise (solid blue line) is illustrated in Fig. 4a for venue (a), Fig. 4d for (b), Fig. 4e for (c), and Fig. 9a for (d). Furthermore, the reverberation times in venues (a), (b), and (d) were determined and are shown in Table 2. During this measurement, the receiver position was in the middle of the first row 120 cm above the floor. The position of the impulse source was on the right side in front of the stage, approx. 160 cm above the floor and approx. 10 m away from the receiver position. For venue (c), Table 2 shows the reverberation times available in the literature [28,27]. The reverberation time characterizes the diffuse field, which has an impact on the measured SPL in a hall. Since the considerations are focused on operas and theaters, it is necessary to consider venues with appropriate reverberation time. Venues (b) with 1.4 s, (c) with 1.7 s, and (d) with 1.3 s at 1 kHz lie in the typical range for operas and theater houses [10]. Venue (a) demonstrates a relatively long reverberation time (2 s at 1 kHz), which is confirmed by the data published in literature [26]. According to Barron [10], such long reverberation time design is a current trend in new European opera houses. According to this fact, the venue choice represents state of the art in terms of background noise and reverberation time.

To cover the typical range of genres, 12 different performances were chosen for the measurement. The pieces selected at Semperoper Dresden were 3 operas and 2 ballets. Different epochs were included in the chosen operas, namely *Doktor Faust* (1925) by F. Busoni, *La clemenza di Tito* (1791) by W. A. Mozart, and *Les Contes d'Hoffmann* (1881) by J. Offenbach. The chosen ballets were both from the same epoch but from different genres. *Manon* (1974) is a classical ballet by K. MacMillan and J. Massenet and *Forgotten Land* (1981) is a modern ballet by G. Balanchine, J. Kilián, and W. Forsythe. At Leipzig Opera an opera and a ballet piece were selected: *Die Frau ohne Schatten* (*The Woman without a Shadow*) (1919) by R. Strauss and a neoclassical ballet *Don Juan* (1998) by T. Malandain. It was possible to measure one piece at Bayerische Staatsoper twice: *Un Ballo in Maschera* (1857) by G. Verdi. This allows assessing the consistency of the findings. The repeated measurements were done under reproducibility conditions [B.2.16] [JCGM 100:2008] with the changed condition of 'time' and 'condition of use' as the two performances were recorded on two

Table 2

Reverberation times measured in venues (a), (b), and (d) (see Table 1) in octaves. Determined in the middle of the first row in the unoccupied condition and with iron curtain closed. Reverberation times of venue (c) were taken from literature [27,28].

Octave Hz	(a) s	(b) s	(c) s	(d) s
250	-	1.74	1.7	1.59
500	2.02	1.50	1.7	1.45
1 k	1.95	1.42	1.7	1.33
2 k	1.85	1.29	1.6	1.27
4 k	1.52	1.06	1.2	1.17
8 k	1.13	0.77	-	0.88

different days with the entire equipment set up and dismantled for the two measurements. The relatively new piece *Alice's Adventures in Wonderland* (2011) by C. Wheeldon, J. Talbot, and N. Wright was selected as the ballet performance in that auditorium. The pieces measured in State Playhouse Dresden were *Jeder stirbt für sich allein* (*Alone in Berlin*) by H. Fallada and E. Petschinka and *Amphitryon* by H. von Kleist. Through the wide range of pieces covering different cultural epochs in style, it is ensured that the analysis remains valid for a large range of conditions.

2.2. Data analysis

For data acquisition and export, the Bruel&Kjaer-Software BZ5503 was used. The A-weighted total equivalent level L_{Aeq} and the unweighted L_{eq} in 1/3 octave bands (12.5 Hz–20 kHz) in 100 ms-steps was taken during the entire performance. Here, L_{eq} is the true equivalent level without time weighting applied. To ensure that only the actual performance time is subject of the analysis, the data was cleaned from applause and intermissions afterwards.

The audience behavior during opera, ballet and theater performance is different from each other (e.g. aria applause in opera). Furthermore, the performance sound pattern is dependent on the performance type, for example short intermissions for entering and leaving dancers typically present in a ballet performance. These differences have a significant influence on the generated noise. To reflect this aspect the data is processed separately for opera, ballet, and drama.

In order to illuminate the collected data from different angles, different data analysis methods are discussed: Minimum 1s-Averaged Level (min1s) level, Gaussian Mixture Model (GMM), and N% exceedance level.

2.2.1. Minimum 1 s-Averaged Level (min1s)

The most straightforward way to look for the background noise level over the measurement duration is to use the quietest period of time as was done by Newton & James [25]. An adequate time interval is 1 s, which is based on the subjective duration evaluation of a 1 kHz tone of 60 dB SPL as proposed by Fastl/Zwicker [29, pp. 265–269]. Whereas the data is in 100 ms-steps, the evaluation can make use of this time discretization by moving time average with a rectangular window function of length 1 s in the form

$$L_{min} = \min \left\{ 10 \lg \left(\frac{1}{n} \sum_{i=1}^n 10^{0.1L_{j+i}} \right) \right\}, \quad (1)$$

with $\min\{\}$ as minimum operator, L_{j+i} as band filtered or broad band level at sample $j + i$, and $n = 10$ as number of samples in the window. As a result, this procedure yields the min1s level with a better time discretization in 100 ms-steps. A data cut-out is shown in Fig. 2: the black line is the measured total level and the gray region indicates the averaging time.

The charm of a relatively simple parameter is counterbalanced by the potential to overestimate noise requirements. Levels identified using the min1s algorithm occur only once during a performance and are by definition relatively rare. Thus, this metric allows quantifying the moments of dramatic silence, where the audience may collectively hold their breath. Adopting min1s levels as noise requirements for stage machinery may be understood as aiming for the highest possible target, namely ensuring that noise from stage machinery will not be heard during a performance at all. From an engineering point of view additional information that helps interpreting sound levels as they occur during a performance would be desirable. In particular, a SPL likelihood of occurrence during a performance would enable better assessment of the reasonableness of sound levels for limit derivation.

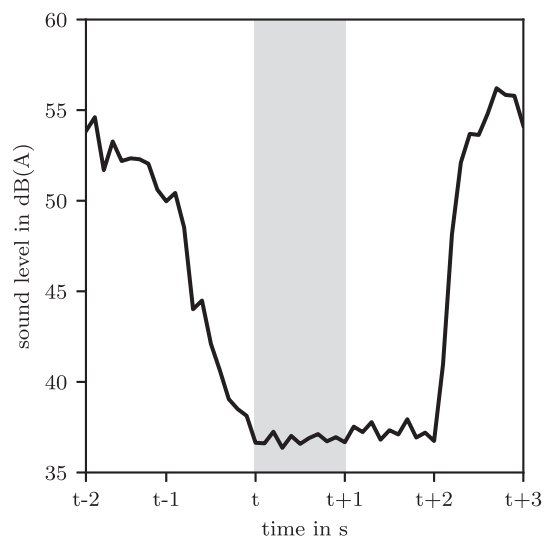


Fig. 2. A-weighted total level of a short break during the performance. Solid black line is the level and the gray region indicates the averaging time for obtaining the min1s level.

2.2.2. Gaussian Mixture Model (GMM)

To consider the occurrence probability and to allow more in-depth level analysis a statistical perspective can be useful. GMM [30] is an established method in noise studies. The effectiveness of it was demonstrated in several audience and background noise investigations [13,31]. GMM splits a global Probability Density Function (PDF) into multiple normal distributions. This decomposition can be applied on the SPL distribution during the performance (Fig. 3, gray line), whether in 1/3 octaves or as total level. Afterwards every single normal distribution can be considered separately. This allows to remove unwanted noise sources from the PDF or to focus on noise sources of interest.

The GMM represents a linear combination of normal distributions

$$p(x) = \sum_{k=1}^N w_k \varphi_k(x) \quad (2)$$

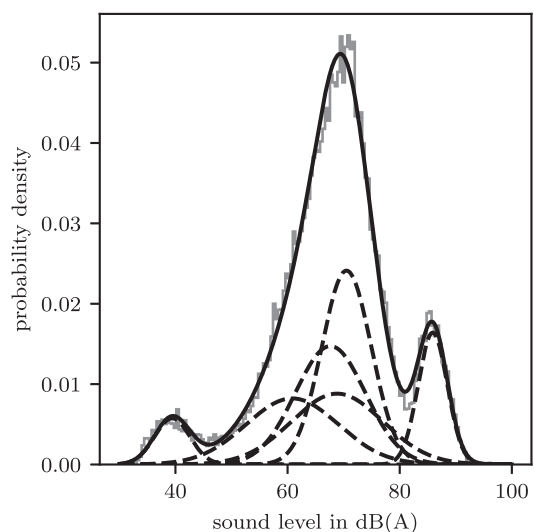


Fig. 3. GMM (solid black line) applied to the measured PDF (solid gray line) of total level in the ballet piece Don Juan. BIC suggests 6 normal distributions (dotted lines) as suitable.

with number of normal distributions N in the form

$$\varphi_k(x) = \frac{1}{\sqrt{2\pi\sigma_k^2}} e^{-\frac{1}{2}\left(\frac{x-\mu_k}{\sigma_k}\right)^2}. \quad (3)$$

Considering the separated normal distributions, the GMM noise limit is defined by the mean value of the minimum distribution (Fig. 3 left gaussian). This presumes that the background noise is normally distributed and the contribution is sufficient to be detected with GMM. The example histogram in Fig. 3 clearly reveals three peaks. However, a suitable approximation requires a higher distribution number [13,31]. To determine the optimal number Bayesian Information Criterion (BIC) [32,33] is used. Applied on the example in Fig. 3, BIC suggests 6 normal distributions. It is necessary to use an appropriate number of normal distributions to obtain the minimum distribution and subsequently the limit value correctly. In the cases where the smallest cluster of levels is not fitted well enough, there is a danger to underestimate the noise requirements [34].

2.2.3. $N\%$ exceedance level (L_N)

As an alternative to GMM a probabilistic method called $N\%$ exceedance level (L_N) [35,36] can be applied. It directly delivers information about how often a distinct level is exceeded over the measurement time. This type of level-quantile is usually used in traffic noise investigations [37–39] and can also be the basis for more sophisticated models [40,41] or linked with GMM [13].

Based on the intended probability the L_N noise limit is defined by the exceedance level value. It combines the robustness of the min1s level combined with a probabilistic approach. The benefit of the L_N method is the known quantile N , which represents how often the L_N level is exceeded. Due to the very definition of level-quantile a probability of having fallen below a distinct level limit is automatically obtained. Despite this advantage, for higher occurrence probabilities there is an increasing risk of including performance sounds in the results. This risk can be minimized by adequate choice of the percentile. Accordingly, the percentiles 95 and 99 well represent the important probability range and emerge reasonable for limit derivation.

3. Results

3.1. Opera

The results for individual opera pieces can be found in Fig. 4. Merged to one data set all opera pieces result in 12.3 h of evaluated opera performance. Data analysis in 1/3 octave bands and in octave bands is shown in Fig. 5. The colored background reveals the cumulative density of the measured data. The black lines denote the L_N levels, the red line illustrates the min1s level, and the cyan line refers to the mean values from GMM. The background level is represented by the blue line. For individual results the background level is shown for the venue where the piece was measured. For merged results only the maximum value of venues considered in that unique case is illustrated. The quantitative summary of the results is listed in Table 3.

3.2. Ballet

The ballet data (5.8 h) is shown in the same way as the data from operas. For individual pieces see Fig. 7 and for the merged ballet data see Fig. 6 and Table 4.

3.3. Drama

Figs. 8 and 9 and Table 5 show the same results for theatrical performances based on 4.1 h of recorded material.

4. Discussion

4.1. Reproducibility of level metrics

The suitability of the different level metrics can be evaluated based on the reproducibility and on the reasonableness of the results. The reproducibility of the results can be assessed by comparing the two takes of *Un Ballo in Maschera* in Fig. 10. The best reproducibility is achieved by the exceedance levels (see Fig. 10 solid green and magenta lines), where only a small difference with a maximum of 1.4 dB at 31.5 Hz is present. $L_{\min 1s}$ shows the highest difference of 3 dB at 16 Hz (see Fig. 10 red solid line), which is outside the frequency range important for room acoustics. Above 160 Hz this method shows deviations of less than 1 dB and, hence, may be recognized as a reasonable method to determine SPL limits. The poorest results are generated by the GMM method (see Fig. 10 cyan solid line) with relatively large differences of up to 10 dB at 1 kHz and of 5 dB at 400 Hz.

One possible explanation for this is that in some cases the stationary background noise is not identified by the GMM method as a separate distribution. This situation can arise when the (cumulative) probability of stationary background noise to occur is relatively low and in the same order of magnitude as the fitting residual of the GMM method. With the background noise usually being the distribution with the lowest levels the difference between detecting and not detecting this distribution can be quite significant level-wise. Such problems were not encountered in similar studies [13,31] that also used GMM strategies. This can be traced back to differences in determining the fitting residual. While Jeong et al. [13] used a predetermined number of distributions combined with weighting factors to increase the impact of low level contributions the present study determines the number of synthesizing distributions a posteriori based on the BIC.

4.2. Types of performances

All analyzed performance types have in common a global decrease in levels towards higher frequencies. This can be observed in Figs. 5, 6, and 8 for opera, ballet, and drama performances alike. Differences become evident when it is distinguished between performance types and parameter metrics. In drama performances the different level metrics yield very similar results. This is rather evident in Fig. 8b showing an almost strictly monotonic decrease in levels between 16 Hz (≈ 50 dB) and 16 kHz (≈ 17 dB). In contrast, the levels determined during opera or ballet performances are shown in Figs. 5b and 6b. These illustrate a larger spread in levels at mid frequencies for the different metrics. Also, for some parameters the generally decreasing trend is interrupted between 125 Hz and 4 kHz by a local maximum at mid frequencies (e.g. see Fig. 5b, GMM level of 57 dB at 500 Hz for opera performances).

As this increase in level matches the frequency range associated with music (55 Hz–4 kHz [11]), the elevated levels are likely caused by the performance music during the recordings. The exact comparison of the different level metrics in opera and ballet performances shows that the different parameters provide a different resilience against detecting performance sounds. In Figs. 5b and 6b, L_{GMM} and L_{95} yield relatively high levels compared to $L_{\min 1s}$ and L_{99} . The latter two parameters show relatively similar results for ballet performances over the entire frequency range, but also for opera performances over a wide frequency range.

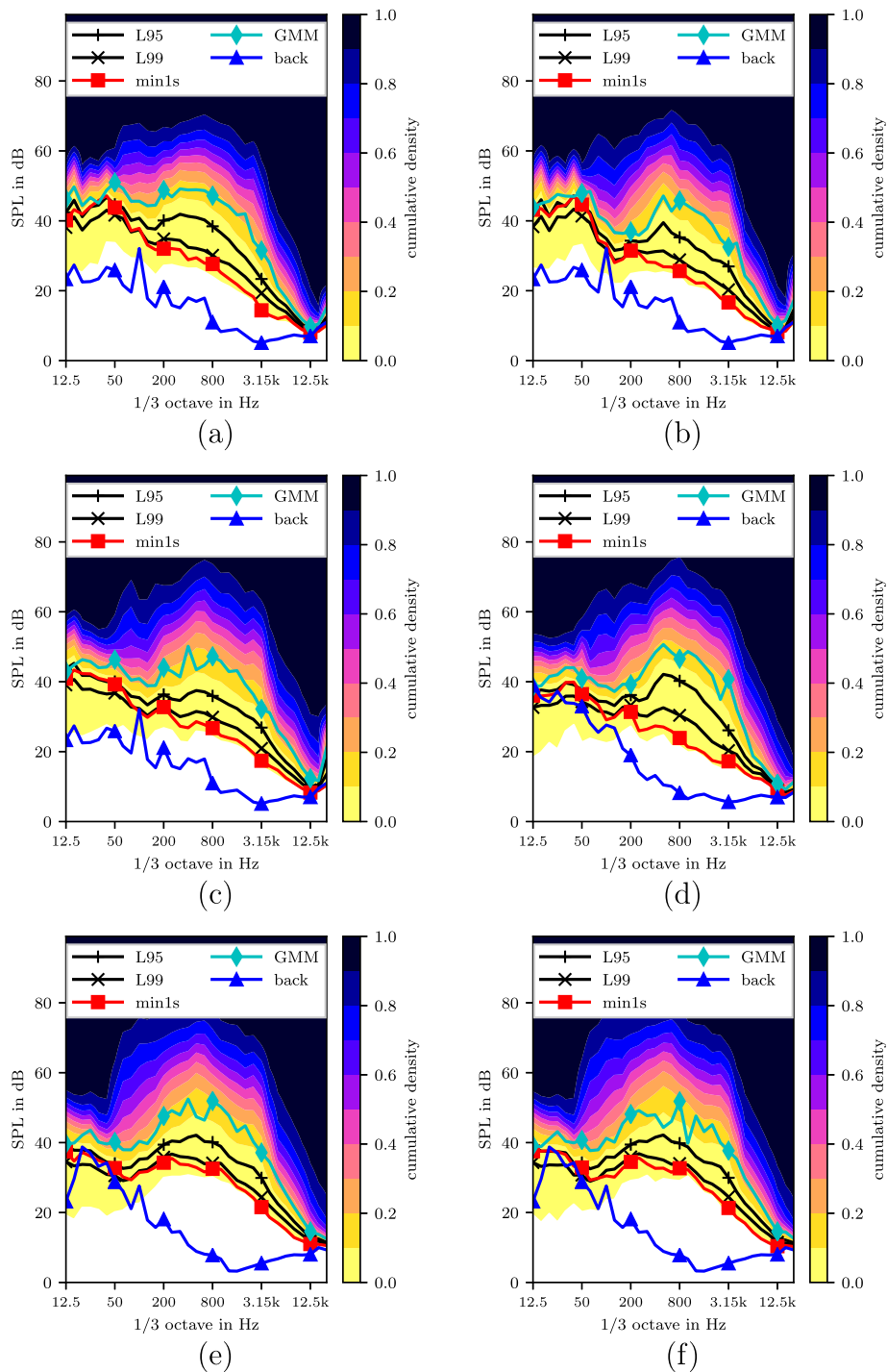


Fig. 4. Opera individual measurements and analysis results. (a) *Dr. Faust*, (b) *Titus*, (c) *Les Contes d'Hoffmann*, (d) *The Woman without a Shadow*, (e) *Un Ballo in Maschera* – take 1, (f) *Un Ballo in Maschera* – take 2.

In the case of opera and ballet results, it is observed that the background noise at frequency bands below 160 Hz is sometimes higher than the min1s and L_{99} results, see Figs. 5 and 6. Since the background level (blue solid line) is the maximum of all considered venues for each performance type, it can slightly exceed the levels obtained by the noise metrics. Also the individual results can demonstrate such a behavior, see for example Fig. 4e or Fig. 7c. This is mainly attributed to higher likelihood of measuring extreme low level due to much longer measurement time during the performance compared to the relatively short background noise measurement.

4.3. Stage machinery imperceptibility probability

The experimentally determined relationship between SPL and the probability of exceedance N does not yet provide a direct foundation to predict the likelihood of hearing stage machinery as it is not operated continuously during the entire performance. In fact, stage machinery is audible during a performance precisely when the two events 'SPL falls below L_N ' and 'stage machinery operates' occur simultaneously. This relationship can be represented mathematically by

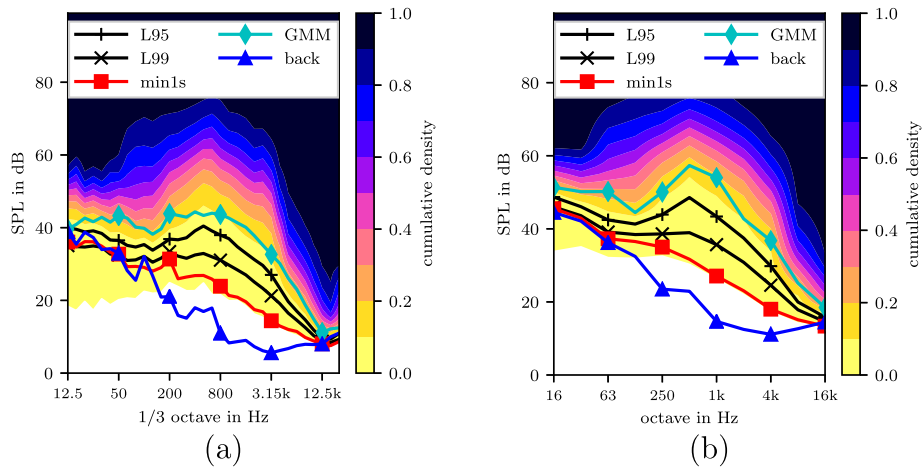


Fig. 5. Opera measurement and analysis results. (a) in 1/3 octave bands, (b) in octave bands.

Table 3
Merged opera results: min1s levels, GMM minimum mean values and L_N levels.

Octave Hz	min1s dB	GMM dB	L_{95} dB	L_{99} dB
16	45.5	51.4	48.7	46.0
31.5	42.9	50.2	46.1	43.6
63	37.3	50.2	42.4	39.1
125	36.5	44.5	41.3	38.4
250	35.0	49.5	43.9	38.6
500	31.7	57.4	48.6	38.9
1 k	27.1	54.0	43.4	35.7
2 k	23.0	42.8	37.5	30.8
4 k	18.0	36.1	29.8	24.6
8 k	15.1	25.2	20.0	17.8
16 k	13.4	18.5	15.8	14.6
Total (A)	34.8	58.1	52.1	42.9

Table 4
Merged ballet results: min1s levels, GMM minimum mean values and L_N levels.

Octave Hz	min1s dB	GMM dB	L_{95} dB	L_{99} dB
16	45.1	51.4	49.6	46.7
31.5	45.3	53.4	48.4	45.8
63	40.0	50.1	45.8	42.7
125	35.5	50.7	41.9	38.2
250	32.9	54.6	47.9	38.4
500	31.2	46.8	48.0	36.6
1 k	28.1	42.5	44.0	32.5
2 k	24.9	40.7	38.3	29.1
4 k	18.6	35.5	28.9	22.9
8 k	14.2	23.4	19.6	16.6
16 k	12.8	21.7	16.1	13.7
Total (A)	33.7	48.5	52.2	40.0

$$P_{imp} = 1 - P_{SM} \cdot (1 - N). \tag{4}$$

The imperceptibility probability P_{imp} during a performance is a function of the percentile of the exceedance level N and the probability of stage machinery operation P_{SM} .

Technically, to prevent overheating, the operation of machinery is limited by the intermittent periodic duty S3 to 40% [42]. A probability of $P_{SM} = 40\%$ may seem to overestimate the actual usage of

stage machinery by far, given wide-spread rules of thumb suggesting a maximum use of five complete up and down cycles during a performance. Based on an average performance duration of 111 min and five 6 m strokes of 0.3 m/s (200 s in total) this leads to an adequate and realistic operation probability of $P_{SM} \approx 3\%$. For the arbitrary choice of having stage machinery with noise characteristics that fall below the levels defined by $N = 99\%$, Eq. (4) yields an imperceptibility probability of $P_{imp} \approx 99.97\%$.

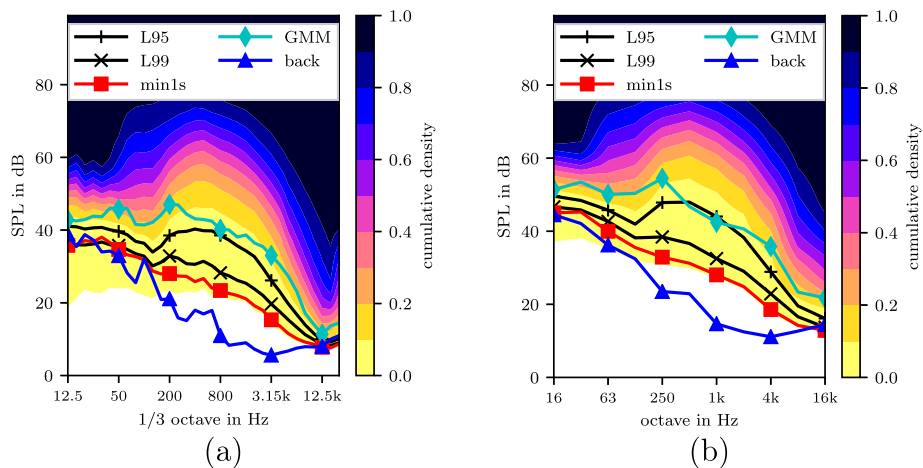


Fig. 6. Ballet measurement and analysis results. (a) in 1/3 octave bands, (b) in octave bands.

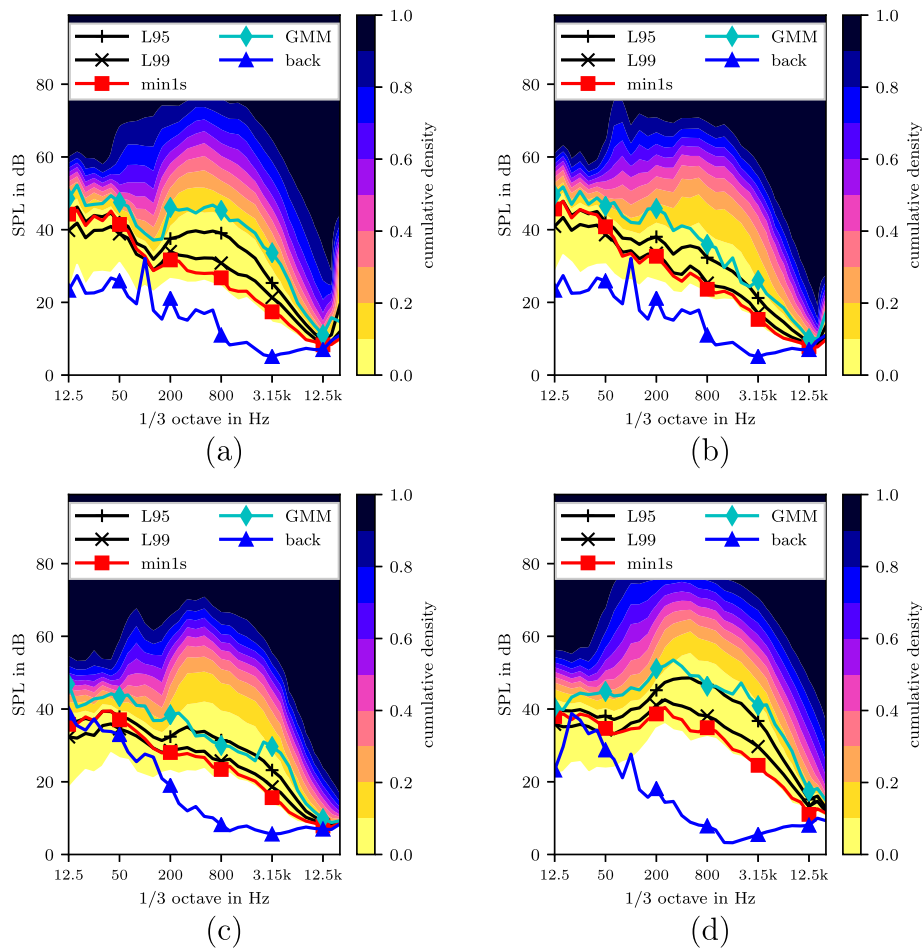


Fig. 7. Ballet individual measurements and analysis results. (a) *Manon*, (b) *Forgotten Land*, (c) *Don Juan*, (d) *Alice's Adventures in Wonderland*.

Obviously this assumes that the events 'SPL falls below L_N ' and 'stage machinery operates' are uncorrelated to each other. In situations where machinery operation is purposely aimed at silent moments the presented concept is not applicable. The risk of L_N being influenced by operating stage machinery cannot be excluded beyond the smallest doubt since there is no data available showing the noise characteristics of the moving stage elevators in the otherwise silent halls. As long as the assumption holds that both events discussed earlier are uncorrelated, it can be maintained that the noise of the stage machinery probably does not affect the exceedance levels. The semantic analysis of the min1s events provides some support for the assumption that the stage machinery was not operated in the quietest moments deliberately.

4.4. Spectral content

Compared to the levels of individual performances or different pieces in Figs. 4, 7, and 9 the merged data of all pieces (see Figs. 5, 6, and 8) of the same genre shows a much more homogeneous trend over frequency which is due to the longer measurement time. A similar smoothing effect should be expected when comparing the octave band levels in Figs. 5b, 6b, and 8b to the same levels determined for 1/3 octave bands. On closer inspection, however, a second effect can be seen. The determined levels at an octave band resolution are higher compared to what would have been expected based on simple level addition of contributing 1/3 octave levels. This discrepancy can be attributed to the fact that the level minima in the octave bands do not coincide in time with the minima of the 1/3 octave bands.

In the stage machinery industry it is common to consider noise requirements in single-number values (see Section 1.2), but this approach ignores the spectral composition of the noise. Considering Figs. 5b, 6b, and 8b, the distribution of the performance noise is dependent on frequency. Limit definition without considering this dependency can be a problem especially in the case of narrow-band noise typically generated by machines. The 1/3 octave bands provide best details about the frequency distribution of noise, but the number of values can be inconvenient for practical use. The consideration in octave bands as an established practical approach for noise criteria [3,4,7–9] reduces the data compared to 1/3 octave while still revealing sufficient information. Therefore, octave bands (see Tables 3–5) are best suited to define the noise limits.

The last aspect to discuss regarding spectral content is the suitability of the limits for noise sources with known characteristics, i.e. featuring tonality or impulsive impact noise during operation. The audibility of tonal components in noise spectra depends a lot on spectral masking. As masking can only be discussed in critical bandwidths (i.e. 1/3 octave bands for mid and high frequencies) octave band noise limits are not sufficient. From a practical point of view a limit penalty of up to 5 dB to the octave band limits may seem appropriate. The scientific sustainability of such rules of thumb should be subject to future investigations.

4.5. Comparison to tender documents

The determined total levels can be compared with the total levels published in tender documents. Fig. 11 shows the histogram

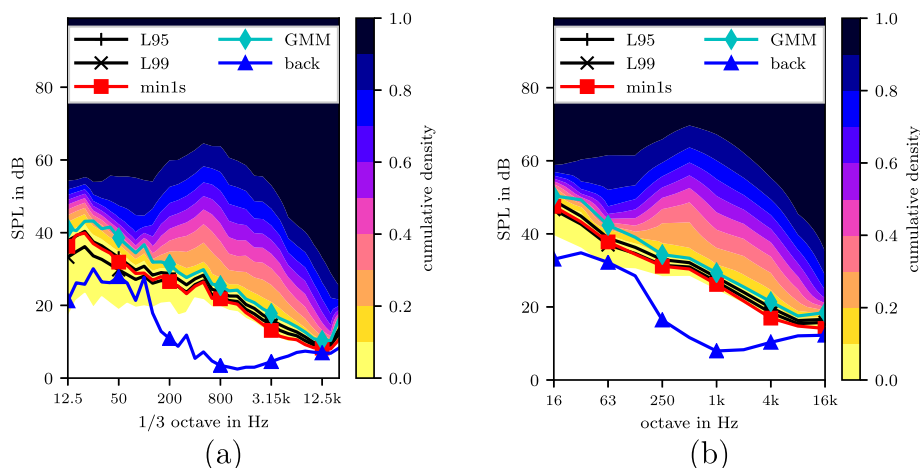


Fig. 8. Drama measurement and analysis results. (a) in 1/3 octave bands, (b) in octave bands.

Table 5

Merged drama results: min1s levels, GMM minimum mean values and L_N levels.

1/3 octave Hz	min1s dB	GMM dB	L_{95} dB	L_{99} dB
16	47.5	50.4	49.1	46.6
31.5	43.3	49.3	44.8	42.7
63	37.8	42.3	38.8	37.0
125	34.4	39.0	36.3	34.6
250	31.1	34.3	32.9	31.4
500	30.4	33.3	32.1	30.9
1 k	26.2	29.3	28.1	26.9
2 k	21.6	25.5	24.0	22.7
4 k	16.9	21.4	19.8	18.4
8 k	14.8	17.5	16.3	15.4
16 k	14.1	18.4	16.6	15.8
Total (A)	32.1	35.1	33.9	32.9

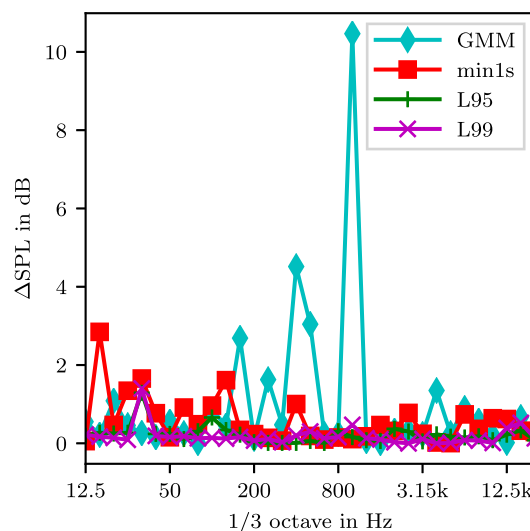


Fig. 10. Differences between two measurements of *Un Ballo in Maschera*.

of required levels from tenders [16] on the left and the measured levels of this study on the right. The total levels during drama performances (black circles) show the smallest scatter. The mean value of limits required in tenders somewhat corresponds to the levels that were measured in drama performances. For opera performances the comparison is less clear. While the very stringent min1s level also fits to the average of the tender requirements fairly well, a small change in the evaluation basis leads to a situation where the tender limits well exceed the determined L_{99} level.

4.6. Practical implications

Based on the discussion of the imperceptibility probabilities, it seems reasonable to distinguish between two scenarios.

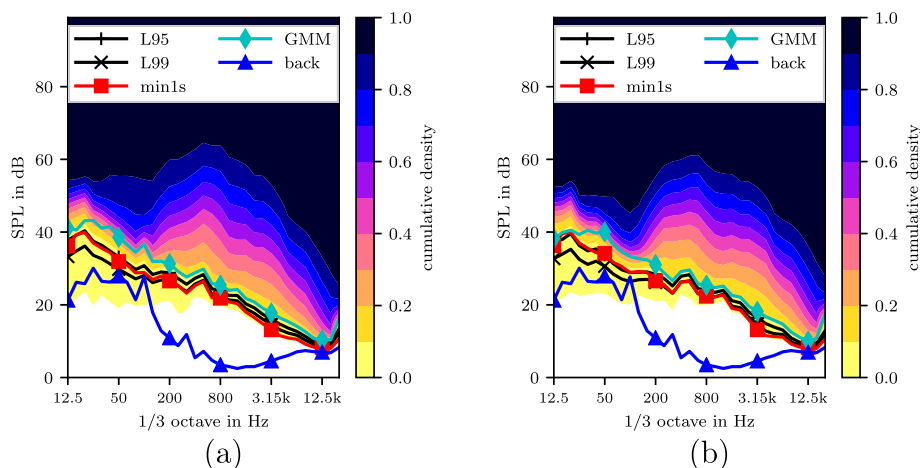


Fig. 9. Drama individual measurements and analysis results. (a) *Jeder stirbt für sich allein*, (b) *Amphitryon*.

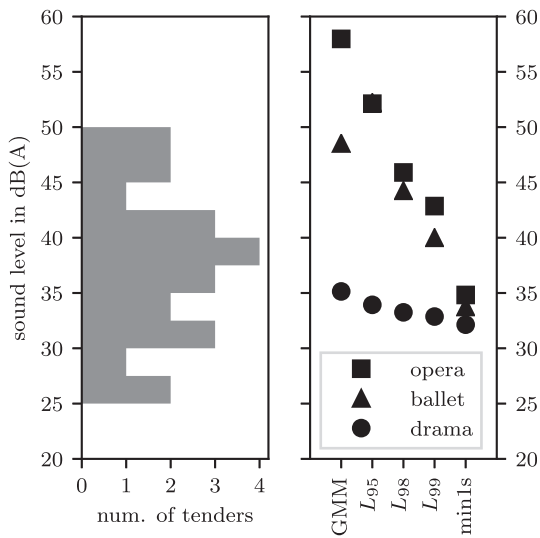


Fig. 11. Histogram of required levels from tenders [16] on the left and analysis method results (GMM, L_N , and min1s) applied on measured total levels on the right.

In standard environments, where a small chance to encounter audible stage machinery noise during a performance of approximately 0.03% is acceptable, noise limits based on L_{99} seem to be of practical use. To allow more artistic freedom and guarantee that the stage machinery is inaudible even throughout the quietest moments of a performance, min1s limits seem preferable in sensitive environments.

The limits for different art forms and sensitivities are shown in Fig. 12. For opera, the standard limits are illustrated by the red solid line and the sensitive limits by the magenta dashed line. In the case of ballet, the standard limit is given by the blue solid line and the sensitive limit by the cyan dashed line. Due to negligible difference between min1s and L_{99} limits for drama, only one noise limit needs to be specified. The numerical values are listed in

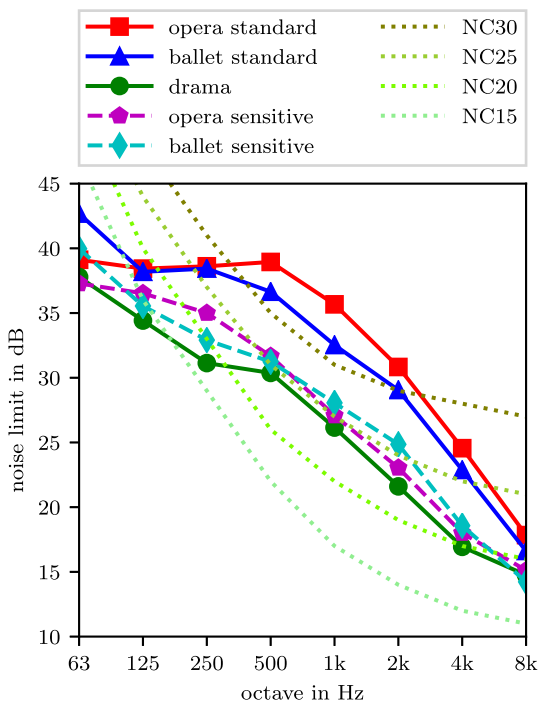


Fig. 12. Noise limits (L_{eq}) for stage machinery in opera, ballet, and theater play in octave bands with NC-curves (dotted lines) in background.

Table 6. The values in brackets are close to the background noise level (see Figs. 5b, 6b, and 8b, blue solid line) and should be used with the proviso that they may not be suitable for very quiet environments. The total level limits in dB(A) are stated as supplemental information. As masking plays a significant role in noise perception, the spectral content is relevant and A-weighted total levels may not be of practical use.

4.7. Limiting factors

The number of investigated venues is limited by the challenge to get access to the middle of the first row during live performances with audience during day-to-day operation of a performing art venue. Comparison to other relevant publications [13,15,14,25] suggests that the sample size reported here is adequate and in many cases exceeds the number of investigated venues and recorded performances. Despite these efforts there is a lack of comparable (standardized) data that is generally available. As a result there is still a remaining theoretical chance of including outliers in the result. Ultimately, this probability can only be reduced by further investigations, which gradually lead to a comprehensive dataset. The drafting of a generally accepted measurement standard could be helpful in this endeavor. Taking the current state of knowledge into account, the presented results provide new insights into the levels during live performances in German venues. In the future, this measured data base can be extended by additional measurements including new venues on an international scale.

A potential limitation may be the lacking noise data of the operating stage machinery in the otherwise quiet hall. This limits the discussion to an assessment of likelihood whether the determined L_N levels are influenced by machine noise. Although impact seems rather unlikely, measured spectra would be preferable for a definite proof.

Eventually the findings of this study need to become subject to a perceptual evaluation. The perception of the machinery noise in the presence of continuous building service type sounds is a substantial investigation of its own and should be addressed in a future study. This study focuses on the technical description of performance sounds and can therefore provide a basis for perceptual evaluations to come.

As part of the probabilistic inaudibility discussion it was assumed that noise from the stage machinery is inaudible if it is of the same or lower level as other sounds that occur during a performance. This logic underestimates the ability of the human brain to separate multiple sound sources through binaural hearing. Binaural masking is currently difficult to quantify. New findings may

Table 6

Proposed noise limits (L_{eq}) for opera, ballet, and theater play in octave bands (unweighted) and total level (A-weighted). Values in brackets are close to the measured background noise in investigated venues and should be adapted if necessary.

Octave Hz	Opera		Ballet		Drama dB
	Standard dB	Sensitive dB	Standard dB	Sensitive dB	
63 Hz	(39)	(37)	43	(40)	(38)
125 Hz	38	(37)	38	(36)	(34)
250 Hz	39	35	38	33	31
500 Hz	39	32	37	31	30
1 kHz	36	27	33	28	26
2 kHz	31	23	29	25	22
4 kHz	25	18	23	19	17
8 kHz	18	(15)	17	(14)	(15)
Total, dB(A)	43	35	40	34	32

warrant changing the employed relationship to better recognize the auditive sensitivity.

5. Conclusion

Based on measurements in 4 German performing arts venues involving 12 live performances with audience $L_{\min 1s}$ and L_{99} have been identified as the most suitable criteria for requirements for stage machinery. The suitability discussion included the reproducibility of different criteria and their resilience against performance sound and stationary background noise. The results show the likelihood at which total levels occur under realistic conditions during performances of drama, opera, and ballet with audiences in octave and 1/3 octave bands ranging from 125 Hz–8 kHz. Understanding how likely levels at a given frequency occur in regular performances is relevant for the designers of stage machinery and technical directors. Producers of other stage equipment, architects, or musicians can also profit from these results.

Acknowledgments

Each author contributed in a different way to the whole of this work. A.M. is responsible for the design of the study, analyzing the raw data, preparing the figures, and writing the manuscript. M.M. and M.S. helped to choose the measurement equipment and setup the measurement. M.M. and M.G. conducted the measurements in Bayerische Staatsoper. I.W. and S.M. helped to develop and to discuss the analysis methods. I.W. revised the manuscript. The interpretation and discussion of the results was done jointly by all of the authors.

The authors would like to thank Christoph Höller for proofreading the manuscript.

The authors would also like to thank the technical directors of the Semperoper Dresden, Oper Leipzig, Bayerische Staatsoper and State Playhouse Dresden for permission to measure during the performances. Additionally, the authors would like to acknowledge Karsten Mattered, the technical director of the Bayerische Staatsoper, for providing detailed information on reverberation times of the Bayerische Staatsoper.

This manuscript is part of the cooperation project Pianissimo funded by ZIM supported by German Federal Ministry for Economic Affairs and Energy under the index ZF4128201AT5.

References

- [1] Ogawa T. Theatre engineering and stage machinery, consultancy series. Entertainment Technology Press; 2001.
- [2] Grösel B. Bühnentechnik: Mechanische Einrichtungen [Stage Machinery: Mechanical Installations]. De Gruyter 2015. <https://doi.org/10.1515/9783110356892>.
- [3] Beranek LL. Revised criteria for noise in buildings. *Noise Control* 1957;3(1):19–27.
- [4] VÉR IL, Beranek LL. Noise and vibration control engineering: principles and applications. John Wiley & Sons; 2006. doi:10.1002/9780470172568.
- [5] Beranek LL, Blazier WE, Figwer JJ. Preferred Noise Criterion (PNC) curves and their application to rooms. *J Acoust Soc Am* 1971;50(5A):1223–1228. 10.1121/1.191276.
- [6] ISO 1996-1:2016-03: Acoustics – Description, measurement and assessment of environmental noise – Part 1: Basic quantities and assessment procedures (2016).
- [7] Beranek LL. Balanced noise-criterion (NCB) curves. *J Acoust Soc Am* 1989;86(2):650–64.
- [8] ANSI S12.2:1995 Criteria for Evaluating Room Noise; 1995.
- [9] Blazier WE. Revised noise criteria for design and rating of HVAC systems. *Noise Control Eng J* 1981;16:64–73.
- [10] Barron M. Auditorium acoustics and architectural design. Taylor & Francis; 2009. <https://doi.org/10.4324/9780203874226>.
- [11] Rossing TD. Springer handbook of acoustics. New York: Springer; 2014. <https://doi.org/10.1007/978-1-4939-0755-7>.
- [12] Steinberg JC. The stereophonic sound film system – Pre- and post-equalization of compandor systems. *J Acoust Soc Am* 1941;13(2):107–14.
- [13] Jeong C-H, Marie P, Brunskog J, Petersen CM. Audience noise in concert halls during musical performances. *J Acoust Soc Am* 2012;131(4):2753–61.
- [14] Marie P. Background noise requirements and audience noise in performance spaces mathesis. Technical University of Denmark; 2009.
- [15] Kleiner M. On the audience induced background noise level in auditoria. *Acta Acustica United Acustica* 1980;46(1):82–8.
- [16] Melnikov A. Geräuschlos Bewegen, Ansätze zur Reduzierung der Schallemission der Untermaschinen [Silent Movement, Approaches for Noise Reduction of Understage Machinery]. Bühnentechnische Rundschau Sonderband 2015:36–9.
- [17] Tennhardt H-P. Grenzwerte der Schallimmission Bühnentechnischer Anlagen [Limits for Noise Emission of Stage Machinery Installations]. IEMB Infolblatt 1998;5:1–4.
- [18] Schirmer W, Ulrich O. Beating technology noise, ABTT 3, 2002.
- [19] Schirmer W. Zur Ermittlung des Standes der Technik für geräuscharme Bühnenpodien [Review of low-noise Stage Elevators], DAGA Proceedings, 2003.
- [20] Harris R. The drama of the silent move: control of noise from stage machinery in the Operaen Copenhagen, Proceedings of the Institute of Acoustics 27 (2), 2005.
- [21] Bühnen Köln Sanierung; Zusätzliche Technische Vertragsbedingungen (ZTV) Teil 3 - Akustische Anforderungen [Renovation of Bühnen Köln; Additional Technical Terms Part 3 - Acoustic Requirements]; 2013.
- [22] ISO 3382-1:2009-06 Acoustics - Measurement of room acoustic parameters - Part 1: Performance spaces (2009).
- [23] Brüel & Kjær, Product Data: Hand-held Analyzer Types 2250 and 2270 (2016).
- [24] Brüel & Kjær, User Manual: Hand-held Analyzer Types 2250 and 2270 (Feb. 2017). URL: <https://www.bksv.com/media/literature/Various/be1713.ashx>.
- [25] Newton JP, James AW. Audience noise – How low can you get? *Proc. Inst. Acoust.* 1992;14:65–72.
- [26] Beranek L. Concert halls and opera houses: music, acoustics, and architecture. Springer Science & Business Media; 2004. <https://doi.org/10.1007/978-0-387-21636-2>.
- [27] Cremer L, Müller HA. Die wissenschaftlichen Grundlagen der Raumakustik [Scientific Basis of Room Acoustics]. 2nd Edition. Stuttgart: Hirzel; 1978.
- [28] Fasold W, Sonntag E, Winkler H. Winkler, Bau- und Raumakustik [Building and Room Acoustics], Bauphysikalische Entwurfslehre. Berlin: VEB Verlag für das Bauwesen; 1987.
- [29] Fastl H, Zwicker E. Psychoacoustics: facts and models. Springer Berlin Heidelberg: Springer Series in Information Sciences; 2007. <https://doi.org/10.1007/978-3-540-68888-4>.
- [30] Sung HG. Gaussian mixture regression and classification Ph.D. thesis. Houston, Texas: Rice University; 2004.
- [31] Hodgson M, Rempel R, Kennedy S. Measurement and prediction of typical speech and background-noise levels in university classrooms during lectures. *J Acoust Soc Am* 1999;105(1):226–33.
- [32] Akaike H. Information theory and an extension of the maximum likelihood principle. New York, NY: Springer New York; 1998. https://doi.org/10.1007/978-1-4612-1694-0_15, pp. 199–213.
- [33] Schwarz G. Estimating the dimension of a model. *Ann. Stat.* 1978;6(2):461–4.
- [34] Melnikov A, Maeder M, Gatt M, Scheffler M, Marburg S. Development of a novel sound pressure level requirement for characterizing noise disturbances from theater and opera stages. *Proc. Meetings Acoustics* 2017;30(1):. <https://doi.org/10.1121/2.000063030013>.
- [35] ISO 20906:2009: Acoustics – Unattended monitoring of aircraft sound in the vicinity of airports; 2009.
- [36] Schick A. Schallbewertung: Grundlagen der Lärmforschung [Sound Assessment: Fundamentals of Noise Research]. Berlin Heidelberg: Springer; 2013.
- [37] García A, Faus L. Statistical analysis of urban noise levels. *Journal de Physique Colloques* 1990;51(C2):281–4.
- [38] García A, Faus L. Statistical analysis of noise levels in urban areas. *Appl. Acoustics* 1991;34(4):227–47. [https://doi.org/10.1016/0003-682X\(91\)90007-2](https://doi.org/10.1016/0003-682X(91)90007-2).
- [39] Olayinka OS, Abdullahi SA. A statistical analysis of the day-time and night-time noise levels in Ilorin Metropolis, Nigeria. *Trends Appl. Sci. Res.* 2008;3:253–66.
- [40] Ryu H, Park IK, Chun BS, Chang SI. Spatial statistical analysis of the effects of urban form indicators on road-traffic noise exposure of a city in South Korea. *Appl. Acoustics* 2017;115:93–100. <https://doi.org/10.1016/j.apacoust.2016.08.025>. URL: <http://www.sciencedirect.com/science/article/pii/S0003682X16302511>.
- [41] Park SH, Lee PJ, Lee BK. Levels and sources of neighbour noise in heavyweight residential buildings in Korea. *Appl. Acoustics* 2017;120:148–57. <https://doi.org/10.1016/j.apacoust.2017.01.012>. URL: <http://www.sciencedirect.com/science/article/pii/S0003682X17300403>.
- [42] IEC 60034-1:2010 Rotating electrical machines – Part 1: Rating and performance; 2010.

Acoustic metamaterial capsule for reduction of stage machinery noise

Anton Melnikov,^{1,a)} Marcus Maeder,¹ Niklas Friedrich,² Yan Pozhanka,³ Alexander Wollmann,⁴ Michael Scheffler,⁴ Sebastian Oberst,⁵ David Powell,⁶ and Steffen Marburg¹

¹Chair of Vibroacoustics of Vehicles and Machines, Boltzmannstrasse 15, Technical University of Munich, Garching, Bavaria 85748, Germany

²SBS Bühnentechnik GmbH, Bosewitzer Strasse 20, Dresden, Saxony 01259, Germany

³CADFEM-CIS, Kondrat'yevskiy Prospekt 15, Saint Petersburg, Northwestern Federal District 195197, Russia

⁴Applied Mechanics Group, University of Applied Sciences, Kornmarkt 1, Zwickau, Saxony 08056, Germany

⁵Centre for Audio, Acoustics and Vibration University of Technology Sydney, 15 Broadway, Sydney, New South Wales 2007, Australia

⁶School of Engineering and Information Technology, University of New South Wales, Northcott Drive, Canberra, Australian Capital Territory 2612, Australia

ABSTRACT:

Noise mitigation of stage machinery can be quite demanding and requires innovative solutions. In this work, an acoustic metamaterial capsule is proposed to reduce the noise emission of several stage machinery drive trains, while still allowing the ventilation required for cooling. The metamaterial capsule consists of c-shape meta-atoms, which have a simple structure that facilitates manufacturing. Two different metamaterial capsules are designed, simulated, manufactured, and experimentally validated that utilize an ultra-sparse and air-permeable reflective meta-grating. Both designs demonstrate transmission loss peaks that effectively suppress gear mesh noise or other narrow band noise sources. The ventilation by natural convection was numerically verified, and was shown to give adequate cooling, whereas a conventional sound capsule would lead to overheating. The noise spectra of three common stage machinery drive trains are numerically modelled, enabling one to design meta-gratings and determine their noise suppression performance. The results fulfill the stringent stage machinery noise limits, highlighting the benefit of using metamaterial capsules of simple c-shape structure. © 2020 Author(s). All article content, except where otherwise noted, is licensed under a Creative Commons Attribution (CC BY) license (<http://creativecommons.org/licenses/by/4.0/>). <https://doi.org/10.1121/10.0000857>

(Received 25 September 2019; revised 28 January 2020; accepted 19 February 2020; published online 5 March 2020)

[Editor: Kai Ming Li]

Pages: 1491–1503

I. INTRODUCTION

Noise control in mechanical and civil engineering requires compact, efficient, and low maintenance solutions. In particular, the control of noise emitted by machinery operating in theaters or operas, such as stage elevator drive trains, is quite demanding, with the emission limits being as close as possible to that of the background noise levels.^{1–3} This is naturally challenging for stage machinery designers, especially when the constraints of the venue do not allow the application of conventional noise control measures, such as elastic bearings, noise barriers, or sound capsules. Noise at frequencies below 1000 Hz is especially problematic, since conventional noise insulation structures are quite bulky at these frequencies, and space is generally a scarce resource in a stage environment.

One of the main noise sources of stage machinery drive trains are the gear boxes, where the noise is dominated by the gear mesh frequencies and their higher harmonics.^{4–6}

Figure 1 shows a measured noise spectrum of a typical stage machinery gearbox, showing a small number of distinct peaks. The strongest peak is found below 1000 Hz, and its suppression would be the most effective means to reduce the overall noise emission. Since the stage machinery manufacturer is unable to influence the noise emission of the gearboxes directly, secondary noise control measures are required. Sound capsules can be very effective for noise reduction, but also have drawbacks, which limit their applicability to stage machinery. First, sound capsules are often ineffective below 1000 Hz, which is often the most important frequency range, and second, typical sound capsules do not allow air flow, which may lead to overheating of the encapsulated machinery. Typically, stage machinery is operated in intermittent periodic duty cycle S3 40%, which requires sufficient heat exchange by forced or natural convection.⁷ Therefore, in this work a novel meta-capsule (acoustic metamaterial capsule) is introduced, which can overcome these drawbacks.

Acoustic metamaterials offer a broad variety of opportunities to manipulate propagating acoustic waves⁸ by

^{a)}Also at: SBS Bühnentechnik GmbH, Bosewitzer Strasse 20, Dresden, Saxony 01259, Germany. Electronic mail: anton.melnikov@tum.de

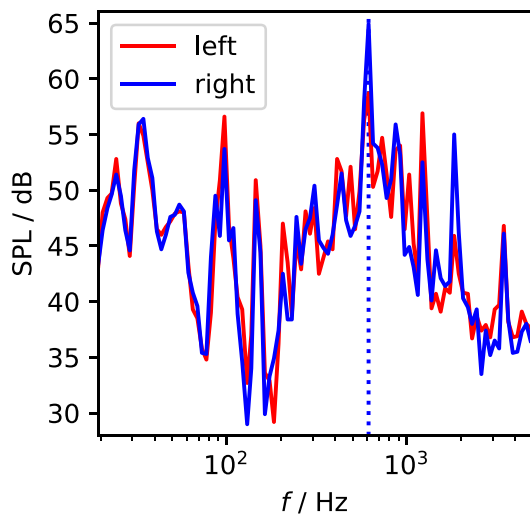


FIG. 1. (Color online) Noise emission of a gearbox of a rope drive system for left and right rotation directions as by the gear box supplier. The blue dotted vertical indicates the frequency of the highest emission.

introducing media properties such as negative bulk modulus⁹ or negative dynamic mass density.¹⁰ These principles have been utilized to create acoustic superlenses^{11–13} and acoustic barriers.^{14–16} The latter is a promising approach for noise control, where useful concepts have already been demonstrated.^{17–21}

Fard *et al.*¹⁷ conducted a numerical study on periodic Helmholtz resonators showing promising results for noise control applications over a frequency range of more than one octave. Henneberg *et al.*¹⁸ demonstrated and experimentally verified an elastic stop-band material to reduce velocity cross-coupling of ultrasonic transducers by 10 dB. In a subsequent study, Henneberg *et al.*¹⁹ expanded the ideas to multi-frequency applications. Claeys *et al.*²⁰ presented a sound insulating meta-capsule comprised of elastic resonators embedded in a two-dimensional lattice, reducing sound pressure level (SPL) by 20 dB. Marinova *et al.*²¹ realised a transmission loss of up to 25 dB at 130 Hz for a membrane-type metamaterial noise barrier. However, these approaches all make use of an airtight sound capsule, preventing ventilation and increasing the risk of machinery overheating.

Metamaterials which allow air flow have been developed, based on perforated membranes^{22,23} and space coiling structures.^{24–28} The air-permeable meta-grating realized by Cheng *et al.*²⁴ demonstrated 93% insertion loss while having a thickness 0.15 times the wavelength at 500 Hz. Later, a whole acoustic metacage allowing forced fluid flow through it was designed and verified experimentally by Shen *et al.*²⁹ All of these approaches rely on reflection or redirection of the sound wave, without attempting to engineer absorption. Acoustic metamaterial absorbers have been proposed.^{30–33} Wu *et al.*³⁰ make use of energy dissipation due to the friction in thin channels during the resonance. This principle allows an absorption of 88.9% to be achieved with a single layer of metamaterial.³¹ Lee *et al.*³² proposed arrays of paired Helmholtz resonators with an absorption of over 90% at 2200 Hz that could simultaneously be used to control the

direction of air flow. Xiang *et al.*³³ designed a stackable, ultra-open metamaterial absorber with broadband performance, having a measured absorption coefficient above 0.6 for a frequency range between 500 and 720 Hz. Although many acoustic metamaterials have been developed and experimentally verified, there have been very few demonstrations of their performance outside of a controlled laboratory environment. Acoustic metamaterials which allow for ventilation have been applied to windows,^{34,35} where the noise spectra and suppression requirements differ significantly from those of machinery noise.^{1,3,36}

An important drawback of the structures presented in Refs. 23, 24, and 32 is that they strongly reflect the incident field only within a narrow frequency range. This can limit the noise control applications of acoustic metamaterials to tasks where the noise emission is dominated by narrow band noise spectra,^{4–6} where a measurement example of gear induced SPL with a narrow peak is shown in Fig. 1. Accordingly, effective noise reduction of such emissions by a narrow band meta-grating is possible, but only if the meta-grating is tailored to the noise spectrum of the source. To date, it has not been demonstrated whether acoustic metamaterial sound barriers allowing ventilation can meet the requirements for machinery noise control.

The desired properties of metamaterials originate from localized resonances, asymmetries, or phase shifts in periodically arranged unit cells, called meta-atoms. The design of such properties requires complex fine features or exotic geometric shapes, which usually require sophisticated manufacturing technologies. However, the resonant properties required for strong reflection can be achieved with simpler meta-atom structures. Recently, we demonstrated a c-shape meta-atom consisting of a cylindrical Helmholtz resonator,³⁷ which facilitates manufacturing using conventional industrial technologies, e.g., mechanical processing. Furthermore, this meta-atom provides a number of additional properties such as reduced thermo-viscous losses and coupling between the monopolar and dipolar degrees of freedom, known as Willis coupling,³⁸ which gives additional flexibility in controlling the acoustic response of a metamaterial. It was demonstrated that Willis coupling can be tailored to achieve any value up to the theoretical limit.^{37,39} The ease of manufacturing the metamaterial structures presented in Ref. 37 makes them an ideal building block for air-permeable noise control structures, building on the concepts presented in Refs. 24 and 32.

In this work we present a metamaterial capsule design and apply it directly to stage machinery in order to reduce the noise induced by gears. In Sec. II, we design a reflective meta-grating based on c-shape meta-atoms and, subsequently, we expand this design to a full 3D meta-capsule prototype. The transmission loss of this prototype is modelled numerically and verified experimentally. In Sec. III, a meta-capsule is designed for the rope drive system, one of the most common drive trains in stage machinery. The transmission loss of the meta-grating is tailored to the measured noise spectrum of the gear-box. The numerically determined

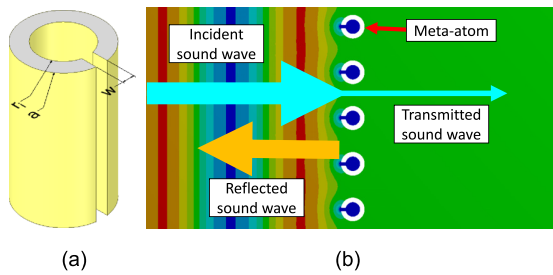


FIG. 2. (Color online) (a) c-shape meta-atom with dimensions, as proposed in Ref. 37. (b) FEM simulation of wave reflection from the meta-grating. The background color scheme shows the magnitude of the sound pressure.

transmission loss is then compared with the measurements under realistic conditions. Furthermore, the ventilation performance of the meta-capsule is verified by numerical studies considering natural convection. In Sec. IV, we demonstrate a numerical approach for modelling of stage machinery noise induced by gearboxes. It is applied to three typical stage machinery drive trains: push chain, gear rack, and spiralift. We then identify critical emission peaks of these drive trains and propose tailored multilayer meta-gratings for effective noise reduction while still allowing ventilation.

II. META-CAPSULE PROTOTYPE

Inspired by the promising concepts proposed by Quan *et al.*,³⁹ Cheng *et al.*,²⁴ and Lee *et al.*³² we use a resonant c-shape meta-atom³⁷ to create a 2D meta-grating. The c-shape meta-atom is shown in Fig. 2(a) and has the following

dimensions: outer radius $a = 19$ mm, inner radius $r_i = 12$ mm, and neck width $w = 5.5$ mm. Positioning the meta-atoms periodically with a lattice constant (distance between the meta-atoms) of $d = 4a = 76$ mm creates a meta-grating, as shown in Fig. 2(b). Due to the strong response of the meta-atoms, this meta-grating can significantly affect the sound field and provide strong reflection of the acoustic waves even when the meta-atoms are arranged to have notable gaps between them.

The transmission loss of the meta-grating was calculated by the finite element method (FEM) using ANSYS MULTIPHYSICS⁴⁰ for a normally incident wave. The mesh element size was 1 mm inside and around the meta-atom, while the size in all other regions was 3 mm. The element type is a 20-node element with a quadratic interpolation function. The transmission loss is calculated without considering impedance boundary conditions or thermo-viscous losses, and it is shown in Fig. 3(a) (red solid line) with a peak of 97 dB located at 1513 Hz. This transmission loss was achieved for a 2D geometry, with no obliquely incident wave components, so it neglects several important 3D effects which can reduce the transmission loss.

To expand the 2D meta-surface to a 3D structure, we design a meta-capsule prototype to reduce emission from the encapsulated noise source to the outside of the meta-capsule. The meta-capsule is a box with dimensions 350 mm × 310 mm × 310 mm and its structure and photograph are shown in Figs. 3(b) and 3(c), respectively. The role of the meta-grating is to reflect acoustic waves and any

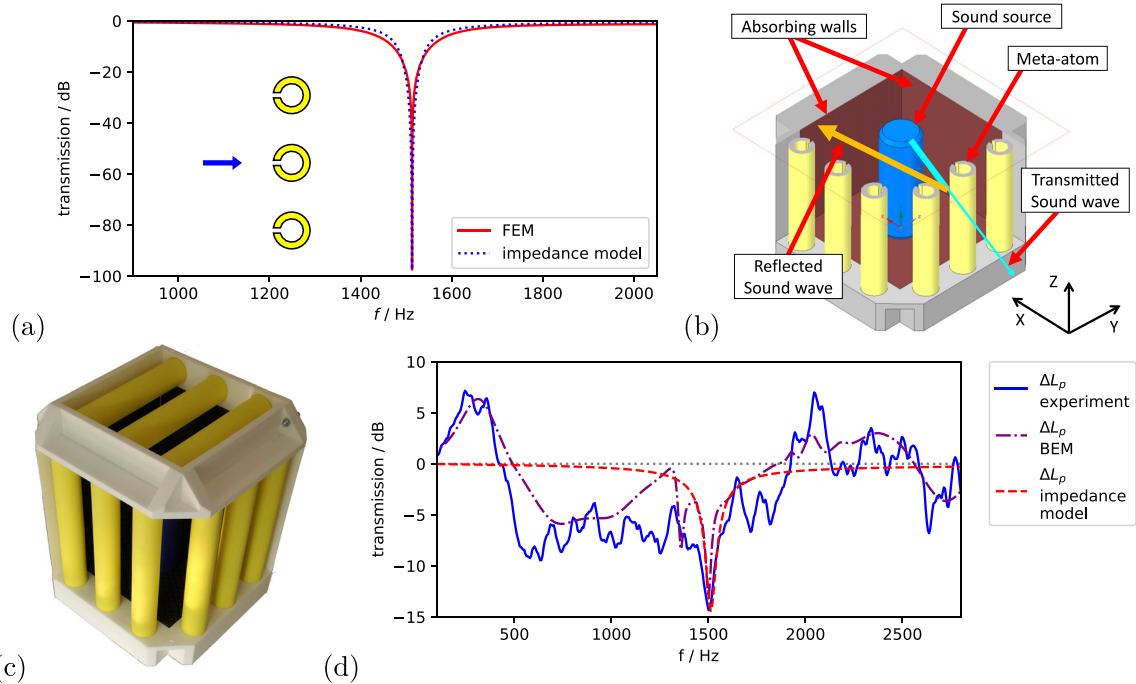


FIG. 3. (Color online) (a) Transmission loss determined using FEM (red solid line) and impedance model [blue dotted line, according to Eq. (3)] for a normally incident wave (blue arrow) for infinite meta-grating with a lattice constant $d = 76$ mm. (b) Meta-capsule prototype concept: the sound wave is redirected by the meta-grating to the absorbing wall. (c) Photograph of manufactured meta-capsule. (d) Transmission of the meta-capsule prototype measured (blue solid line) and simulated (purple dash-dotted line). Red dashed line shows transmission of the meta-capsule calculated using Eq. (3). ΔL_p is the ratio between the sound radiation with and without the meta-capsule.

internal losses within the c-shaped elements will cause unwanted transmission of waves. Therefore, we separate the absorption and reflection functions into different walls of the meta-capsule. Three sides of the meta-capsule contain an air-permeable meta-grating to redirect the sound wave and the side opposite each meta-grating contains absorbing foam to dissipate the redirected wave. Figure 3(b) shows a schematic of the incident wave generated by the sound source being reflected by the meta-grating and subsequently being absorbed by the foam.

To determine the transfer function of the 3D meta-capsule prototype, we apply the in-house 3D boundary element method (BEM) code *AKUSTA*, using continuous elements with a quadratic interpolation function.⁴¹⁻⁴³ The sound source was modelled as a chamfered cylinder, matching the shape of the commercial loudspeaker model *Ultimate Ears Boom 2*, with a diameter of 65 mm and height of 180 mm. This loudspeaker is used subsequently for the experimental validation. A normal surface velocity of 1 m/s was applied uniformly over the source surface. The acoustic transfer function was determined by analyzing two situations, a free loudspeaker on the bottom plate and a loudspeaker covered by the meta-capsule. The sound pressure was compared at the reference point $\mathbf{r}_{\text{ref}} = [-1, 0, 0]$ m relative to the center of the source, as per the coordinate system shown in Fig. 3(b). The density and acoustic velocity of air were set to $\rho_0 = 1.2 \text{ kg m}^{-3}$ and $c = 343 \text{ m s}^{-1}$, respectively.

Figure 3(d) shows the simulated transmission of the capsule at the reference point \mathbf{r}_{ref} (purple dash-dotted line). A transmission loss peak of 13 dB is observed at 1500 Hz, corresponding to the transmission loss peak of the 2D meta-surface. The curve demonstrates additional features, including a valley between 500 and 1300 Hz with a transmission loss of up to 6 dB and a smaller peak of 8 dB at 1350 Hz. Additionally, an increase in transmission is present below 500 Hz with a peak of 7 dB at 300 Hz and above 2000 Hz with values up to 3 dB. So long as this transmission increase does not correspond to any of the noise peaks of the

encapsulated machinery, it will have minimal effect on the total noise emission. However, the drop of 13 dB at the operating frequency of 1500 Hz shows that the meta-capsule is promising for the suppression of narrowband noise sources.

While the transmission loss at 1500 Hz can be readily explained by the transmission properties of the 2D meta-grating, to understand the other features, we need to consider the change in power radiated by the loudspeaker when the meta-capsule is added (see blue solid line with stars in Fig. 4). It is observed that the radiated source power depends on the frequency, and it is suppressed in regions between 600 and 1300 Hz and 1550 and 1800 Hz. Consequently, this changes the SPL measured outside the meta-capsule, where a similar reduction is present (see red dashed line in Fig. 4). Therefore, the broadband transmission effects observed in the SPL are mainly due to the change of the source's radiation impedance. This same effect is responsible for the increase in emission below 500 Hz and above 1800 Hz, where the meta-capsule effectively becomes an impedance-matching structure. Similarly, the farfield radiated power (see dark-blue solid line with crosses in Fig. 4) follows the trend of the source radiated power, however, the farfield power has a negative peak close to 1500 Hz caused by the meta-grating. The change of the source radiated power is linked to the Purcell effect in optics,⁴⁴ which was recently demonstrated experimentally for acoustic waves.^{45,46} Related discussions of the influence of radiation impedance on the radiated sound power can be found in several textbooks.^{47,48}

A. Experimental validation of the prototype

For experimental validation of the acoustic transfer function, the meta-capsule prototype was manufactured. The individual parts were printed using selective laser sintering from polyamide and mounted together using silicone to seal the gaps. The absorbing walls were created by gluing a 40 mm layer of the commercial absorbing material *Cellofoam 471/SK*⁴⁹ onto a 10 mm layer of polyamide. The

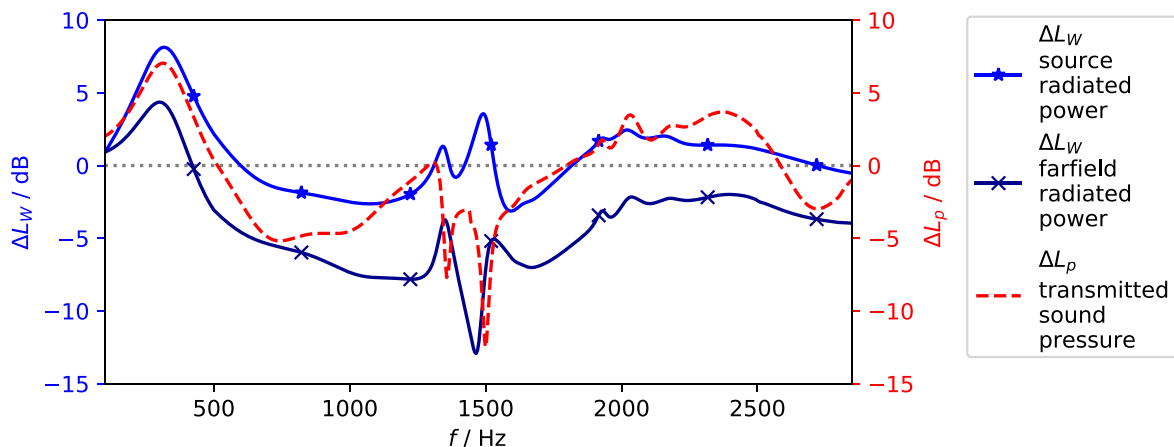


FIG. 4. (Color online) Numerically calculated change in sound power radiated from the loudspeaker and farfield radiated power, compared with the sound pressure transmitted through the meta-capsule prototype shown in Fig. 3(b). Broadband regions of SPL attenuation are caused by the change of the radiated source power, due to the change of the radiation impedance induced by the meta-capsule.

transfer function was determined using white noise excitation of the loudspeaker and recording the sound pressure with a Bruel&Kjaer hand-held analyzer type 2270, equipped with an 1/2-in free-field microphone type 4189 and a ZC-0032 preamplifier. The microphone was calibrated before measurement with the pistonphone type 4228 (Bruel&Kjaer), and the calibration was verified after measurement to ensure parameters had not changed during measured. The measurement was executed in an environment with a background noise level at least 10 dB below the measured values in the frequency range of interest. The microphone was positioned at the same reference point as in numerical simulation, $\mathbf{r}_{\text{ref}} = [-1, 0, 0]$ m. The transmission loss was determined by comparing measured sound pressure with and without the meta-capsule.

The measured transmission function of the manufactured meta-capsule prototype is shown as the blue solid line in Fig. 3(d). The maximum transmission loss at 1500 Hz is about 14 dB, which is slightly above the numerically predicted value of 13 dB. This peak is caused by the meta-grating. Over the frequency range between 500 and 2000 Hz, the transmission is reduced by approximately 7 dB, similar to the numerical result. Furthermore, we can observe an increase in transmission below 500 Hz and above 1800 Hz, due to the change in radiation impedance of the source.

B. Transmission loss modeling using impedance

The transmission loss peak of the meta-capsule can be calculated using a simple impedance model for acoustic filters.^{48,50} From the response shown in Supplementary Equation S37 of Ref. 37 we can write the impedance of a layer of meta-atoms as

$$Z_{\text{MA}}(\omega) = \frac{2A_d}{A_w} \left(i\omega\rho_0 l_{\text{eff}} + b - \frac{iK}{\omega V} A_w \right), \quad (1)$$

where A_d is the meta-grating cross section belonging to one meta-atom, A_w is the c-shape's aperture cross section, i is the imaginary unit, ω is the angular frequency, ρ_0 is the density of air, $l_{\text{eff}} = l + c_{\text{eff}}w$ is the effective aperture length,⁴⁸ K is the bulk modulus of air, V is the c-shape's inner volume, and b is the damping. Considering the characteristic impedance of air $Z_0 = \rho_0 c$, we can write the impedance of the meta-grating as

$$Z_{\text{MG}} = \left(\frac{1}{Z_{\text{MA}}} + \frac{1}{Z_0} \right)^{-1}. \quad (2)$$

Subsequently, the transmission can be calculated according to

$$\Delta L_p = 20 \log_{10} \left(1 - \left| \frac{Z_{\text{MG}} - Z_0}{Z_{\text{MG}} + Z_0} \right| \right). \quad (3)$$

Figure 3(a) demonstrates how this model matches the numerical results for a plane wave incident upon an infinite meta-grating. The empirical parameters $c_{\text{eff}} = 1.6$ and $b = 1 \times 10^{-4} \text{ Pa s m}^{-1}$ were found to produce good agreement.

Furthermore, Eq. (3) can be used to predict the transmission peak of the meta-capsule. However, due to finite meta-grating size and oblique incidence angle the transmission loss peak observed in Fig. 3(d) is less effective. Subsequently, to represent the efficiency drop the damping can be set to an artificial value $b = 1.75 \text{ Pa s m}^{-1}$, which results in good agreement with simulation and experiment [see Fig. 3(d), red dashed line]. In Sec. IV we consider multilayer meta-gratings, where N different meta-atom layers of multilayer meta-grating can be combined as

$$Z_{\text{MG}} = \left(\sum_{n=1}^N \frac{1}{Z_{\text{MA},n}} + \frac{1}{Z_0} \right)^{-1}. \quad (4)$$

III. DESIGN AND EXPERIMENTAL VALIDATION IN APPLICATION

A. Design for a rope drive system

Rope drives are very popular for applications with high acoustic requirements, since they allow a very quiet stage machinery to be constructed.⁵¹ Although many other noise sources are avoided in rope drive systems, gearboxes are still required and their noise emission can be highly intrusive when not masked by additional noise sources. The rope drive system considered herein is shown in Fig. 5(a). The electric motor drives a pair of rope drums using silent chains. The measured noise emission of the gear box used for this system is presented in Fig. 1 for both rotation directions. It was observed that a dominant peak is present at 613 Hz (blue dotted vertical line), which is especially prominent for the right rotation. Therefore, in the following we propose a tailored meta-capsule to reduce this peak.

For this purpose we designed a meta-grating, which provides maximum transmission loss at 613 Hz. The meta-atom uses the c-shape presented in Fig. 2(a) with different dimensions: outer radius $a = 42.5$ mm, inner radius $r_i = 32.5$ mm, neck width $w = 10.6$ mm, and lattice constant $d = 110$ mm. The photograph of the designed and manufactured meta-capsule is shown in Fig. 5(b). The meta-grating is placed at one side of the capsule only and its surface normal is aligned parallel with the motor shaft. It has size $590 \text{ mm} \times 530 \text{ mm}$ and consists of an array of five meta-atoms. The meta-atoms are made from polyamide using selective laser sintering. To suppress vertical modes inside the c-shape cavity, two metal sheets divide the meta-grating into three regions. The central field has a missing meta-atom in the center to provide clearance necessary for the connection of the emergency drive. All other walls of the meta-capsule are made of steel sheets of thickness 2 mm combined with commercial absorber *Cellofoam 471/SK*⁴⁹ of thickness 40 mm. The meta-capsule encapsulates only the electric motor and the gear-box. The air flow necessary for ventilation is only possible through the meta-grating.

Based on the new geometry, the meta-grating transmission can be estimated with the red dashed curve in Fig. 5(c) according to Eq. (3). Using $b = 1.5 \text{ Pa s m}^{-1}$ results in 17 dB

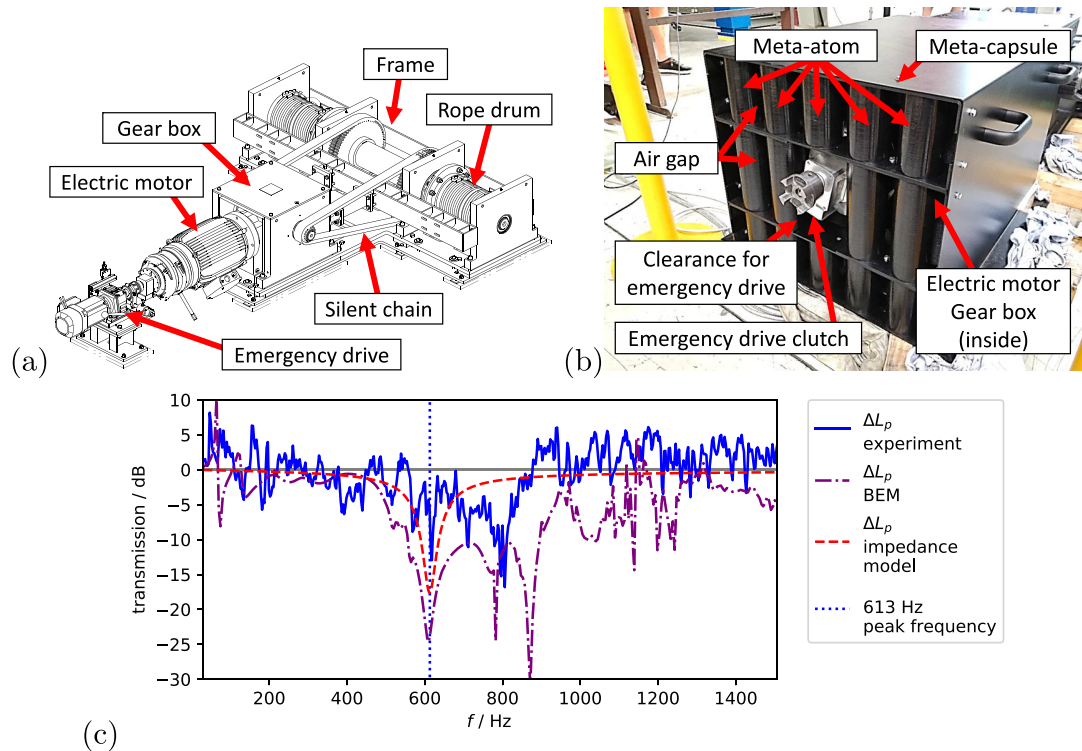


FIG. 5. (Color online) (a) Rope drive system with labels. (b) Photograph of the meta-capsule with electric motor and gear box inside. (c) Measured (blue solid line), simulated (purple dash-dotted line), and empirically estimated [Eqs. (3), red dashed line] transmission profile of the meta-capsule. Vertical blue dotted line corresponds to the peak observed in Fig. 1. ΔL_p is the ratio between the sound radiation with and without the meta-capsule.

transmission loss, which is close to the results demonstrated for the prototype meta-capsule in Fig. 3(d). Furthermore, we determine the transfer function of the meta-capsule by means of 3D BEM using continuous elements with a quadratic interpolation function. For simplification, the motor and the gearbox have been assumed to be the only sound sources in the model. The normal surface velocity was normalized to $v_n = 1 \text{ m s}^{-1}$ and applied uniformly over the motor and gear box surfaces. The sound transfer function was determined by calculating transmitted pressure for the electric motor and gear box inside the meta-capsule, and normalising this to pressure for the same situation with the meta-grating removed on one side only. The medium density and the speed of sound are set to $\rho_0 = 1.2 \text{ kg m}^{-3}$ and $c = 343 \text{ m s}^{-1}$, respectively. The numerically determined transmission profile is shown by the purple dash-dotted line in Fig. 5(c). Three transmission loss peaks are observed, 24 dB at 613 Hz, 24 dB at 780 Hz, and 30 dB at 880 Hz. The peak at 613 Hz is caused by the tailored meta-grating design.

B. Experimental validation in application

The designed meta-capsule was manufactured using the procedure outlined in Sec. II A. For the absorbing walls, the porous material was attached to 2 mm thick steel sheets. The meta-capsule's transfer function was determined using the natural excitation of all active components during the operation at maximum rotational speed of approximately

1490 min^{-1} . The data was acquired with a 1/4-in free-field PCB microphone and Squadriga Frontend (Head Acoustics). The microphone was calibrated with a pistonphone type 4230 B&K (Bruel&Kjaer). The measurements were conducted in a factory building, with a background noise level of at least 10 dB below the measured values in the frequency range of interest. The microphone position was 1 m away from the meta-grating and was concentric with the motor shaft axis. The transmission loss was determined the same way as for the prototype meta-capsule.

The measured transmission is shown in Fig. 5(c). The measurement confirms a peak very close to 613 Hz with a transmission loss of 14 dB. The measured transmission loss at the peak is less than that prediction by numerical calculation and closer to the value predicted by Eq. (3). We note that the meta-grating thickness is 85 mm, which is 0.15λ at 613 Hz (λ is the wavelength) hence below $\lambda/4$. There are two additional peaks present in the measurement, around 700 Hz and around 800 Hz. The confirmation of the designed transmission loss peak demonstrates the feasibility of the meta-capsule concept in application.

C. Ventilation performance of the meta-capsule

To demonstrate the ventilation properties of the designed meta-capsule, we conducted 3D Computational Fluid Dynamics (CFD) simulations solving the non-linear Navier-Stokes equations with the commercial code ANSYS FLUENT.⁴⁰ This allows the steady-state temperature during

operation to be determined, considering natural convection, and determining heat dissipation from the efficiency of the drive unit. The electric motor has a nominal power of 27 kW, which already includes a margin of safety $S=2$ required by the DIN 56950-1:2012-05 stage machinery standard.⁵² The used efficiency factors are $\eta = 0.94$ for the motor and $\eta = 0.97$ for the gear box, resulting in heating powers of 810 and 381 W, respectively. The periodic duty of the stage machinery is usually defined as S3 40%,⁷ which means an operation duration of maximum 40% during a 10 min cycle. For steady state configuration, this periodic duty type reduces the heating power by a factor of 0.4. For turbulent regions of air flow induced by natural convection we applied the $k-\omega$ SST turbulence model^{53,54} with the constants $\alpha_{\text{inf}} = 1$, $\alpha_{\text{inf}}^* = 0.52$, $\beta_{\text{inf}}^* = 0.09$, $a_1 = 0.31$, $\beta_i^{\text{Inner}} = 0.075$, and $\beta_i^{\text{Outer}} = 0.0828$. The environmental temperature was 20 °C. The heat transfer coefficient of the acoustic absorber was considered as $h_{\text{Cello}} = 0.04 \text{ W m}^{-1} \text{ K}^{-1}$ as specified by the manufacturer.⁴⁹

The CFD results at steady state are shown in Fig. 6. In Fig. 6(a) we observe that the meta-grating allows sufficient cooling by natural convection. It leads to a motor surface temperature of 85 °C, which is within the bounds given in Table VII of Ref. 7. However, as shown in Fig. 6(b), a conventional air-tight sound capsule would lead to temperatures above 140 °C, which would cause overheating of the electric motor (see Table VII in Ref. 7). Following this, a conventional sound capsule would not be recommended to be used in combination with the simulated drive train.

IV. MODELLING OF STAGE MACHINERY NOISE

In this section, we numerically analyze the application of the meta-capsule to the suppression of noise in other types of stage machinery, namely, push chain, gear rack, and spiralift systems. To design the meta-capsules, it is necessary to first characterize the noise emission from these stage machinery systems. All three systems had been designed to reduce the noise emission by the empirical methods common in stage machinery.

In this work we consider only the gear induced excitation, since this typically dominates stage machinery noise. The analysis of vibration due to mechanical motion was

done with the FEM, using the commercial software package ANSYS.⁴⁰ To determine the excitation forces, the gear mesh process was modelled for each system using FEM. The material of the gears and shafts is steel, with a Young's modulus of $E_{\text{St}} = 200 \text{ GPa}$, a Poisson ratio of $\nu_{\text{St}} = 0.3$, and a density of $\rho_{\text{St}} = 7850 \text{ kg m}^{-3}$. The fluctuation of the meshing force, which is affected by the time-varying mesh stiffness, is known to be the major source of noise and vibration.^{5,6} We use this force fluctuation to model the source in our analysis. As demonstrated in Refs. 5 and 6, the normal modes of the gears and the shafts can be neglected for the determination of the dynamic bearing force. Under the assumption of periodic excitation forces, the loads are transferred to the frequency domain with harmonic time dependence. This allows subsequent analysis of steady-state time-harmonic dynamics by means of the harmonic response.

The harmonic response was calculated using full power-train models up to 2500 Hz utilizing a modal superposition procedure with a preceding modal analysis up to 5000 Hz. The frequency range was limited by the model dimensions of several meters [see Figs. 8(a), 9(a), and 10(a)] but is sufficient to cover the important noise frequency range of stage machinery. Due to the complexity of the real structure and lack of accurate data, a representative damping ratio of $\zeta = 3 \times 10^{-2}$ was considered, as is commonly recommended for metal structures with joints.⁵⁵ The harmonic analysis yields the surface velocities of the whole structure required for the subsequent acoustic analysis.

At low frequencies, the directivity of the sound can be neglected, which allows the full acoustic analysis to be reduced to a sound power analysis. The calculation of the sound power of a mechanical system is usually done by solving a Robin problem with known normal velocity, known admittance boundary condition, and unknown sound pressure. After the sound pressure is obtained, the sound power follows as^{56,57}

$$P = \frac{1}{2} \Re \left\{ \int_{\Gamma} p(x) v_n^*(x) d\Gamma \right\}, \quad (5)$$

where $p(x)$ is sound pressure, $v_n^*(x)$ is the complex conjugate of the normal surface velocity of the fluid, and Γ is fluid-structure interface.

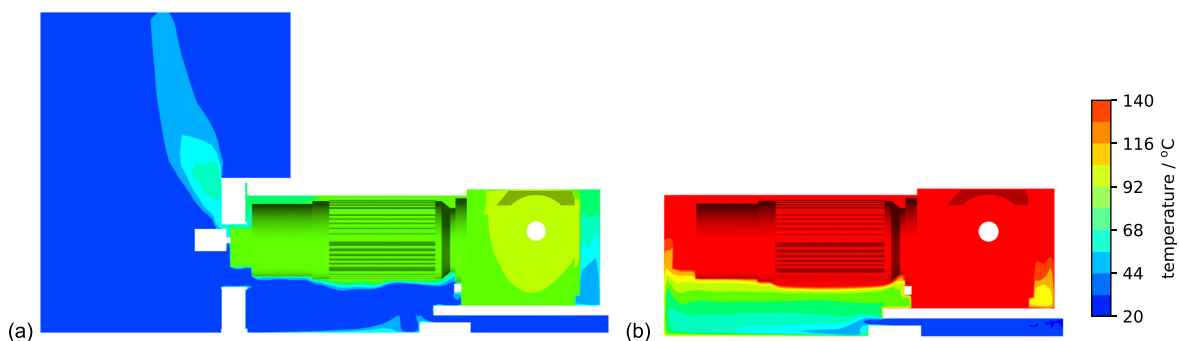


FIG. 6. (Color online) Temperature profile due to natural convection during stationary operation of the motor covered by (a) an air-permeable meta-capsule and (b) an airtight conventional sound capsule calculated using CFD. The meta-capsule results in a temperature of $\approx 85 \text{ °C}$ at the motor surface, whereas a conventional sound capsule would cause overheating of the motor with temperatures $> 140 \text{ °C}$.

If large models have to be considered, computation of sound pressure p requires significant computational effort, which can imply restrictions for geometrical details and for the frequency range. The computation of sound pressure can be avoided by utilizing sound power approximation methods, such as equivalent radiated power (ERP) or the lumped parameter model (LPM).^{56,58,59} ERP uses the assumption of unit radiation efficiency for the whole fluid-structure interface. Therefore, application of ERP on the power trains typically overestimates the sound power in the lower frequency range.⁵⁹ The LPM avoids general overestimation at low frequencies and is able to consider acoustic short circuits. This method is based on the approximation of the Rayleigh integral and is written as^{56,59}

$$P_{\text{LPM}} = \frac{1}{2} k \rho c \sum_{\mu} \sum_{\nu} \frac{\sin(k|\mathbf{r}_{\mu} - \mathbf{r}_{\nu}|)}{2\pi|\mathbf{r}_{\mu} - \mathbf{r}_{\nu}|} \Re\{v_{\mu} v_{\nu}^*\} A_{\mu} A_{\nu}. \quad (6)$$

More details on the performance of these methods can be found in Refs. 59, 60.

Commonly, the noise limits in stage machinery address the middle of the first row of the auditorium, see Fig. 7. To study the SPL at this location geometrical acoustics was solved using COMSOL MULTIPHYSICS.⁶¹ Therefore, this study considers only the air transmission path between the location of the drive train and the middle of the first row. The effective distance and the absorption of the surfaces are different in every venue, therefore the sound transfer function strongly depends on the hall. To determine the transfer function, a geometrical model of the auditorium including the stage is required. The newly build venue *Kraftwerk Mitte* in Dresden (Germany) was chosen as a reference hall for modeling of the transfer function. Thus, a model was derived from the geometry of the venue *Kraftwerk Mitte*. The absorption coefficients of the walls and chairs were

updated to represent the measured reverberation times. Additionally, the transmission loss of the stage floor separating the drive train location from the stage area was determined experimentally and implemented in the model. Finally, this model was used to determine the SPL in the middle of first row of auditoria originating from LPM sound power of two machines of the same kind below the stage (see Fig. 7).

Recently, we analyzed SPL data in the middle of the first row taken during live performances and proposed five different limit curves: opera standard, opera sensitive, ballet standard, ballet sensitive, and drama.³ These performance curves are illustrated in Figs. 8(c), 9(c), and 10(c). To avoid disturbance of the audience during the performance, stage machinery noise emission should remain below these limits. The simulation produces discrete frequency spectra, whereas the SPL limits are defined in octave bands.³ The measured SPL results from analog filtering of the sound analyzer. This filtering was reproduced by a digital Butterworth filter applied to the simulation data to enable its comparison with the limits obtained from analog measurements.³

Here, we present the numerical results of stage machinery noise. We observe that the considered noise spectra are dominated by a few sharp peaks, which can be reduced by surrounding the machinery in a meta-capsule. Furthermore, based on the previously presented outcomes, we propose a multi-layer meta-grating to reduce the noise emission during scenic performance to allowable levels.

A. Push chain

The FEM model of the push chain system demonstrating a vibration mode at 273 Hz is shown in Fig. 8(a). The simulated SPL in the first row is illustrated in Fig. 8(b) as a narrow-band spectrum (cyan solid line) and in Fig. 8(c) in octaves (red solid line with crosses). Furthermore, Fig. 8(c) shows five different noise limits in the first row of the auditorium during a scenic performance (dark lines with smaller markers).³ Comparison of the noise emission with the noise limits in Fig. 8(c) reveals that the emission exceeds some limits at 250 Hz, 1 kHz, and 2 kHz octaves.

Analyzing the noise spectrum in Fig. 8(b) allows the identification of critical peaks at 273, 1367, and 1638 Hz (cyan solid line). These peaks dominate the octave levels exceeding the limits. The critical peaks can be reduced by combining three different meta-gratings in a multilayer metamaterial. To match the peak frequencies with the transmission loss peaks the meta-grating should consist of the following c-shape geometries (a, l, w) in mm: (82, 10, 10), (20, 5.2, 6), and (16, 4, 4). The lattice constant was set to $d = 4a$ for all geometries. The empirical damping used in Eq. (3) was interpolated, then extrapolated as

$$b(f) = b_1 + \frac{b_2 - b_1}{f_2 - f_1} (f - f_1), \quad (7)$$

where f is the frequency, $b_1 = 1.5 \text{ Pa s m}^{-1}$, $f_1 = 613 \text{ Hz}$, $b_2 = 1.75 \text{ Pa s m}^{-1}$, and $f_2 = 1500 \text{ Hz}$ according to Secs. II and III. Using Eqs. (3) and (4), the transmission of such

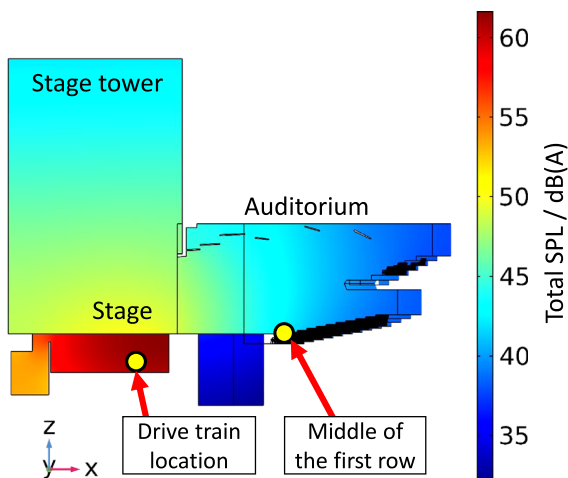


FIG. 7. (Color online) Sound level distribution calculated by geometrical acoustics in *Kraftwerk Mitte* (Dresden). The important locations are that of the drive trains below the stage and the reference point in the middle of the first row.

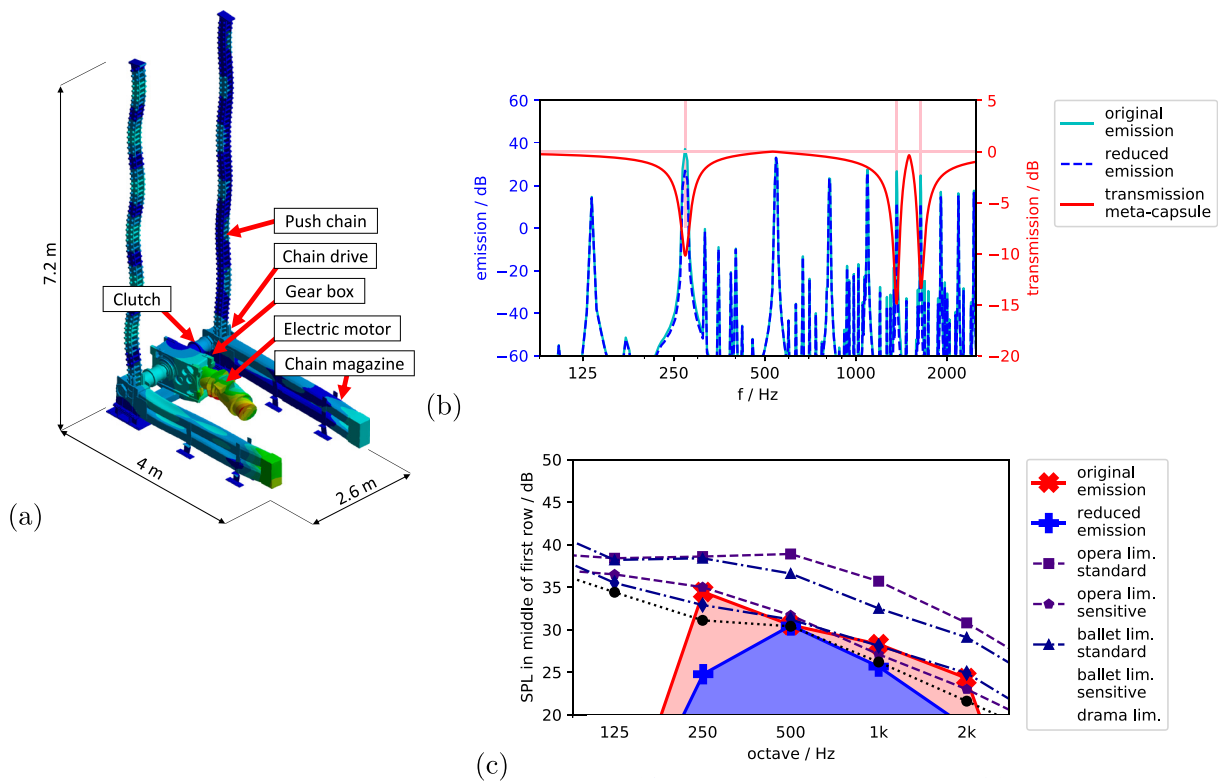


FIG. 8. (Color online) (a) Components and dimensions of the push chain system. The plot reveals a vibration mode at 273 Hz. (b) Simulated emission of the push chain system (cyan solid line) and the reduced emission by meta-capsule design (blue dashed line). The transmission of the meta-capsule (red solid line) is based on Eqs. (3) and (4) and tailored for the three critical emission peaks. (c) Original and reduced noise emission compared with the stage machinery noise limits in octaves.

multilayer metamaterial can be estimated by the red solid line shown in Fig. 8(b). Application of this transmission on the noise spectrum leads to the blue dashed line in Fig. 8(b), where the identified peaks are significantly reduced compared to the original emission (cyan solid line). The reduced emission in octaves is shown in Fig. 8(c), where now all five limit types are fulfilled at 250 Hz and 2 kHz. At the 500 Hz and 1 kHz octave bands, the sensitive limits for opera and ballet are fulfilled as well, whereas the drama limit (black dotted line with circles) is still slightly exceeded by approximately 1 dB.

B. Gear rack

The gear rack system is shown in Fig. 9(a). It illustrates a vibration mode at 545 Hz. Figure 9(b) illustrates the narrow-band SPL in the middle of the first row as a cyan solid line. Figure 9(c) shows the SPL in the middle of the first row in octaves (red solid line with crosses). It is observed in Fig. 9(b) that the sensitive limits are strongly violated for the 1 kHz octave band. Additionally, drama and sensitive ballet limits are slightly exceeded at the 2 kHz octave band.

The limit violation can be traced back to the SPL peaks at 817.0, 1094.2, and 1638.7 Hz [see Fig. 9(b)]. Based on these peaks the required c-shape geometries were chosen for (a, l, w) in mm: (32, 7, 8.5), (24, 6, 6), (16, 4, 4) with $d = 4a$ and b according to Eq. (7). The transmission function of such multilayer metamaterials is estimated using

Eqs. (3) and (4) and is depicted by the red solid line in Fig. 9(b). Application of these transfer functions on the noise emission leads to reduced emission shown in Fig. 9(b) (blue dashed line) and in Fig. 9(c) (blue solid line with pluses). It can be observed that all limits are fulfilled in Fig. 9(c).

C. Spiralift system

Figure 10(a) shows the spiralift system. This system differs slightly from the push chain and gear rack because it has two chains that require a chain tightener. The chain tightener provides local modes with relatively low eigenfrequencies. These modes get excited and even if the chain tightener area is relatively small, the magnitudes are large enough to produce dominant noise peaks. Such a mode at 282 Hz is illustrated in Fig. 10(a) producing the strongest SPL peak in Fig. 10(b) (cyan solid line). The resulting octave levels are demonstrated in Fig. 10(c) (red solid line with crosses), where almost all limits are violated between the 250 Hz and 2 kHz octave bands.

Since there are four octaves where the emission has to be reduced, at least four peaks are to be treated, one per octave. This requires a multilayer metamaterial with four different meta-grating layers. The critical peaks occur at 282, 560, 1119, and 1678 Hz in Fig. 10. The required c-shape geometries (a, l, w) in mm were chosen as (80, 9, 10), (45, 9.5, 10), (24, 7, 6), (16, 4, 4.5) with $d = 4a$ and b according to Eq. (7). The transmission function of the

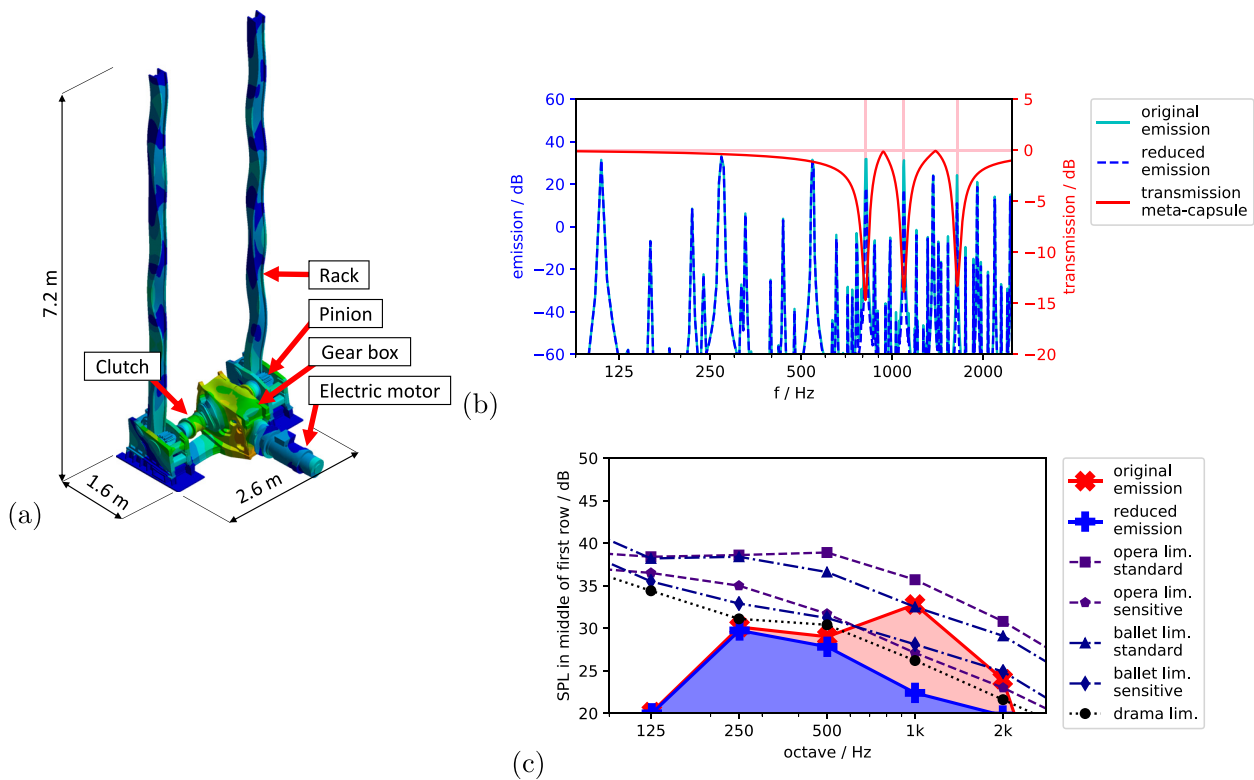


FIG. 9. (Color online) (a) Components and dimensions of the gear rack system. The plot reveals a vibration mode at 545 Hz. (b) Simulated emission of the gear rack system (cyan solid line) and the reduced emission by meta-capsule design (blue dashed line). The transmission of the meta-capsule (red solid line) is based on Eqs. (3) and (4) and tailored for the three critical emission peaks. (c) Original and reduced noise emission compared with the stage machinery noise limits in octaves.

metamaterial was estimated using Eqs. (3) and (4) and is shown in Fig. 10(b) as the red solid line. The reduced emission is shown in Fig. 10(b) as the blue dashed line and in Fig. 10(c) in octaves (blue solid line with pluses). The reduced emission fulfills standard opera and standard ballet limits. Furthermore, all limits are fulfilled for the 250 Hz octave band, whereas sensitive opera, sensitive ballet, and drama limits are still exceeded by up to 5 dB.

V. DISCUSSION

Two meta-capsules were investigated experimentally and numerically. In the case of the meta-capsule prototype, a reasonable agreement between simulation and experiment was demonstrated, see Fig. 3(d). The same level of agreement could not be observed during the validation of the meta-capsule on the rope drive system [see Fig. 5(c)], nevertheless, the existence of the transmission loss peak caused by the meta-grating was confirmed. The deviations can be attributed to geometrical simplification during the BEM modelling, misalignment during the manufacturing of the capsule, and neglect of the sound radiation contribution from the outer meta-capsule surfaces. Due to the simple geometry of the meta-capsule prototype, we were able to represent its shape exactly in the simulation. However, in the case of the rope drive system, the complex geometry of the cooling ribs of the electric motor [see Fig. 5(a)] and

some additional details had to be simplified before BEM modelling. Furthermore, sometimes the absorbing foam could not be mounted as intended during the design, which reduced the capsule's inner volume. The volume reduction could explain the shift of the peak pair from around 700 and 800 Hz in the experiment to around 780 and 880 Hz in the simulation. Finally, the BEM model considers only the noise radiated by the surface of the electric motor and the gear box, whereas many more surfaces contribute to the total sound radiation. We note that under these imperfect but realistic conditions, a transmission loss was still observed.

We demonstrated the potential of noise emission reduction based on three common stage machinery systems. In all three cases we could identify and treat the critical peaks in a way that the noise limits could be fully or partially fulfilled. Complete numerical modelling was not feasible due to the large model size compared to the required details of the metamaterial. Therefore, the transmission loss was estimated by the impedance model in Eqs. (3) and (4). This approach gives the engineer a simple tool for designing such meta-gratings, as was demonstrated for these three examples. Additionally, the cooling performance of the multi-layer meta-gratings can be tailored using CFD to fulfill the allowable temperatures similarly to the single-layer meta-grating shown in Sec. III C.

An alternative noise control solution allowing ventilation can be realized using sonic crystals.¹⁵ We therefore

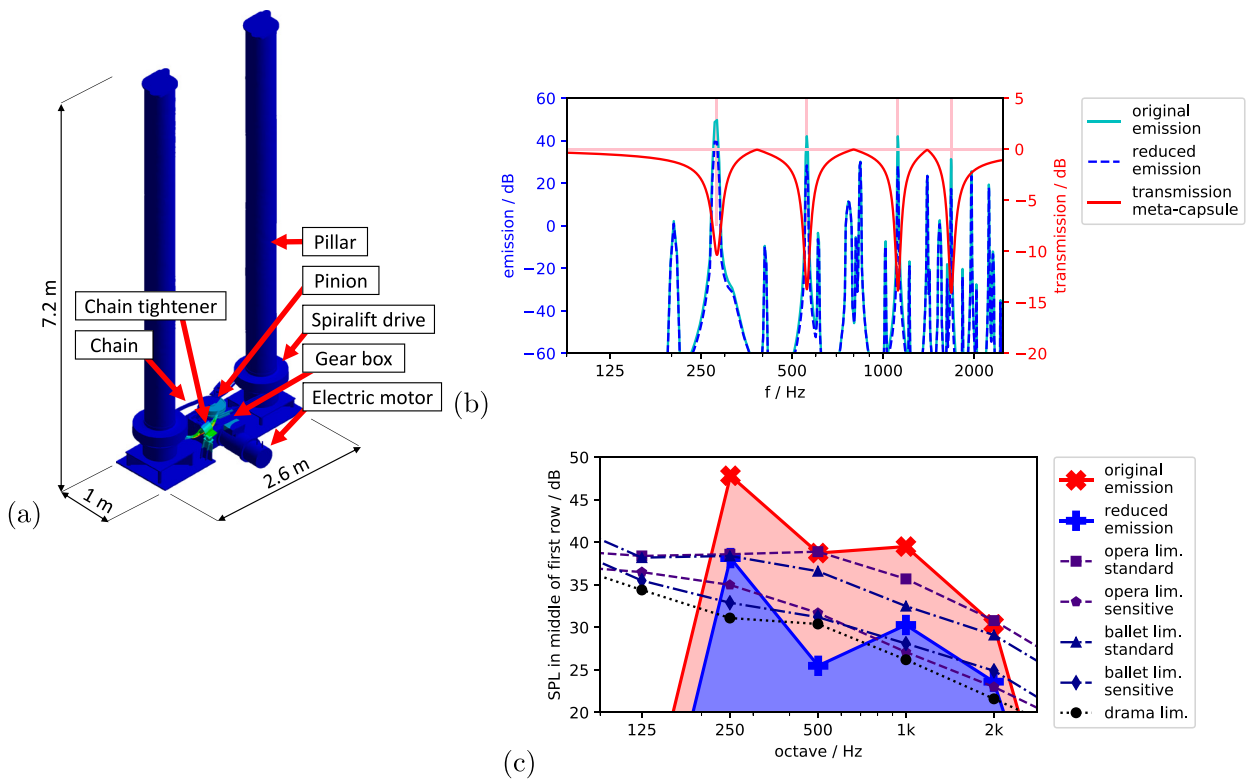


FIG. 10. (Color online) (a) Components and dimensions of the spiralift system. The plot reveals a local vibration mode at 282 Hz. (b) Simulated emission of the spiralift system (cyan solid line) and the reduced emission by meta-capsule design (blue dashed line). The transmission of the meta-capsule (red solid line) is based on Eqs. (3) and (4) and tailored for the four critical emission peaks. (c) Original and reduced noise emission compared with the stage machinery noise limits in octaves.

benchmark our meta-grating against a sonic crystal consisting of meta-atoms outlined in Sec. II. We also compare the performance of rigid cylinders in meta-grating and sonic crystal configurations, with a radius similar to that of the meta-atom radius a . The lattice constant used for sonic crystals is $d = 4a$. In Fig. 11, the c-shape sonic crystal

demonstrates two band gaps in the considered frequency range: 1333 to 1591 Hz and 1980 to 2636 Hz, where the first band gap is linked to the meta-atom resonance. Considering the sonic crystal of cylinders leads to only one band gap between 1744 and 2606 Hz. The effect of the band gaps can be observed in the transmission loss of the sonic crystal

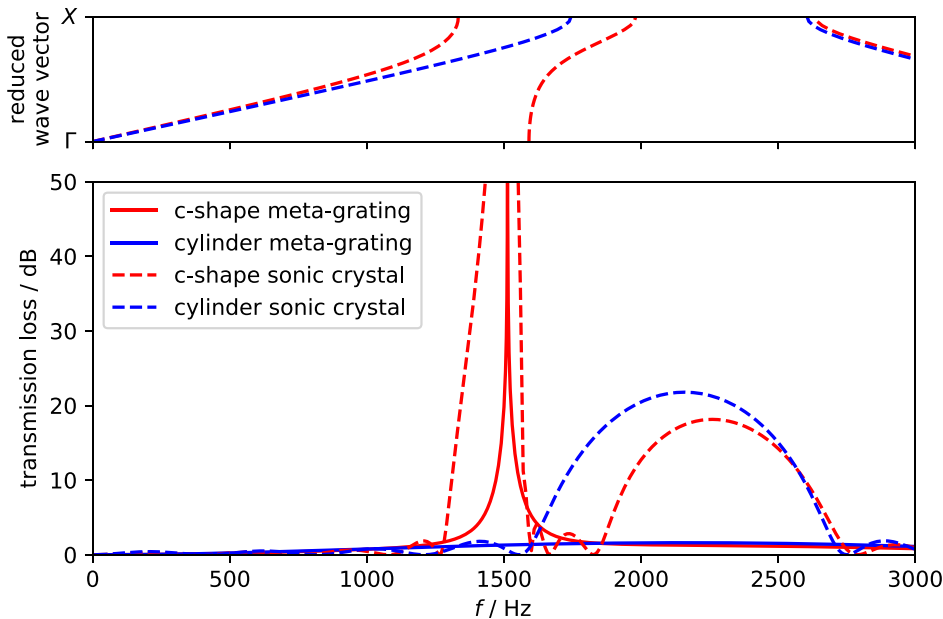


FIG. 11. (Color online) Dispersion relation for c-shape and cylinder sonic crystals and comparison of transmission loss for four different cases: c-shape meta-grating, cylinder meta-grating, c-shape sonic crystal with five unit cells, and cylinder sonic crystal with five unit cells.

(dashed curves), where the first band gap of the c-shape sonic crystal causes large transmission loss. Comparing that with the c-shape meta-grating reveals that the sonic crystal reflects the sound over a broader frequency range. However, the price for better performance is a thickness of five unit cells being $(5 + 4)2a$, which equals approximately 1.5λ at 1500 Hz. The increased thickness makes the sonic crystal less attractive for applications which have limited space, including stage machinery.

We note that the designed meta-gratings are ultra-sparse, having a thickness much smaller than the wavelength at the frequency of the maximum transmission loss. The meta-grating designed for the meta-capsule prototype with $a = 19$ mm is 0.17λ , while the meta-grating designed for the rope drive system with $a = 42.5$ mm reaches 0.15λ . The latter value is similar to the factor achieved by Cheng *et al.*²⁴ and demonstrates the effectiveness of the c-shape meta-atom. Furthermore, we observe in Fig. 11 that the sonic crystal of cylinders reveals a transmission loss up to 20 dB in the band gap, whereas the meta-grating of cylinders is not able to provide any noticeable transmission loss in the considered frequency range. This indicates that the transmission loss of the c-shape meta-grating is primarily due to local resonances of each meta-atom, rather than Bragg reflection between multiple meta-atoms.

VI. CONCLUSION

In this study, we investigated the reduction of noise emission from stage machinery using c-shape meta-atoms, with simple geometry that facilitates relatively easy manufacturing. We designed a 2D meta-grating and expanded it to a 3D meta-capsule prototype, which we investigated experimentally and numerically. In both experiment and simulation, a significant transmission drop at the resonant frequency of the meta-grating was observed. Furthermore, additional attenuation was present over a broad frequency range around the operating frequency, in addition to the narrow band attenuation of the meta-grating. Subsequently, this concept was verified by designing and manufacturing a meta-capsule for a rope drive system common in stage machinery. A transmission loss peak at resonant frequency could be observed experimentally. Additionally, it was numerically proven that the meta-capsule provides sufficient ventilation for cooling of the motor by natural convection. Finally, we modelled the noise of three other drive train types typically used in stage machinery, where a violation of stage machinery noise limits in the first row of the auditorium was present. Identification of critical peaks and subsequent design of tailored meta-gratings was demonstrated to reduce the noise emission. Following this, the presented concept provides a new horizon for noise control in stage machinery and other noise sensitive branches. This work demonstrates benefits and limitations of acoustic meta-capsules for noise control applications. To an engineer, it offers a simple concept for using acoustic meta-materials in daily work.

ACKNOWLEDGMENTS

A.M., M.M., N.F., M.S., and S.M. acknowledge funding supported by the German Federal Ministry for Economic Affairs and Energy under the index ZF4128201AT5. The authors acknowledge Yan Kei Chiang from UNSW Canberra for useful discussions on impedance modelling.

- ¹L. L. Beranek, "Revised criteria for noise in buildings," *Noise Control* **3**(1), 19–27 (1957).
- ²H.-P. Tennhardt, "Grenzwerte der schallimmission buhmentechnischer anlagen" ["Limits for noise immission of stage machinery installations"], *IEMB Infoblaetter* **5**, 1–4 (1998).
- ³A. Melnikov, I. Witew, M. Maeder, M. Gatt, M. Scheffler, and S. Marburg, "Sound pressure level limits for stage machinery noise in operas and theaters," *Appl. Acoust.* **156**, 29–39 (2019).
- ⁴A. Melnikov, M. Scheffler, and S. Marburg, "Untersuchungen eines Bühnenpodiums hinsichtlich der Reduktion von Geräuschemission" ["Investigations of a stage elevator concerning noise reduction"], *Proceedings of DAGA2017 Kiel* (2017).
- ⁵R. Müller, "Schwingungs- und Geräuschanregung bei Stirnradgetrieben" ["Vibration and noise of spur gears"] (1991).
- ⁶J. Zhou and S. Wenlei, "Vibration and noise radiation characteristics of gear transmission system," *J. Low Freq. Noise Vib. Active Control* **33**(4), 485–502 (2014).
- ⁷IEC 60034-1:2010: "Rotating electrical machines—Part 1: Rating and performance" (2010).
- ⁸S. A. Cummer, J. Christensen, and A. Alù, "Controlling sound with acoustic metamaterials," *Nat. Rev. Mater.* **1**(3), 16001 (2016).
- ⁹N. Fang, D. Xi, J. Xu, M. Ambati, W. Sritravanich, C. Sun, and X. Zhang, "Ultrasonic metamaterials with negative modulus," *Nat. Mater.* **5**(6), 452–456 (2006).
- ¹⁰Z. Liu, X. Zhang, Y. Mao, Y. Y. Zhu, Z. Yang, C. T. Chan, and P. Sheng, "Locally resonant sonic materials," *Science* **289**(5485), 1734–1736 (2000).
- ¹¹M. Ambati, N. Fang, C. Sun, and X. Zhang, "Surface resonant states and superlensing in acoustic metamaterials," *Phys. Rev. B* **75**(19), 195447 (2007).
- ¹²S. Zhang, L. Yin, and N. Fang, "Focusing ultrasound with an acoustic metamaterial network," *Phys. Rev. Lett.* **102**(19), 194301 (2009).
- ¹³D. Torrent and J. Sánchez-Dehesa, "Acoustic metamaterials for new two-dimensional sonic devices," *New J. Phys.* **9**(9), 323 (2007).
- ¹⁴J. V. Sánchez-Pérez, D. Caballero, R. Martínez-Sala, C. Rubio, J. Sánchez-Dehesa, F. Meseguer, J. Llinares, and F. Gálvez, "Sound attenuation by a two-dimensional array of rigid cylinders," *Phys. Rev. Lett.* **80**(24), 5325–5328 (1998).
- ¹⁵D. P. Elnford, L. Chalmers, F. V. Kusmartsev, and G. M. Swallowe, "Matryoshka locally resonant sonic crystal," *J. Acoust. Soc. Am.* **130**(5), 2746–2755 (2011).
- ¹⁶F. Langfeldt, W. Gleine, and O. von Estorff, "Analytical model for low-frequency transmission loss calculation of membranes loaded with arbitrarily shaped masses," *J. Sound Vib.* **349**, 315–329 (2015).
- ¹⁷S. M. B. Fard, H. Peters, S. Marburg, and N. Kessissoglou, "Acoustic performance of a barrier embedded with Helmholtz resonators using a quasi-periodic boundary element technique" (2017).
- ¹⁸J. Henneberg, A. Gerlach, H. Storck, H. Cebulla, and S. Marburg, "Reducing mechanical cross-coupling in phased array transducers using stop band material as backing," *J. Sound Vib.* **424**, 352–364 (2018).
- ¹⁹J. Henneberg, A. Gerlach, H. Cebulla, and S. Marburg, "The potential of stop band material in multi-frequency ultrasonic transducers," *J. Sound Vib.* **452**, 132–146 (2019).
- ²⁰C. Claeys, E. Deckers, B. Pluymers, and W. Desmet, "A lightweight vibro-acoustic metamaterial demonstrator: Numerical and experimental investigation," *Mech. Syst. Sign. Process.* **70-71**, 853–880 (2016).
- ²¹P. Marinova, S. Lippert, and O. von Estorff, "On the numerical investigation of sound transmission through double-walled structures with membrane-type acoustic metamaterials," *J. Acoust. Soc. Am.* **142**(4), 2400–2406 (2017).



- ²²G. Ma, M. Yang, Z. Yang, and P. Sheng, “Low-frequency narrow-band acoustic filter with large orifice,” *Appl. Phys. Lett.* **103**(1), 011903 (2013).
- ²³F. Langfeldt, H. Kemsies, W. Gleine, and O. von Estorff, “Perforated membrane-type acoustic metamaterials,” *Phys. Lett. A* **381**(16), 1457–1462 (2017).
- ²⁴Y. Cheng, C. Zhou, B. G. Yuan, D. J. Wu, Q. Wei, and X. J. Liu, “Ultra-sparse metasurface for high reflection of low-frequency sound based on artificial MIE resonances,” *Nat. Mater.* **14**(10), 1013–1019 (2015).
- ²⁵Z. Chen, L. Fan, S.-y. Zhang, H. Zhang, X.-j. Li, and J. Ding, “An open-structure sound insulator against low-frequency and wide-band acoustic waves,” *Appl. Phys. Exp.* **8**(10), 107301 (2015).
- ²⁶H.-I. Zhang, Y.-f. Zhu, B. Liang, J. Yang, J. Yang, and J.-c. Cheng, “Omnidirectional ventilated acoustic barrier,” *Appl. Phys. Lett.* **111**(20), 203502 (2017).
- ²⁷R. Ghaffarivardavagh, J. Nikolajczyk, S. Anderson, and X. Zhang, “Ultra-open acoustic metamaterial silencer based on Fano-like interference,” *Phys. Rev. B* **99**(2), 024302 (2019).
- ²⁸X. Yu, Z. Lu, T. Liu, L. Cheng, J. Zhu, and F. Cui, “Sound transmission through a periodic acoustic metamaterial grating,” *J. Sound Vib.* **449**, 140–156 (2019).
- ²⁹C. Shen, Y. Xie, J. Li, S. A. Cummer, and Y. Jing, “Acoustic metacages for sound shielding with steady air flow,” *J. Appl. Phys.* **123**(12), 124501 (2018).
- ³⁰X. Wu, C. Fu, X. Li, Y. Meng, Y. Gao, J. Tian, L. Wang, Y. Huang, Z. Yang, and W. Wen, “Low-frequency tunable acoustic absorber based on split tube resonators,” *Appl. Phys. Lett.* **109**(4), 043501 (2016).
- ³¹X. Wu, K. Y. Au-Yeung, X. Li, R. C. Roberts, J. Tian, C. Hu, Y. Huang, S. Wang, Z. Yang, and W. Wen, “High-efficiency ventilated metamaterial absorber at low frequency,” *Appl. Phys. Lett.* **112**(10), 103505 (2018).
- ³²T. Lee, T. Nomura, E. M. Dede, and H. Iizuka, “Ultrasparse acoustic absorbers enabling fluid flow and visible-light controls,” *Phys. Rev. Appl.* **11**(2), 024022 (2019).
- ³³X. Xiang, X. Wu, X. Li, P. Wu, H. He, Q. Mu, S. Wang, Y. Huang, and W. Wen, “Ultra-open high-efficiency ventilated metamaterial absorbers with customized broadband performance,” arXiv:1911.05969 (2019).
- ³⁴S.-H. Kim and S.-H. Lee, “Air transparent soundproof window,” *AIP Adv.* **4**(11), 117123 (2019).
- ³⁵Y. Ge, H.-x. Sun, S.-q. Yuan, and Y. Lai, “Switchable omnidirectional acoustic insulation through open window structures with ultrathin metasurfaces,” *Phys. Rev. Mater.* **3**(6), 065203 (2019).
- ³⁶L. L. Beranek, “Balanced noisecriterion (NCB) curves,” *J. Acoust. Soc. Am.* **86**(2), 650–664 (1989).
- ³⁷A. Melnikov, Y. K. Chiang, L. Quan, S. Oberst, A. Alù, S. Marburg, and D. Powell, “Acoustic meta-atom with experimentally verified maximum Willis coupling,” *Nat. Commun.* **10**(1), 3148 (2019).
- ³⁸J. R. Willis, “Effective constitutive relations for waves in composites and metamaterials,” *Proc. R. Soc. London A: Math. Phys. Eng. Sci.* **467**(2131), 1865–1879 (2011).
- ³⁹L. Quan, Y. Radi, D. L. Sounas, and A. Alù, “Maximum Willis coupling in acoustic scatterers,” *Phys. Rev. Lett.* **120**(25), 254301 (2018).
- ⁴⁰ANSYS *Multiphysics*, Release 19.2, Help System, ANSYS Inc., www.ansys.com (Last viewed 02/29/2020).
- ⁴¹S. Marburg and S. Schneider, “Influence of element types on numeric error for acoustic boundary elements,” *J. Comput. Acoust.* **11**(3), 363–386 (2003).
- ⁴²S. Marburg, “The Burton and Miller method: Unlocking another mystery of its coupling parameter,” *J. Comput. Acoust.* **24**(1), 1550016 (2015).
- ⁴³S. Marburg, *Boundary Element Method for Time-Harmonic Acoustic Problems* (Springer, Cham, 2018).
- ⁴⁴K. H. Drexhage, “Influence of a dielectric interface on fluorescence decay time,” *J. Lumin.* **1-2**, 693–701 (1970).
- ⁴⁵L. Langguth, R. Fleury, A. Alù, and A. F. Koenderink, “Drexhage’s experiment for sound,” *Phys. Rev. Lett.* **116**(22), 224301 (2016).
- ⁴⁶M. Landi, J. Zhao, W. E. Prather, Y. Wu, and L. Zhang, “Acoustic Purcell effect for enhanced emission,” *Phys. Rev. Lett.* **120**(11), 114301 (2018).
- ⁴⁷P. M. Morse and K. U. Ingard, *Theoretical Acoustics* (Princeton University Press, Princeton, 1968).
- ⁴⁸L. E. Kinsler, *Fundamentals of Acoustics* (Wiley, New York, 2000).
- ⁴⁹“Cellofoam 471 data sheet,” https://www.cellofoam.co.uk/fileadmin/user_upload/Data_sheets_English/471_E.pdf (Last viewed 02/29/2020).
- ⁵⁰K. T. Chen, Y. H. Chen, K. Y. Lin, and C. C. Weng, “The improvement on the transmission loss of a duct by adding Helmholtz resonators,” *Appl. Acoust.* **54**(1), 71–82 (1998).
- ⁵¹R. Harris, “The drama of the silent move: Control of noise from stage machinery in the Operaen Copenhagen,” *Proc. Inst. Acoust.* **27**(2), 28–35 (2005).
- ⁵²DIN 56950-1:2012-05, “Entertainment technology—Machinery installations—Part 1: Safety requirements and inspections” (2012).
- ⁵³D. C. Wilcox, “Reassessment of the scale-determining equation for advanced turbulence models,” *AIAA J.* **26**(11), 1299–1310 (1988).
- ⁵⁴F. R. Menter, “Two-equation eddy-viscosity turbulence models for engineering applications,” *AIAA J.* **32**(8), 1598–1605 (1994).
- ⁵⁵V. Adams and A. Askenazi, *Building Better Products with Finite Element Analysis* (OnWord Press, Florence, KY, 1999).
- ⁵⁶G. H. Koopmann and J. B. Fahnlne, *Designing Quiet Structures: A Sound Power Minimization Approach* (Elsevier, Amsterdam, 1997).
- ⁵⁷S. Marburg and B. Nolte, *Computational Acoustics of Noise Propagation in Fluids—Finite and Boundary Element Methods* (Springer-Verlag, Berlin, 2008).
- ⁵⁸J. B. Fahnlne and G. H. Koopmann, “A lumped parameter model for the acoustic power output from a vibrating structure,” *J. Acoust. Soc. Am.* **100**(6), 3539–3547 (1996).
- ⁵⁹D. Fritze, S. Marburg, and H.-J. Hardtke, “Estimation of radiated sound power: A case study on common approximation methods,” *Acta Acust. Acust.* **95**(5), 833–842 (2009).
- ⁶⁰M. Klaerner, M. Wuehrl, L. Kroll, and S. Marburg, “Accuracy of vibro-acoustic computations using non-equidistant frequency spacing,” *Appl. Acoust.* **145**, 60–68 (2019).
- ⁶¹COMSOL *Multiphysics*, v. 5.4, COMSOL AB, www.comsol.com (Last viewed 02/29/2020).

ARTICLE

<https://doi.org/10.1038/s41467-019-10915-5>

OPEN

Acoustic meta-atom with experimentally verified maximum Willis coupling

Anton Melnikov ^{1,2,3,4}, Yan Kei Chiang⁴, Li Quan⁵, Sebastian Oberst ³, Andrea Alù ^{5,6}, Steffen Marburg¹ & David Powell⁴

Acoustic metamaterials are structures with exotic acoustic properties, with promising applications in acoustic beam steering, focusing, impedance matching, absorption and isolation. Recent work has shown that the efficiency of many acoustic metamaterials can be enhanced by controlling an additional parameter known as Willis coupling, which is analogous to bianisotropy in electromagnetic metamaterials. The magnitude of Willis coupling in a passive acoustic meta-atom has been shown theoretically to have an upper limit, however the feasibility of reaching this limit has not been experimentally investigated. Here we introduce a meta-atom with Willis coupling which closely approaches this theoretical limit, that is much simpler and less prone to thermo-viscous losses than previously reported structures. We perform two-dimensional experiments to measure the strong Willis coupling, supported by numerical calculations. Our meta-atom geometry is readily modeled analytically, enabling the strength of Willis coupling and its peak frequency to be easily controlled.

¹Vibroacoustics of Vehicles and Machines, Technical University of Munich, Garching b. Munich 85748, Germany. ²SBS Bühnentechnik GmbH, Dresden 01259, Germany. ³Centre for Audio, Acoustics and Vibration University of Technology Sydney, Sydney, NSW 2007, Australia. ⁴School of Engineering and Information Technology, University of New South Wales, Canberra, ACT 2612, Australia. ⁵Department of Electrical and Computer Engineering, The University of Texas at Austin, Austin, TX 78712, USA. ⁶Photonics Initiative, Advanced Science Research Center City University of New York, New York, NY 10031, USA. Correspondence and requests for materials should be addressed to A.M. (email: anton.melnikov@tum.de) or to D.P. (email: david.powell@adfa.edu.au)

Acoustic metamaterials^{1,2} have demonstrated unique material properties which do not exist naturally, such as negative bulk modulus³ and negative dynamic mass density⁴. These properties have enabled the development of acoustic superlenses^{5–7}, barriers⁸, cloaking devices⁹, and the enhancement of non-linear effects¹⁰. Metamaterials are typically arrays of sub-wavelength structures, known as meta-atoms, with geometry engineered to control their dynamic mass and stiffness. It has recently been shown that more efficient metamaterial designs can be created by incorporating an additional degree of freedom, represented by the Willis coupling parameter.

Willis coupling is a term in the acoustic and elastic constitutive relations that couples potential and kinetic energy^{11–13}, analogous to the bianisotropy parameter in electromagnetism^{14,15}. The Willis coupling and bianisotropy parameters can only be non-zero in structures with low symmetry¹⁶, for example, in one dimension a structure lacking mirror symmetry in the propagation direction is required¹⁷. The inclusion of these terms into the constitutive relations has been shown to resolve violations of causality and passivity in metamaterial homogenization^{18,19}. Recent work has demonstrated that the incorporation of Willis coupling or bianisotropy into metamaterial structures of sub-wavelength thickness, known as metasurfaces, can improve their efficiency when refracting at large angles^{20–22}. While bianisotropy has been demonstrated and engineered in a wide range of electromagnetic meta-atom designs²³, approaches for controlling the degree of Willis coupling in acoustic meta-atoms are not well-established.

Recently, a bound on the maximum value of the Willis coupling parameter was derived, based on the conservation of energy²¹. It was shown how meta-atoms can be designed to reach this theoretical bound, using space-coiling structures with long meander-line channels^{21,24–26}. While such structures are advantageous for achieving resonance in a sub-wavelength volume, they are difficult to manufacture reproducibly, typically requiring additive manufacturing techniques. Moreover, their channel widths are often comparable to the viscous and thermal boundary layer thickness, and their channel lengths are of the order of the wavelength, leading to high thermo-viscous losses, and a significant reduction in scattering efficiency^{27–29}. It was shown numerically in ref. ²¹ that the thermo-viscous losses in space-coiling meta-atoms can reduce their Willis coupling magnitude to be significantly lower than the theoretical bound.

Experimental evidence of Willis coupling has been reported in both one-dimensional^{2,17} and two-dimensional metamaterial structures²⁰. It has also been shown how the effective medium properties of a bulk metamaterial incorporating Willis coupling can be derived from the polarizability of individual acoustic meta-atoms³⁰. However, the theoretical limit on the strength of Willis

coupling has not been tested experimentally, and it remains unknown how closely this limit may be approached in practice. To resolve this question we propose an acoustic meta-atom, which is designed to realize maximum Willis coupling and to minimize thermo-viscous losses. Experimental results obtained from a fabricated sample are compared to numerical calculations, showing good agreement of the resonant frequency and line-shape, with a reduction in magnitude that we attribute primarily to the energy leakage through the top and bottom waveguide plates, which are not perfectly hard. The simplicity of the structure enables us to present an analytical model for its polarizability, showing how the Willis coupling can be tailored to have any value between zero and the theoretical bound.

Results

Meta-atom design. Acoustic wave interaction with a meta-atom is conveniently described by its polarizability tensor. Due to the sub-wavelength size of meta-atoms, their scattering is dominated by monopole and dipole moments, and their polarizability can be written as

$$\begin{bmatrix} M \\ \mathbf{D} \end{bmatrix} = \boldsymbol{\alpha} \begin{bmatrix} \check{p}^{\text{inc}} \\ \check{\mathbf{v}}^{\text{inc}} \end{bmatrix} = \begin{bmatrix} \alpha^{pp} & \alpha^{pv} \\ \alpha^{vp} & \alpha^{vv} \end{bmatrix} \begin{bmatrix} \check{p}^{\text{inc}} \\ \check{\mathbf{v}}^{\text{inc}} \end{bmatrix}, \quad (1)$$

where M is the scalar monopole moment, \mathbf{D} is the vector dipole moment, $\boldsymbol{\alpha}$ is the polarizability tensor, \check{p}^{inc} and $\check{\mathbf{v}}^{\text{inc}}$ are the incident pressure and the velocity at the center of the meta-atom²¹. The off-diagonal terms α^{pv} and α^{vp} represent the Willis coupling between the dipolar and monopolar responses.

We show how the reported structures exhibiting Willis coupling^{2,17,21} can be replaced by a simpler, and more reproducible structure, by avoiding thin channels and large areas of fluid-structure interfaces. The structure can be tuned to achieve any value of Willis coupling up to the theoretical bounds and can be readily analyzed using a closed form analytical solution which assists in understanding the physical mechanisms behind its operation.

Achieving a strong acoustic polarizability in a small volume requires a resonant structure. Inspired by resonant sonic crystals⁸ and Helmholtz resonators with multiple apertures^{31–33}, our novel meta-atom design is presented in Fig. 1. This meta-atom exhibits Willis coupling due to the asymmetrical neck openings. The air within each neck is treated as an incompressible mass, while the air in the cavity acts as a spring, together creating an oscillating system excited by an incident acoustic wave. As the oscillation occurs in the fluid domain only, this avoids wave coupling through fluid-structure interfaces. Since the structure avoids long and thin channels, thermo-viscous losses are expected to be greatly reduced.

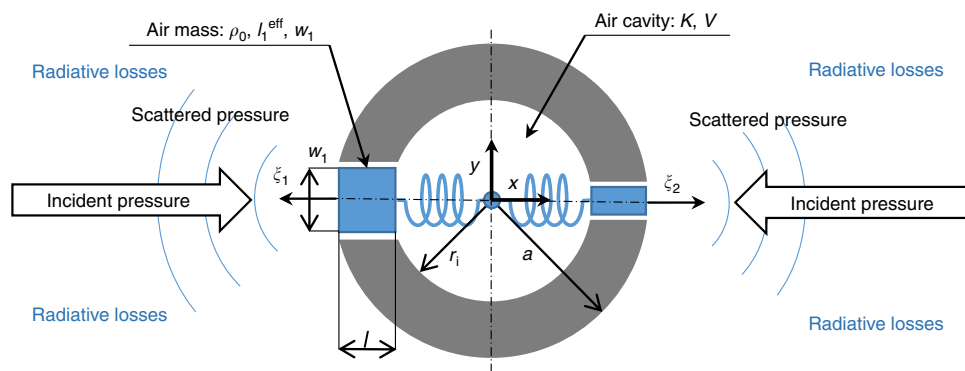


Fig. 1 Meta-atom geometry and dimensions. Here a is the cylinder radius and r_i is the cavity radius. The neck widths w_n are in general different for each aperture, the neck length l is common to all apertures and the cavity volume $V = \pi r_i^2$

Peak Willis coupling is expected to occur close to the Helmholtz resonator’s eigenfrequency, which is dependent on the air mass moving within the apertures and the inner cavity volume. In two dimensions (2D), the moving mass is determined by the aperture cross-sections $A_n = w_n$ and the neck length l , which is equal for all apertures due to the inner and outer cylindrical boundaries being concentric. The 2D-volume $V = \pi r_i^2$ is determined by the inner radius $r_i = a - l$, where a is the outer radius. By neglecting radiation damping, the eigenfrequency for N apertures can be approximated as (see Supplementary Note 3)

$$\omega_0 = \frac{c}{r_i} \sqrt{\frac{\sum_{n=1}^N w_n}{\pi l}} \quad (2)$$

A more accurate model including radiation damping is developed subsequently in this work. Generally, an arbitrary number of apertures may be included. However, for controlling Willis coupling along one axis, two oppositely arranged apertures are sufficient, as illustrated in Fig. 1. The apertures can be used to adjust the resonant frequency and the level of Willis coupling. The maximum Willis coupling magnitude is exhibited when the structure is shown in Fig. 1 becomes maximally asymmetric, consistent with the single aperture meta-atoms shown in ref. 21.

Experimental verification. To experimentally demonstrate Willis coupling in the presented meta-atom, its polarizability is determined in a 2D experiment. A single aperture meta-atom having maximum asymmetry is manufactured and investigated with the dimensions $a = 20$ mm, $r_i = 10$ mm, and $w = 12$ mm (see Fig. 2a). The incident and scattered pressure fields are measured in a 2D parallel-plate waveguide²⁹ (see Fig. 2b) with subsequent extraction of the polarizability tensor as detailed in Supplementary Note 5.

The polarizability tensor defined in Eq. (1) has elements with different units and values differing by many orders of magnitude. Therefore it is convenient to introduce the normalized polarizability tensor α' , the elements of which are shown for our meta-

atom structure in Fig. 2d–g. The normalized values are defined as $\alpha'_{pp} = -2\alpha^{pp}$, $\alpha'_{pv} = \frac{-\sqrt{2}}{\rho c} \alpha^{pv}$, $\alpha'_{vp} = ik\sqrt{2}\alpha^{vp}$, and $\alpha'_{vv} = \frac{ik}{\rho c} \alpha^{vv}$ ²¹. As required by reciprocity²¹, the tensor satisfies $\alpha' = \alpha'^T$, since the off-diagonal terms are equal to each other with a sign reversal (see Fig. 2e, f). The error bars in Fig. 2d–g show the standard deviation of the experimentally extracted polarizability terms, obtained from the least squares fit (see Methods section). To verify that the magnitude of Willis coupling is close to the theoretical maximum, Fig. 3 shows the numerically and analytically calculated $|\alpha'_{pv}|$ and the experimentally determined $|\alpha'_{pv}|$ and $|\alpha'_{vp}|$. For the numerical analysis, the 2D Boundary Element Method (BEM) has been applied. Here, the peak Willis coupling at $k \cdot a = 0.75$ achieves 90% of the theoretical bound $4\omega^{-2}$.

Polarizability theory. To show how the Willis coupling and other polarizability components can be tailored by adjusting the meta-atom geometry, we develop a polarizability theory. The predictions of this theory are shown in Figs. 2 and 3. It is based on multiple aperture Helmholtz resonator dynamics for the outward directed particle displacement ξ_n within each aperture (see Supplementary Note 3)

$$i\omega^3 c_n^{\text{rad}} \frac{\rho_0 A_n}{c} \xi_n + \omega^2 \rho_0 l_n^{\text{eff}} \xi_n - \frac{K}{V} \sum_m A_m \xi_m = p_n^{\text{ext}} \quad (3)$$

Here p_n^{ext} is the external pressure at aperture n , ρ_0 is the medium density, c is the speed of sound, $A_n = w_n$ is the cross-section of the aperture, $K = c^2 \rho_0$ is the bulk modulus, V is the inner cavity volume, $l_n^{\text{eff}} = l + c_n^{\text{eff}}$ is the effective neck length (including a radiative correction) and c_n^{rad} is the radiative loss coefficient (see Fig. 1). The ω^3 -term corresponds to radiative losses, the ω^2 -term represents Newton’s second law applied to the air in the neck, and the summation over m accounts for coupling between apertures via compression of the center cavity using Hooke’s law. Considering all apertures results in a matrix

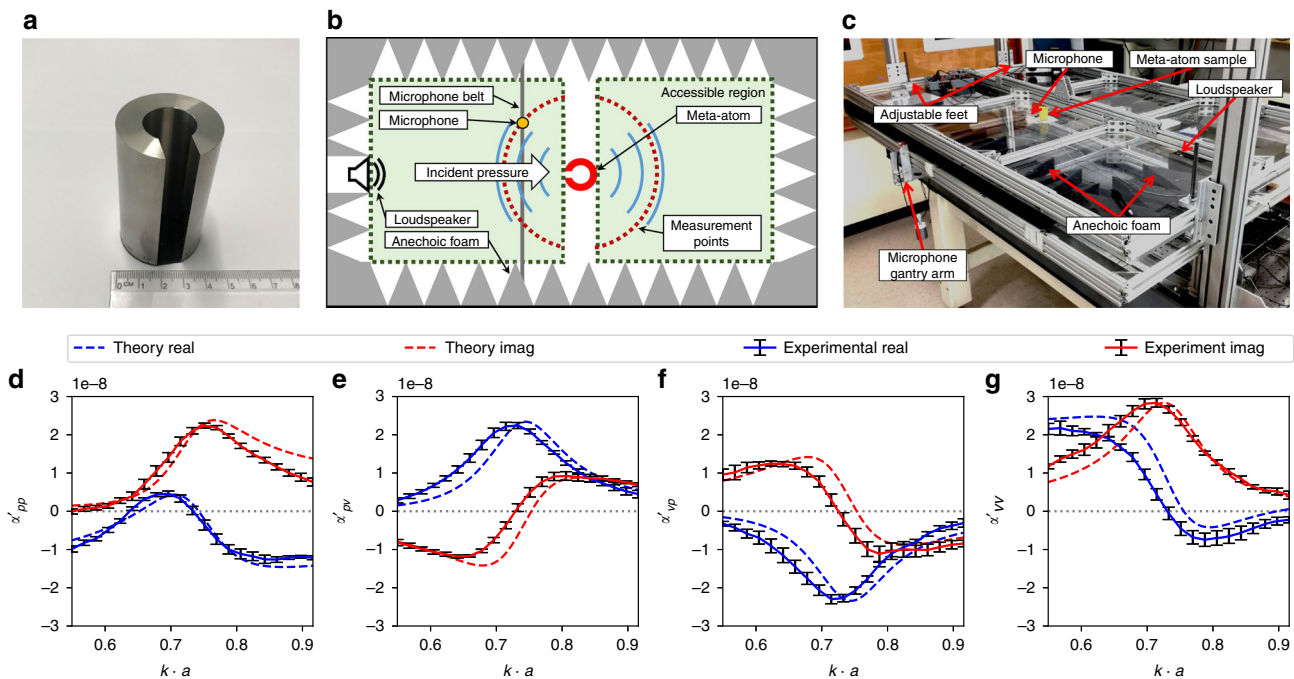


Fig. 2 Experimental system and results. **a** Stainless steel sample: single aperture meta-atom with $a = 20$ mm, $r_i = 10$ mm, $w = 12$ mm, and $h = 66$ mm. **b, c** Schematic and photograph of the experimental set-up. **d–g** Theoretically predicted and experimentally determined components of the normalized polarizability tensor. The error bars show the standard deviation resulting from the least squares fit over 12 incident angles

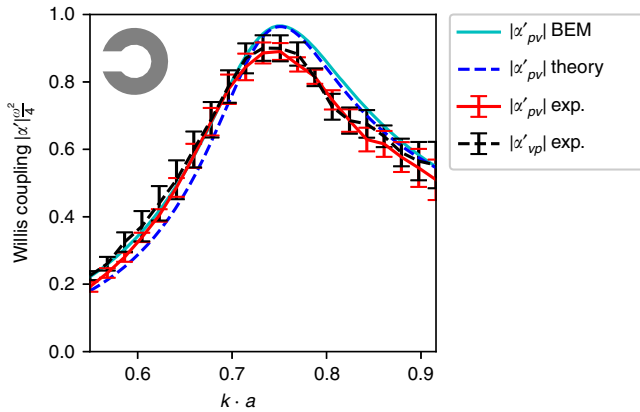


Fig. 3 Willis coupling magnitude. Result for a single aperture meta-atom obtained from BEM simulation (cyan solid line), polarizability theory (blue dashed line) and experimentally (red solid and black dashed lines), normalized to the theoretical bound $4\omega^{-2}$

equation $\mathbf{K}_{\text{eq}}\boldsymbol{\xi} = \mathbf{p}^{\text{ext}}$, where \mathbf{K}_{eq} is the dynamic stiffness matrix given by Supplementary Equation (38). This matrix allows the displacement to be solved for an arbitrary incident pressure field and hence, the contribution of the oscillating air masses (see Fig. 1) to the scattering of the meta-atom. See Supplementary Note 3 for full details of the derivation.

We consider now the shape illustrated in Fig. 1. This restricts the Willis coupling to a single axis and simplifies the problem to a 2×2 matrix. In this case, the resonator polarizability tensor $\boldsymbol{\alpha}^{\text{res}}$ is obtained as

$$\boldsymbol{\alpha}^{\text{res}} = \rho_0 \begin{bmatrix} A_1 & A_2 \\ x_1 A_1 & x_2 A_2 \end{bmatrix} \mathbf{K}_{\text{eq}}^{-1} \begin{bmatrix} 1 & -i a \rho_0 \omega \\ 1 & i a \rho_0 \omega \end{bmatrix}, \quad (4)$$

The ratio of aperture widths $\frac{w_1}{w_2} = \frac{A_1}{A_2}$ determines the strength of Willis coupling and can be used to optimize the structure. Expanding Eq. (4) for a single aperture meta-atom with $w_2 = 0$ leads to the following expression for the polarizability

$$\boldsymbol{\alpha}^{\text{res}} = \frac{\rho_0 \begin{bmatrix} A_1 & -i a \rho_0 \omega A_1 \\ x_1 A_1 & -i a \rho_0 \omega x_1 A_1 \end{bmatrix}}{i \omega^3 c^{\text{rad}} \frac{\rho_0 A_1}{\pi c} + \omega^2 \rho_0 I_1^{\text{eff}} - \frac{K}{V} A_1}. \quad (5)$$

The dynamic stiffness matrix becomes a scalar equation with the remaining projection matrix being singular. The singularity arises because both the monopole and dipole moments are determined from the air movement within a single aperture, but it presents no computational difficulties, since the inverse of the polarizability tensor is not required.

As the Helmholtz resonator is embedded within a cylinder (see Fig. 1), there is an additional influence on the meta-atom polarizability due to the background scattering from the cylinder. Considering only the dipole and monopole terms, the polarizability tensor of a cylinder of radius a is (see Supplementary Note 4)

$$\boldsymbol{\alpha}^{\text{cyl}} = \begin{bmatrix} \frac{4}{ik^2 c^2} \frac{J_1(ka)}{H_1^{(1)}(ka)} & 0 \\ 0 & \frac{8\rho_0}{k^3 c} \frac{J_1(ka)}{H_1^{(1)\prime}(ka)} \end{bmatrix}, \quad (6)$$

where J_n is a Bessel function, $H_n^{(1)}$ is a Hankel function of the first kind and $k = \omega/c$ is the wavenumber. As expected for a symmetrical geometry, the off-diagonal terms corresponding to Willis coupling are zero. Since the resonator and cylinder are superimposed, they influence the effective incident fields of each

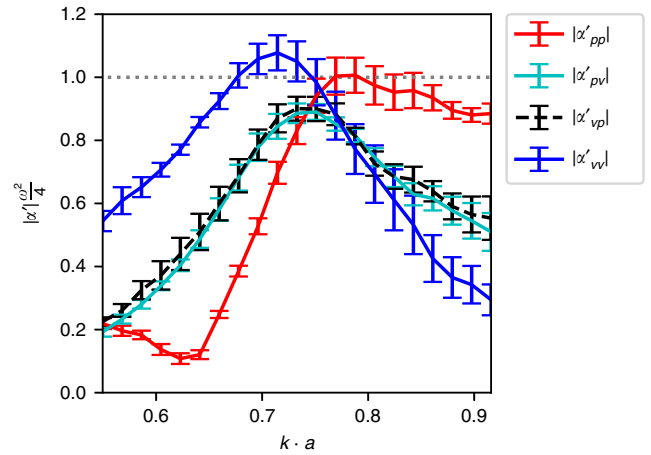


Fig. 4 Experimental polarizability. Amplitudes of experimentally determined polarizability components showing shared magnitude closely to $k \cdot a = 0.75$

other through an additional scattered term:

$$\begin{aligned} \check{p}_{\text{cyl}}^{\text{inc}} &= \check{p}^{\text{inc}} + \check{p}_{\text{res}}^{\text{scat}} \\ \check{p}_{\text{res}}^{\text{inc}} &= \check{p}^{\text{inc}} + \check{p}_{\text{cyl}}^{\text{scat}}. \end{aligned} \quad (7)$$

This results in a coupled formulation for the monopole and dipole moments of the cylinder and the Helmholtz resonator as

$$\begin{bmatrix} M^{\text{cyl}} \\ D^{\text{cyl}} \\ M^{\text{res}} \\ D^{\text{res}} \end{bmatrix} = \begin{bmatrix} \mathbf{I} & -\boldsymbol{\alpha}^{\text{cyl}} \mathbf{E} \\ -\boldsymbol{\alpha}^{\text{res}} \mathbf{E} & \mathbf{I} \end{bmatrix}^{-1} \begin{bmatrix} \boldsymbol{\alpha}^{\text{cyl}} \mathbf{u}^{\text{inc}} \\ \boldsymbol{\alpha}^{\text{res}} \mathbf{u}^{\text{inc}} \end{bmatrix}. \quad (8)$$

where $\mathbf{u}^{\text{inc}} = [\check{p}^{\text{inc}} \quad \check{v}_x^{\text{inc}}]^T$ is the incident field vector and $\mathbf{E} = \text{diag}\left(-\frac{ik^2 c^2}{4} H_0^{(1)}(ka), -\frac{k^2 c}{4a\rho_0} H_1^{(1)}(ka)\right)$ represents the acoustic propagation from the cylinder to each of the apertures. Finally, adding the monopole and dipole moments from Eq. (8) results in

$$\begin{bmatrix} M^{\text{tot}} \\ D^{\text{tot}} \end{bmatrix} = \begin{bmatrix} M^{\text{cyl}} + M^{\text{res}} \\ D^{\text{cyl}} + D^{\text{res}} \end{bmatrix} = \boldsymbol{\alpha}^{\text{tot}} \mathbf{u}^{\text{inc}}, \quad (9)$$

which gives the total polarizability tensor $\boldsymbol{\alpha}^{\text{tot}}$. The components of $\boldsymbol{\alpha}^{\text{tot}}$ for a single aperture meta-atom with $a = 20$ mm, $r_i = 10$ mm, $w = 12$ mm, $c = 343$ m \cdot s $^{-1}$, and $\rho_0 = 1.2$ kg \cdot m $^{-3}$ are shown together with the experimental results in Fig. 2.

Discussion

It has been shown based on passivity and reciprocity conditions²¹ that maximum Willis coupling can be achieved only if the polarizability components share the same magnitude and the meta-atom has no losses. Figure 4 shows the magnitude of the experimentally extracted polarizability components, where a crossing point can be observed at $k \cdot a = 0.75$. At this point the magnitudes are very close to each other, giving a precise indication of the frequency of maximum Willis coupling.

The lossless condition cannot be perfectly satisfied, since any fluid medium exhibits thermal and viscous losses, which are greatly magnified close to the boundaries. Furthermore, our two-dimensional parallel-plate waveguide shown in Fig. 2c will leak some energy through the top and bottom plates, since they can only approximate the perfectly hard boundary condition. Although these losses are not treated in our theory, Fig. 2d–g shows that the experimental line-shape and resonant frequency are well described by our theoretical model. To illustrate how closely our meta-atom approaches the theoretical bound, the

magnitude of the Willis coupling is plotted in Fig. 3. The slight frequency shift observable in Fig. 2d–g between the experimental and theoretical values can be attributed to the thermo-viscous losses of air. To investigate these mechanisms within the meta-atom, we model the thermo-viscous losses using the Finite Element Method (FEM), with the resulting Willis coupling shown in Fig. 5. The results reveal a downshifting of the frequency by 2.2% and show that thermo-viscous losses lead to a reduction of 0.32% in the magnitude of Willis coupling. We note that this reduction in magnitude is much less than that previously reported for space-coiling meta-atoms with thin channels, which was ~21% at $k \cdot a \approx 0.75$ (see Supplementary Material of ref. 21). In Fig. 5 we also plot the Willis coupling magnitude for the space-coiling meta-atom from ref. 21 where the much higher radiative quality factor of the space-coiling structure leads to higher internal dissipation, hence a much greater impact of thermo-viscous losses on the Willis coupling.

In addition to the experimentally demonstrated maximum Willis coupling, the structure presented in Fig. 1 can be tailored to have Willis coupling from zero up to the theoretical bound. To demonstrate this property, normalized Willis coupling for four different parameter sets is shown in Fig. 6. The red meta-atom on top illustrates the single aperture configuration similar to the experimentally investigated structure from Fig. 2a. Once a second aperture with neck width w_2 is introduced, Willis coupling is significantly reduced (Fig. 6 magenta and violet lines). This would

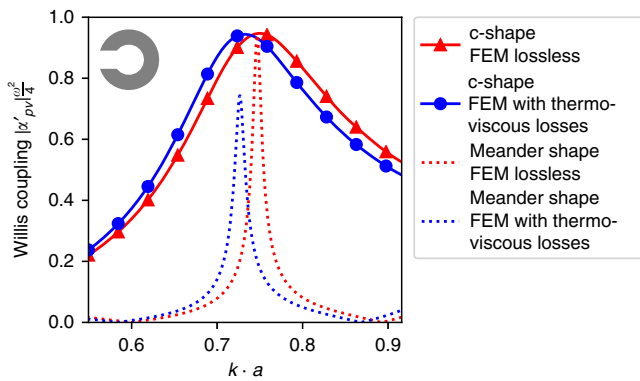


Fig. 5 Sensitivity to thermo-viscous losses. Numerical comparison of Willis coupling showing the influence of thermo-viscous losses in air, which cause a reduction in magnitude of only 0.32% for the c-shape meta-atom, whereas for the space-coiling structure reported in ref. 21 the magnitude drops by ~21%

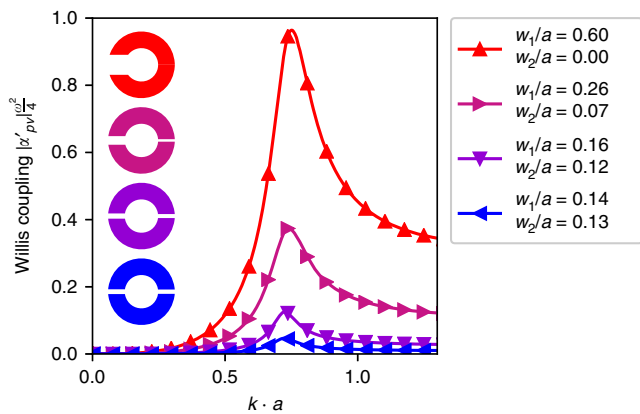


Fig. 6 Control of Willis coupling. Willis coupling of four different meta-atom geometries, where w_2 is varied to control Willis coupling and w_1 is tuned to keep the peak frequency fixed

result in a frequency shift, as expected from Eq. (2). To avoid this, w_1 is tuned to match the peak frequency of the single aperture case. When w_2 is further increased and the shape starts to converge to the symmetrical case (Fig. 6 blue, $\frac{w_1}{w_2} \approx 1.1$), the Willis coupling becomes very weak and disappears completely when $\frac{w_1}{w_2} = 1$. This behavior is of practical importance, since it allows tailoring of the Willis coupling to any desired values. A full parametric analysis of the influence of w_1 and w_2 on the resonant frequency and peak Willis coupling is presented in Supplementary Note 6.

In conclusion, we introduced and experimentally validated a novel meta-atom exhibiting strong Willis coupling and providing a low radiative Q factor. The experiment revealed a Willis coupling magnitude reaching ~90% of the theoretical bound. In this structure, thermo-viscous losses in air are quite small, whereas they are much stronger in previously reported space-coiling meta-atoms. Additionally, the simple shape of our structure facilitates manufacturing and enables accurate analytical modeling. Combining the models of a Helmholtz resonator and a cylindrical scatterer, a theory was developed and shown to agree well with numerical simulations. Since our structure enables Willis coupling to be tailored, this theory can be used to engineer Willis coupling for specific applications.

Methods

Extraction of polarizability tensor. The polarizability relationship given in Eq. (1) is used to illustrate Willis coupling, where it appears as the off-diagonal terms α^{pv} and α^{vp} . An extraction method is necessary to obtain the polarizability of a scatterer from an experiment or numerical model. For simplicity, only the 2D case is considered. We build on the method for extracting polarizability from highly symmetric 2D structures in ref. 29 which does not account for Willis coupling. This method makes use of the incident and scattered pressure fields around the object and fits Bessel and Hankel functions to them as $p_{\text{inc}}(r, \theta) = \sum_n \beta_n J_n(kr) e^{in\theta}$ and $p_{\text{scat}}(r, \theta) = \sum_n \gamma_n H_n^{(1)}(kr) e^{in\theta}$. Since only monopole and dipole components are of importance, the problem can be reduced to considering $n = -1, 0, 1$ terms. Following this, the incident pressure at the meta-atom center is $p^{\text{inc}} = \beta_0$ and the particle velocity $\check{v}_{x,y}^{\text{inc}} = \frac{\beta_1 \mp \beta_{-1}}{2\rho_0 c}$. The monopole moment $M = \frac{-4\gamma_0}{ik^2 c^2}$ and the dipole moments $D_{x,y} = \frac{-4(\gamma_1 \mp \gamma_{-1})}{ik^3 c^2}$ can be retrieved from the scattered field. For further information see Supplementary Note 1 and 2.

The expansion coefficients β_n and γ_n can be obtained from measured or numerically determined pressure on circles with radii R^{inc} and R^{scat} respectively. From the orthogonality of exponential functions, the coefficients can be found as

$$\beta_n = \frac{1}{2\pi J_n(kR^{\text{inc}})} \int_0^{2\pi} p^{\text{inc}}(R^{\text{inc}}, \theta) e^{-in\theta} d\theta \tag{10}$$

and

$$\gamma_n = \frac{1}{2\pi H_n^{(1)}(kR^{\text{scat}})} \int_0^{2\pi} p^{\text{scat}}(R^{\text{scat}}, \theta) e^{-in\theta} d\theta. \tag{11}$$

To avoid the singularity of Eq. (10) due to zeros of the Bessel function²⁹, we ensure $R^{\text{inc}} < \frac{2.4}{k}$. However, R^{scat} should be significantly larger than the meta-atom outer radius to reduce near field contributions. These conflicting requirements mean that R^{inc} and R^{scat} are different in general.

To fully determine the polarizability in 2D, \check{p}^{inc} , \check{v}^{inc} , M and D must be determined for at least 3 incident angles. The incident field quantities for all available angles $\theta_{1..m}$ are arranged in a matrix \mathbf{Y} as

$$\mathbf{Y} = \begin{bmatrix} \check{p}^{\text{inc}}(\theta_1) & \check{v}_x^{\text{inc}}(\theta_1) & \check{v}_y^{\text{inc}}(\theta_1) \\ \vdots & \vdots & \vdots \\ \check{p}^{\text{inc}}(\theta_m) & \check{v}_x^{\text{inc}}(\theta_m) & \check{v}_y^{\text{inc}}(\theta_m) \end{bmatrix} \tag{12}$$

Knowing M and D for each $\theta_{1..m}$, allows the polarizability tensor α to be determined by inversion of \mathbf{Y} . For increased robustness, we take additional angles. The polarizability tensor is then determined via least squares as

$$\alpha = (\mathbf{Y}^T \mathbf{Y})^{-1} \mathbf{Y}^T \begin{bmatrix} M(\theta_1) & D_x(\theta_1) & D_y(\theta_1) \\ \vdots & \vdots & \vdots \\ M(\theta_m) & D_x(\theta_m) & D_y(\theta_m) \end{bmatrix}. \tag{13}$$

Numerical model. To obtain a numerical solution for the polarizability a custom 2D BEM code is used, as described in ref.²⁹. It uses continuous elements with quadratic interpolation functions³⁴ and discretization by collocation method³⁵ with an adaptive integration scheme³⁶. Initially the solids are treated as acoustic hard boundaries. Thermo-viscous losses in air are not included in this formulation. The incident field is a unit intensity plane wave, therefore \vec{p}^{inc} and \vec{v}^{inc} are known explicitly. The medium density and the speed of sound are set to $\rho_0 = 1.2 \text{ kg} \cdot \text{m}^{-3}$ and $c = 343 \text{ m} \cdot \text{s}^{-1}$.

To calculate the influence of thermo-viscous losses in air on the polarizability of the meta-atom (Fig. 5) 2D FEM calculations are performed with the COMSOL Multiphysics Thermo-viscous Acoustics Module. The acoustic boundary of the meta-atom is treated as rigid. For the lossless case, the mechanical boundary condition of the structure is set to be slip and the thermal boundary is set to be adiabatic. Both the viscosity coefficient and the thermal conductivity coefficient are set as zero in the simulation. For the lossy case, the mechanical boundary is set to be no slip and the thermal boundary is set to be isothermal. The thermal and viscous coefficients used for air are $\rho_0 = 1.2043 \text{ kg} \cdot \text{m}^{-3}$, $c = 343.14 \text{ m} \cdot \text{s}^{-1}$, $\mu = 1.814 \times 10^{-5} \text{ Pa} \cdot \text{s}$, $\mu_B = 1.0884 \times 10^{-5} \text{ Pa} \cdot \text{s}$, $k = 0.025768 \text{ W} \cdot \text{m}^{-1} \cdot \text{K}^{-1}$, $C_p = 1005.4 \text{ J} \cdot \text{kg}^{-1} \cdot \text{K}^{-1}$, $\alpha_p = 0.0034112 \text{ K}^{-1}$, $\gamma = 1.4$ and $\beta_T = 9.8692 \times 10^{-6} \text{ Pa}^{-1}$. The finite element type is a triangular element with quadratic interpolation functions. The maximum element size is set to approximately 28 elements per wavelength at 2500 Hz.

Waveguide scattering experiment. To experimentally determine the incident and scattered pressure fields we use the 2D anechoic waveguide chamber presented in ref.²⁹. The propagation medium is air with an acoustic velocity of $343 \text{ m} \cdot \text{s}^{-1}$. The height of the chamber (66 mm) supports only a single propagation mode at frequencies up to 2600 Hz, making it a 2D wave propagation system. The excitation source is a speaker, excited by a continuous wave with frequency varying between 1500 Hz and 2500 Hz in 50 Hz steps. The response is measured by a microphone, which is moved in two axes by belts driven by stepper motors.

The sample is a single aperture meta-atom shown in Fig. 1a. This meta-atom was manufactured from stainless steel with precisely machined surface with maximum surface roughness of $4 \mu\text{m}$ (Rz4). Additionally, rubber seals (black) are glued on top and bottom to prevent air leakage from the resonator cavity and to achieve more homogeneous clamping. The incident field is measured at a radius $R^{\text{inc}} = 40 \text{ mm}$. The scattering of the sample is measured at 12 different incident angles ($0^\circ, 30^\circ, 60^\circ, 90^\circ, 120^\circ, 150^\circ, 180^\circ, 210^\circ, 240^\circ, 270^\circ, 300^\circ, 330^\circ$) at a radius of $R^{\text{scat}} = 200 \text{ mm}$

Data availability

All relevant data that support the findings of this study are available from the corresponding author upon request.

Received: 23 November 2018 Accepted: 6 June 2019

Published online: 17 July 2019

References

- Cummer, S. A., Christensen, J. & Alù, A. Controlling sound with acoustic metamaterials. *Nat. Rev. Mater.* **1**, 16001 (2016).
- Koo, S., Cho, C., Jeong, J.-h & Park, N. Acoustic omni meta-atom for decoupled access to all octants of a wave parameter space. *Nat. Commun.* **7**, 13012 (2016).
- Fang, N. et al. Ultrasonic metamaterials with negative modulus. *Nat. Mater.* **5**, 452–456 (2006).
- Liu, Z. et al. Locally resonant sonic materials. *Science* **289**, 1734–1736 (2000).
- M. Ambati, N. Fang, C. Sun & X. Zhang. Surface resonant states and superlensing in acoustic metamaterials. *Phys. Rev. B*, **75**, 195447 (2007).
- Zhang, S., Yin, L. & Fang, N. Focusing ultrasound with an acoustic metamaterial network. *Phys. Rev. Lett.* **102**, 194301 (2009).
- Torrent, D. & Sánchez-Dehesa, J. Acoustic metamaterials for new two-dimensional sonic devices. *New J. Phys.* **9**, 323 (2007).
- Elford, D. P., Chalmers, L., Kusmartsev, F. V. & Swallowe, G.M. Matryoshka locally resonant sonic crystal. *J. Acoust. Soc. Am.* **130**, 2746–2755 (2011).
- Zhang, S., Xia, C. & Fang, N. Broadband acoustic cloak for ultrasound waves. *Phys. Rev. Lett.* **106**, 024301 (2011).
- Quan, L., Liu, X. & Gong, X. Quasi-phase-matched backward second-harmonic generation by complementary media in nonlinear metamaterials. *J. Acoust. Soc. Am.* **132**, 2852–2856 (2012).
- Willis, J. R. Variational principles for dynamic problems for inhomogeneous elastic media. *Wave Motion* **3**, 1–11 (1981).
- Willis, J. R. The nonlocal influence of density variations in a composite. *Int. J. Solids Struct.* **21**, 805–817 (1985).
- Willis, J. R. Effective constitutive relations for waves in composites and metamaterials. *Proc. R. Soc. A* **467**, 1865–1879 (2011).
- Cheng, D. K. & Kong, J.-A. Covariant descriptions of bianisotropic media. *Proc. IEEE* **56**, 248–251 (1968).
- Kong, J. A. Theorems of bianisotropic media. *Proc. IEEE* **60**, 1036–1046 (1972).
- Serdyukov, A., Semchenko, I., Tretyakov, S. A. & Sihvola, A. *Electromagnetics of Bi-Anisotropic Materials: Theory and Applications*. (Gordon and Breach Science Publishers, Amsterdam, 2001).
- Muhlestein, M. B. et al. Experimental evidence of Willis coupling in a one-dimensional effective material element. *Nat. Commun.* **8**, 15625 (2017).
- Muhlestein, M. B., Sieck, C. F., Alù, A. & Haberman, M. R. Reciprocity, passivity and causality in Willis materials. *Proc. R. Soc. A* **472**, 20160604 (2016).
- Alù, A. Restoring the physical meaning of metamaterial constitutive parameters. *Phys. Rev. B* **83**, 081102 (2011).
- Li, J., Shen, C., Diaz-Rubio, A., Tretyakov, S. A. & Cummer, S. A. Systematic design and experimental demonstration of bianisotropic metasurfaces for scattering-free manipulation of acoustic wavefronts. *Nat. Commun.* **9**, 1342 (2018).
- L. Quan, Y. Ra'di, D. L. Sounas & A. Alù. Maximum Willis coupling in acoustic scatterers. *Phys. Rev. Lett.* **120**, 254301 (2018).
- Ra'di, Y., Sounas, D. L. & Alù, A. Metagratings: beyond the limits of graded metasurfaces for wave front control. *Phys. Rev. Lett.* **119**, 067404 (2017).
- Asadchy, V. S., Diaz-Rubio, A. & Tretyakov, S. A. Bianisotropic metasurfaces: physics and applications. *Nanophotonics* **7**, 1069–1094 (2018).
- Li, Y. et al. Acoustic focusing by coiling up space. *Appl. Phys. Lett.* **101**, 233508 (2012).
- Cheng, Y. et al. Ultra-sparse metasurface for high reflection of low-frequency sound based on artificial Mie resonances. *Nat. Mater.* **14**, 1013–1019 (2015).
- Lu, G. et al. Realization of acoustic wave directivity at low frequencies with a subwavelength Mie resonant structure. *Appl. Phys. Lett.* **110**, 123507 (2017).
- Attenborough, K. Acoustical characteristics of rigid fibrous absorbents and granular materials. *J. Acoust. Soc. Am.* **73**, 785–799 (1983).
- Stinson, M. R. The propagation of plane sound waves in narrow and wide circular tubes, and generalization to uniform tubes of arbitrary cross-sectional shape. *J. Acoust. Soc. Am.* **89**, 550–558 (1991).
- Jordaan, J. et al. Measuring monopole and dipole polarizability of acoustic meta-atoms. *Applied Physics Letters* **113**, 224102 (2018).
- Sieck, C. F., Alù, A. & Haberman, M. R. Origins of Willis coupling and acoustic bianisotropy in acoustic metamaterials through source-driven homogenization. *Physical Review B* **96**, 104303 (2017).
- Dosch, H. G. Radiative feedback in Helmholtz resonators with more than one opening. *J. Acoust. Soc. Am.* **140**, 3576–3581 (2016).
- Crow, B. C. et al. Experimental realization of extraordinary acoustic transmission using Helmholtz resonators. *AIP Adv.* **5**, 027114 (2015).
- Kinsler, L. E. *Fundamentals of Acoustics* (Wiley, 2000).
- Marburg S. & Nolte B. *Computational Acoustics of Noise Propagation in Fluids – Finite and Boundary Element Methods* (Springer-Verlag, 2008).
- T. W. Wu. *Boundary Element Acoustics: Fundamentals and Computer Codes* (WIT, 2000).
- Marburg, S. in *Computational Acoustics*, CISM International Centre for Mechanical Sciences. 69–158 (Springer, Cham, 2018).

Acknowledgements

A.M. acknowledges funding supported by German Federal Ministry for Economic Affairs and Energy under the index ZF4128201AT5. A.M. also acknowledges the financial support provided by S.O. through the UTS Centre for Audio, Acoustics and Vibration (CAAV) international visitor funds. D.P. acknowledges funding from the Australian Research Council through Discovery Project DP150103611. A.A. and L.Q. were supported by the National Science Foundation and the Simons Foundation. The authors acknowledge Murat Tahtali from UNSW Canberra for useful discussions on 3D printing and for manufacturing the 3D-printed initial prototype of the single aperture meta-atom.

Author contributions

A.M. and D.P. developed the analytical model, D.P. designed the experimental set-up; A.M. conceived the meta-atom structure, and designed the experimental sample, validated the results experimentally, numerically and analytically and wrote the paper. Y.K.C. designed the experimental sample and performed measurements to maximize the experimental performance. L.Q. performed the FEM calculations and supported the numerical and analytical study. S.M. and A.A. provided guidance on numerical and theoretical aspects of the study, respectively. A.M., S.O. and D.P. conceptualized the study. D.P. provided guidance on all aspects of the work. All authors contributed in editing the draft.

Additional information

Supplementary Information accompanies this paper at <https://doi.org/10.1038/s41467-019-10915-5>.

Competing interests: The authors declare no competing interests.

Reprints and permission information is available online at <http://npg.nature.com/reprintsandpermissions/>

Peer review information: *Nature Communications* thanks Namkyoo Park and the other anonymous reviewer(s) for their contribution to the peer review of this work. Peer reviewer reports are available.

Publisher's note: Springer Nature remains neutral with regard to jurisdictional claims in published maps and institutional affiliations.



Open Access This article is licensed under a Creative Commons Attribution 4.0 International License, which permits use, sharing, adaptation, distribution and reproduction in any medium or format, as long as you give appropriate credit to the original author(s) and the source, provide a link to the Creative Commons license, and indicate if changes were made. The images or other third party material in this article are included in the article's Creative Commons license, unless indicated otherwise in a credit line to the material. If material is not included in the article's Creative Commons license and your intended use is not permitted by statutory regulation or exceeds the permitted use, you will need to obtain permission directly from the copyright holder. To view a copy of this license, visit <http://creativecommons.org/licenses/by/4.0/>.

© The Author(s) 2019

**Acoustic meta-atom with experimentally verified
maximum Willis coupling
Supplementary Material**

Anton Melnikov,^{1,2,3,4,*} Yan Kei Chiang,⁴ Li Quan,⁵ Sebastian
Oberst,³ Andrea Alù,^{6,5} Steffen Marburg,¹ and David Powell^{4,†}

¹*Vibroacoustics of Vehicles and Machines
Technical University of Munich, Germany*

²*SBS Bühnentechnik GmbH, Dresden, Germany*

³*Centre for Audio, Acoustics and Vibration
University of Technology Sydney, Australia*

⁴*School of Engineering and Information Technology
University of New South Wales, Canberra, Australia*

⁵*Department of Electrical and Computer Engineering
The University of Texas at Austin, Austin, Texas 78712, USA*

⁶*Photonics Initiative, Advanced Science Research Center
City University of New York, USA*

(Dated: June 2, 2019)

SUPPLEMENTARY NOTE 1:

TIME CONVENTION AND INCIDENT FIELD

The incident pressure for a plane wave is given by

$$p_{\text{inc}}(t, \mathbf{x}) = p_0 e^{i(-\omega t + \mathbf{k}\mathbf{x})} \quad (\text{S1})$$

with p_0 as pressure amplitude, \mathbf{k} as wave vector, \mathbf{x} as position vector, ω as angular frequency and t as time.

Considering the linearized and simplified Euler's equation

$$-\rho_0 \frac{d\mathbf{v}}{dt} = \nabla p \quad (\text{S2})$$

the velocity vector \mathbf{v} can be described as following

$$\mathbf{v}(t, \mathbf{x}) = \frac{1}{i\rho_0 ck} \nabla p(t, \mathbf{x}). \quad (\text{S3})$$

For the velocity field in 2D it can be rearranged to

$$\begin{aligned} \mathbf{v}(t, \mathbf{x}) &= \frac{1}{i\rho_0 ck} \begin{bmatrix} \frac{\partial}{\partial x} \\ \frac{\partial}{\partial y} \end{bmatrix} p_0 e^{i(-\omega t + k_x x + k_y y)} \\ &= \frac{1}{\rho_0 ck} \begin{bmatrix} k_x \\ k_y \end{bmatrix} p_0 e^{i(-\omega t + k_x x + k_y y)} \\ &= \frac{\mathbf{k}}{\rho_0 ck} p_0 e^{i(\omega t - \mathbf{k}\mathbf{x})} = \frac{\mathbf{k}}{\rho_0 ck} p(t, \mathbf{x}) \end{aligned} \quad (\text{S4})$$

with ρ_0 as density and c as speed of sound. For practical reasons numerical differentiation is often required, giving the following approximate expression for the velocity

$$\mathbf{v}(t, \mathbf{x}) \approx \frac{1}{i\rho_0 ck} \frac{\Delta p}{\Delta \mathbf{x}} = \frac{1}{i\rho_0 ck} \frac{p(\mathbf{x}_2) - p(\mathbf{x}_1)}{\mathbf{x}_2 - \mathbf{x}_1} \quad (\text{S5})$$

SUPPLEMENTARY NOTE 2:

POLARIZABILITY EXTRACTION FROM NUMERICAL AND EXPERIMENTAL RESULTS

The incident pressure within a 2D system p_{inc} is represented by a cylindrical function expansion

$$p_{\text{inc}} = \sum_{n=-\infty}^{\infty} \beta_n J_n(kr) e^{in\theta} \quad (\text{S6})$$

and scattered pressure p_{scat} by

$$p_{\text{scat}} = \sum_{n=-\infty}^{\infty} \gamma_n H_n^{(1)}(kr) e^{in\theta} \quad (\text{S7})$$

with β_n as the incident field coefficient, γ_n as the scattered field coefficient, $J_n(kr)$ as Bessel function of order n , $H_n^{(1)}(kr)$ as Hankel function of first kind of order n and r and θ as cylindrical coordinates. If pressure data $p_{\text{scat}}(r, \theta)$ is available from an experiment or numerical simulation, β_n and γ_n coefficients can be obtained from the orthogonality of the exponential functions. To calculate these coefficients we hold radius constant at R^{inc} and R^{scat} respectively

$$\beta_n = \frac{1}{2\pi J_n(kR^{\text{inc}})} \int_0^{2\pi} p_{\text{inc}}(R^{\text{inc}}, \theta) e^{-in\theta} d\theta \quad (\text{S8})$$

and

$$\gamma_n = \frac{1}{2\pi H_n^{(1)}(kR^{\text{scat}})} \int_0^{2\pi} p_{\text{scat}}(R^{\text{scat}}, \theta) e^{-in\theta} d\theta. \quad (\text{S9})$$

The process for choosing R^{inc} and R^{scat} is outlined in Ref. [1].

These integrals are numerically approximated, with the scattered field given by

$$\gamma_n \approx \frac{1}{H_n^{(1)}(kR^{\text{scat}})} \sum_{i=1}^n p_{\text{scat}}(\theta_i) e^{-in\theta_i} \frac{1}{n}. \quad (\text{S10})$$

We compare this approach with the acoustic dipole and monopole moments as defined in Ref. [2]

$$M = \int_V \rho dV \quad (\text{S11})$$

$$\mathbf{D} = \int_V \rho \mathbf{r} dV. \quad (\text{S12})$$

We compare the scattered field from a monopole with the first term in the cylindrical function expansion

$$\begin{aligned} p_{Ms} &= \gamma_0 H_0^{(1)}(kr) \\ &= -\frac{ik^2 c^2 M}{4} H_0^{(1)}(kr) \end{aligned} \quad (\text{S13})$$

resulting in the following expression for the monopole coefficient

$$M = \frac{-4\gamma_0}{ik^2 c^2}. \quad (\text{S14})$$

A similar comparison is performed between the dipole scattering and the $n = \pm 1$ terms of the cylindrical function expansion

$$\begin{aligned} p_{Ds} &= (\gamma_1 H_1^{(1)}(kr)e^{i\theta} + \gamma_{-1} H_{-1}^{(1)}(kr)e^{-i\theta}) \\ &= (\gamma_1 e^{i\theta} - \gamma_{-1} e^{-i\theta}) H_1^{(1)}(kr) \\ &= ((\gamma_1 - \gamma_{-1}) \cos \theta + (\gamma_1 + \gamma_{-1}) i \sin \theta) H_1^{(1)}(kr) \\ &= -i \frac{k^3 c^2}{4} (D_x \cos \theta + D_y \sin \theta) H_1^{(1)}(kr) \end{aligned} \quad (\text{S15})$$

resulting in

$$\begin{aligned} D_x &= -(\gamma_1 - \gamma_{-1}) \frac{4}{ik^3 c^2} \\ D_y &= -(\gamma_1 + \gamma_{-1}) \frac{4}{k^3 c^2}. \end{aligned} \quad (\text{S16})$$

This can be summarized by a matrix

$$\begin{bmatrix} M \\ D_x \\ D_y \end{bmatrix} = \frac{-4}{ik^2 c^2} \begin{bmatrix} 0 & 1 & 0 \\ \frac{-1}{k} & 0 & \frac{1}{k} \\ \frac{i}{k} & 0 & \frac{i}{k} \end{bmatrix} \begin{bmatrix} \gamma_{-1} \\ \gamma_0 \\ \gamma_1 \end{bmatrix} \quad (\text{S17})$$

connecting the γ coefficients to monopole and dipole moments. The excitation of the monopole and dipole moments by an incident field can be described by a polarizability tensor $\boldsymbol{\alpha}$ in the form [2]

$$\begin{bmatrix} M \\ D_x \\ D_y \end{bmatrix} = \begin{bmatrix} \alpha^{pp} & \alpha_x^{pv} & \alpha_y^{pv} \\ \alpha_x^{vp} & \alpha_{xx}^{vv} & \alpha_{xy}^{vv} \\ \alpha_y^{vp} & \alpha_{yx}^{vv} & \alpha_{yy}^{vv} \end{bmatrix} \begin{bmatrix} \check{p}^{\text{inc}} \\ \check{v}_x^{\text{inc}} \\ \check{v}_y^{\text{inc}} \end{bmatrix}, \quad (\text{S18})$$

where \check{p}^{inc} and $\check{\mathbf{v}}^{\text{inc}}$ represent the incident pressure and velocity at the center of the meta-atom.

When the monopole and dipole moments and the incident pressure are known, we can obtain the polarizability tensor $\boldsymbol{\alpha}$ row by row for M , D_x and D_y from different incident angles $\theta_{1,2,3}$.

$$\begin{bmatrix} \alpha^{pp} & \alpha_x^{pv} & \alpha_y^{pv} \\ \alpha_x^{vp} & \alpha_{xx}^{vv} & \alpha_{xy}^{vv} \\ \alpha_y^{vp} & \alpha_{yx}^{vv} & \alpha_{yy}^{vv} \end{bmatrix} = \underbrace{\begin{bmatrix} \check{p}^{\text{inc}}(\theta_1) & \check{v}_x^{\text{inc}}(\theta_1) & \check{v}_y^{\text{inc}}(\theta_1) \\ \check{p}^{\text{inc}}(\theta_2) & \check{v}_x^{\text{inc}}(\theta_2) & \check{v}_y^{\text{inc}}(\theta_2) \\ \check{p}^{\text{inc}}(\theta_3) & \check{v}_x^{\text{inc}}(\theta_3) & \check{v}_y^{\text{inc}}(\theta_3) \end{bmatrix}^{-1}}_{\boldsymbol{r}^{-1}} \begin{bmatrix} M(\theta_1) & D_x(\theta_1) & D_y(\theta_1) \\ M(\theta_2) & D_x(\theta_2) & D_y(\theta_2) \\ M(\theta_3) & D_x(\theta_3) & D_y(\theta_3) \end{bmatrix}. \quad (\text{S19})$$

If data is available for additional incident angles the polarizability tensor can be found by least squares

$$\boldsymbol{\alpha} = (\boldsymbol{r}^T \boldsymbol{r})^{-1} \boldsymbol{r}^T \begin{bmatrix} M(\theta_1) & D_x(\theta_1) & D_y(\theta_1) \\ \vdots & \vdots & \vdots \\ M(\theta_N) & D_x(\theta_N) & D_y(\theta_N) \end{bmatrix}. \quad (\text{S20})$$

To meaningfully compare the different elements of the polarizability tensor, which have different units, the normalized polarizability tensor $\boldsymbol{\alpha}'$ is introduced as

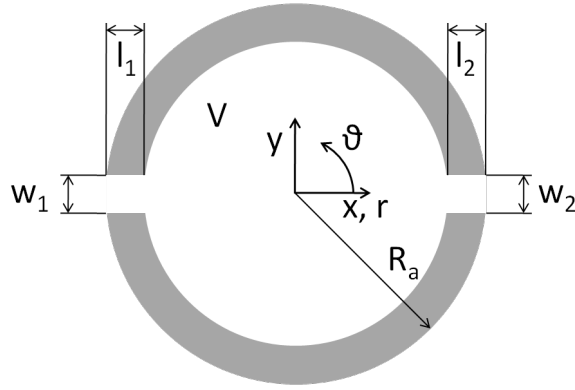
$$\begin{bmatrix} -\sqrt{2}M \\ ikD_x \\ ikD_y \end{bmatrix} = \begin{bmatrix} -2\alpha^{pp} & \frac{-\sqrt{2}}{\rho c}\alpha_x^{pv} & \frac{-\sqrt{2}}{\rho c}\alpha_y^{pv} \\ ik\sqrt{2}\alpha_x^{vp} & \frac{ik}{\rho c}\alpha_{xx}^{vv} & \frac{ik}{\rho c}\alpha_{xy}^{vv} \\ ik\sqrt{2}\alpha_y^{vp} & \frac{ik}{\rho c}\alpha_{yx}^{vv} & \frac{ik}{\rho c}\alpha_{yy}^{vv} \end{bmatrix} \begin{bmatrix} \frac{1}{\sqrt{2}}\check{p}^{\text{inc}} \\ \rho c\check{v}_x^{\text{inc}} \\ \rho c\check{v}_y^{\text{inc}} \end{bmatrix}, \quad (\text{S21})$$

which satisfies $\boldsymbol{\alpha}' = \boldsymbol{\alpha}'^{T-}$ [2] (i.e. the off-diagonal terms are anti-symmetric).

**SUPPLEMENTARY NOTE 3:
HELMHOLTZ-RESONATOR POLARIZABILITY**

General Model

Consider a Helmholtz resonator, containing an internal compressible volume V , with multiple incompressible apertures of length l and cross-section A_n . We model this as a 2D system, and set height $h = 1$ for simplicity in all analysis.



Supplementary Figure 1. Meta-atom geometry.

The air in each of the channels is treated as an incompressible mass of cross-section $A_n = w_n \cdot h$, and when it moves outwards by distance ξ_n , it leads to condensation

$$\Delta\rho/\rho = -\Delta V/V = A_n \xi_n / V \quad (\text{S22})$$

In the acoustic approximation, this condensation leads to an internal pressure increase p^{int}

$$p^{\text{int}} = K \Delta p / p = -K A_n \xi_n / V \quad (\text{S23})$$

where K is the bulk modulus. Considering multiple masses, we arrive at

$$p^{\text{int}} = -\frac{K}{V} \sum_m A_m \xi_m \quad (\text{S24})$$

An incident acoustic field results in some external pressure p^{ext} . In general this is different for each aperture. The inward-directed net force on mass n when subject to external pressure p_n^{ext} is balanced by p^{int} to give

$$F_p = A_n (p_n^{\text{ext}} - p^{\text{int}}) \quad (\text{S25})$$

The movement of the mass in the channels leads to an additional radiation force which must also be included in the balance equation

$$F_n^{\text{rad}} = R_n^{\text{rad}} \frac{d\xi_n}{dt} = \frac{\rho_0 c k^2 A_n^2}{8\pi} \frac{d\xi_n}{dt} \quad (\text{S26})$$

So the total force on mass n is

$$F_n = A_n(p_n^{\text{ext}} - p_n^{\text{int}}) + F_n^{\text{rad}} \quad (\text{S27})$$

By Newton's law, this gives the acceleration

$$F_n = -m_n \frac{d^2\xi_n}{dt^2} \quad (\text{S28})$$

Given that the mass in each channel is $m_n = \rho_0 A_n l_n$

$$F_n = -\rho_0 A_n l_n \frac{d^2\xi_n}{dt^2} \quad (\text{S29})$$

with l_n as the effective length [3]

$$l_n = l + 1.6 \cdot w_n \quad (\text{S30})$$

Substituting the explicit expression for the total force

$$A_n(p_n^{\text{ext}} - p_n^{\text{int}}) + F_n^{\text{rad}} = -\rho_0 A_n l_n \frac{d^2\xi_n}{dt^2} \quad (\text{S31})$$

Factor out the area A_n , and consider $p_n^{\text{rad}} = F_n^{\text{rad}}/A_n$

$$p_n^{\text{ext}} - p_n^{\text{int}} + p_n^{\text{rad}} = -\rho_0 l_n \frac{d^2\xi_n}{dt^2} \quad (\text{S32})$$

An explicit expression for the radiation pressure component can be derived from Kinsler [3, Section 10.8], which gives the radiation force as

$$p_n^{\text{rad}} = \frac{\rho_0 c k^2 A_n}{8\pi} \frac{d\xi_n}{dt} = \frac{\rho_0 c \omega^2}{8\pi c^2} A_n \frac{d\xi_n}{dt} = \frac{\rho_0 A_n \omega^2}{8\pi c} \frac{d\xi_n}{dt} \quad (\text{S33})$$

For harmonic waves, note that $d^2/dt^2 \rightarrow -\omega^2$, so we can write this as

$$p_n^{\text{rad}} = -\frac{\rho_0 A_n \omega^2}{8\pi c} \xi_n \quad (\text{S34})$$

Reorder Newton's equation for mass n

$$-\rho_0 l_n \frac{d^2\xi_n}{dt^2} + p_n^{\text{int}} - p_n^{\text{rad}} = p_n^{\text{ext}} \quad (\text{S35})$$

Substituting explicit expressions for p^{int} and p^{rad} leads to

$$\frac{\rho_0 A_n}{8\pi c} \frac{d^3 \xi_n}{dt^3} - \rho_0 l_n \frac{d^2 \xi_n}{dt^2} - \frac{K}{V} \sum_m A_m \xi_m = p_n^{\text{ext}} \quad (\text{S36})$$

Using $\exp(-i\omega t)$ time convention leads to

$$i\omega^3 \frac{\rho_0 A_n}{8\pi c} \xi_n + \omega^2 \rho_0 l_n \xi_n - \frac{K}{V} \sum_m A_m \xi_m = p_n^{\text{ext}}. \quad (\text{S37})$$

For a Helmholtz resonator with two apertures we can rewrite Eq. (S37) in matrix notation

$$\underbrace{\left(i\omega^3 \frac{\rho_0}{8\pi c} \begin{bmatrix} A_1 & 0 \\ 0 & A_2 \end{bmatrix} + \omega^2 \rho_0 \begin{bmatrix} l_1 & 0 \\ 0 & l_2 \end{bmatrix} - \frac{K}{V} \begin{bmatrix} A_1 & A_2 \\ A_1 & A_2 \end{bmatrix} \right)}_{\mathbf{K}_{\text{eq}}} \boldsymbol{\xi} = \mathbf{p}^{\text{ext}}. \quad (\text{S38})$$

To obtain the undamped eigenfrequency we neglect the radiative part \mathbf{R} and end up with the eigenvalue problem

$$\det \left(\frac{K}{V} \begin{bmatrix} A_1 & A_2 \\ A_1 & A_2 \end{bmatrix} - \omega^2 \rho_0 \begin{bmatrix} l_1 & 0 \\ 0 & l_2 \end{bmatrix} \right) = 0 \quad (\text{S39})$$

which results in

$$\omega_0 = \sqrt{\frac{c^2}{V} \left(\frac{A_1}{l_1} + \frac{A_2}{l_2} \right)} \quad (\text{S40})$$

and matches the common Helmholtz resonator considerations with two openings [4, 5].

Considering specifically the 2D case with height normalized to 1, the general solution for N apertures is

$$\omega_0 = \frac{c}{a-l} \sqrt{\frac{\sum_{n=1}^N w_n}{\pi l}}. \quad (\text{S41})$$

This model yields only one non-zero frequency mode independent of the number of apertures, since it assumes a homogeneous pressure distribution within the internal volume. The full solution accounting for radiative damping can be obtained by inversion as

$$\boldsymbol{\xi} = \mathbf{K}_{\text{eq}}^{-1} \mathbf{p}^{\text{ext}}. \quad (\text{S42})$$

Polarizability Tensor of Helmholtz Resonator with Two Apertures

We perform a multipole expansion considering the fluid displacement ξ_n in every aperture to obtain the monopole moment

$$M = \rho_0 \int_S \xi dS = \rho_0 \sum_n \xi_n A_n \quad (\text{S43})$$

and dipole moment

$$D = \rho_0 \int_S \xi r dS = \rho_0 \sum_n \xi_n r_n A_n \quad (\text{S44})$$

resulting in

$$\begin{bmatrix} M \\ D \end{bmatrix} = \rho_0 \begin{bmatrix} A_1 & A_2 \\ x_1 A_1 & x_2 A_2 \end{bmatrix} \boldsymbol{\xi} = \mathbf{A}_{MD} \boldsymbol{\xi}. \quad (\text{S45})$$

which can be inverted to yield

$$\boldsymbol{\xi} = \begin{bmatrix} \frac{x_2}{A_1 \rho_0 (x_1 - x_2)} & \frac{1}{A_1 \rho_0 (x_1 - x_2)} \\ \frac{x_1}{A_2 \rho_0 (x_1 - x_2)} & -\frac{1}{A_2 \rho_0 (x_1 - x_2)} \end{bmatrix} \begin{bmatrix} M \\ D \end{bmatrix} = \mathbf{A}_{MD}^{-1} \begin{bmatrix} M \\ D \end{bmatrix}. \quad (\text{S46})$$

This connects the motion of the effective masses of the Helmholtz resonator to M and D . To find the polarizability of the Helmholtz resonator we must link the external pressure at each aperture p^{ext} to the incident pressure and velocity at the center of the meta-atom, under the assumption that its radius is small compared to the wavelength

$$\check{p}^{\text{inc}} = \frac{p_1^{\text{ext}} + p_2^{\text{ext}}}{2} \quad (\text{S47})$$

and based on Eq. (S5)

$$\check{v}_x^{\text{inc}} = \frac{p_2^{\text{ext}} - p_1^{\text{ext}}}{i2a\rho_0\omega} \quad (\text{S48})$$

with $a = R$ as particle radius. We can write it in a matrix form as

$$\begin{bmatrix} \check{p}^{\text{inc}} \\ \check{v}_x^{\text{inc}} \end{bmatrix} = \begin{bmatrix} \frac{1}{2} & \frac{1}{2} \\ -\frac{1}{i2a\rho_0\omega} & \frac{1}{i2a\rho_0\omega} \end{bmatrix} \begin{bmatrix} p_1^{\text{ext}} \\ p_2^{\text{ext}} \end{bmatrix} = \mathbf{A}_{pv} \mathbf{p}^{\text{ext}} \quad (\text{S49})$$

or as the inverse

$$\mathbf{p}^{\text{ext}} = \begin{bmatrix} 1 & -ia\rho_0\omega \\ 1 & ia\rho_0\omega \end{bmatrix} \begin{bmatrix} \check{p}^{\text{inc}} \\ \check{v}_x^{\text{inc}} \end{bmatrix} = \mathbf{A}_{pv}^{-1} \begin{bmatrix} \check{p}^{\text{inc}} \\ \check{v}_x^{\text{inc}} \end{bmatrix} \quad (\text{S50})$$

Now we can combine Eqs. (S45), (S42) and (S50) and write

$$\begin{aligned} \begin{bmatrix} M \\ D_x \end{bmatrix} &= \mathbf{A}_{MD} \boldsymbol{\xi} \\ &= \mathbf{A}_{MD} \mathbf{K}_{\text{eq}}^{-1} \mathbf{p}^{\text{ext}} \\ &= \mathbf{A}_{MD} \mathbf{K}_{\text{eq}}^{-1} \mathbf{A}_{pv}^{-1} \begin{bmatrix} \check{p}^{\text{inc}} \\ \check{v}_x^{\text{inc}} \end{bmatrix} \\ \begin{bmatrix} M \\ D_x \end{bmatrix} &= \boldsymbol{\alpha}_{\text{res}} \begin{bmatrix} \check{p}^{\text{inc}} \\ \check{v}_x^{\text{inc}} \end{bmatrix} \end{aligned} \quad (\text{S51})$$

which directly gives us the polarizability tensor $\boldsymbol{\alpha}$. The inverse of the polarizability tensor is required later in this derivation and it can be obtained as

$$\begin{aligned}\boldsymbol{\alpha}_{\text{res}}^{-1} &= \mathbf{A}_{pv} \mathbf{K}_{\text{eq}} \mathbf{A}_{MD}^{-1} \\ &= \begin{bmatrix} \frac{1}{2} & \frac{1}{2} \\ -\frac{1}{i2a\rho_0\omega} & \frac{1}{i2a\rho_0\omega} \end{bmatrix} (i\omega^3 \mathbf{R} + \omega^2 \mathbf{M} - \mathbf{K}) \begin{bmatrix} \frac{x_2}{A_1 \rho_0 (x_1 - x_2)} & \frac{1}{A_1 \rho_0 (x_1 - x_2)} \\ \frac{x_1}{A_2 \rho_0 (x_1 - x_2)} & -\frac{1}{A_2 \rho_0 (x_1 - x_2)} \end{bmatrix}.\end{aligned}\quad (\text{S52})$$

Polarizability Tensor for Resonator with One Aperture

To obtain the highest possible Willis coupling for the Helmholtz resonator the highest level of asymmetry should be applied by closing one of the two channels. Now the response of the resonator given by Eq. (S37) becomes a scalar equation

$$\left(i\omega^3 \frac{\rho_0 A_1}{8\pi c} + \omega^2 \rho_0 l_1 - \frac{K}{V} A_1 \right) \xi_1 = K_{\text{eq}} \xi_1 = p_1^{\text{ext}}.\quad (\text{S53})$$

This implies further simplifications of Eq. (S51) to

$$\begin{aligned}\begin{bmatrix} M \\ D_x \end{bmatrix} &= \rho_0 \begin{bmatrix} A_1 \\ x_1 A_1 \end{bmatrix} \frac{1}{K_{\text{eq}}} \begin{bmatrix} 1 & -ia\rho_0\omega \end{bmatrix} \begin{bmatrix} \check{p}^{\text{inc}} \\ \check{v}_x^{\text{inc}} \end{bmatrix} \\ &= \frac{\rho_0}{i\omega^3 \frac{\rho_0 A_1}{8\pi c} + \omega^2 \rho_0 l_1 - \frac{K}{V} A_1} \begin{bmatrix} A_1 & -ia\rho_0\omega A_1 \\ x_1 A_1 & -ia\rho_0\omega x_1 A_1 \end{bmatrix} \begin{bmatrix} \check{p}^{\text{inc}} \\ \check{v}_x^{\text{inc}} \end{bmatrix} \\ &= \boldsymbol{\alpha}_{\text{res}} \begin{bmatrix} \check{p}^{\text{inc}} \\ \check{v}_x^{\text{inc}} \end{bmatrix}\end{aligned}\quad (\text{S54})$$

The polarizability tensor is now a results of an outer product of two vectors, which gives a zero determinant. The tensor is not invertible in that case, so it will be treated differently in the coupling procedure outlined below.

SUPPLEMENTARY NOTE 4:
CYLINDER POLARIZABILITY

The meta-atom consists of a resonator inside a cylindrical body. The direct scattering from the outer cylinder surface contributes to the total scattering of the whole meta-atom and should be considered as well. The scattering of a plane wave from a cylinder is given analytically as

$$p^{\text{scat}}(r, \theta) = -p_0 \sum_{n=-\infty}^{\infty} i^n \frac{\frac{d}{d(ka)} J_n(ka)}{\frac{d}{d(ka)} H_n^{(1)}(ka)} H_n^{(1)}(kr) e^{in(\theta-\theta_0)} \quad (\text{S55})$$

with $J_n(z)$ as a Bessel functions of n -th order, $H_n^{(1)}(z)$ as a Hankel function of the second kind of n -th order, a as the cylinder radius, θ_0 as the angle of incidence, k as the wave number, and r and θ as cylindrical coordinates. For small cylinders the scattered field can be described by monopole and dipole components corresponding to the $n = 0$ and $n = \pm 1$ terms. This simplifies the scattered field to

$$p^{\text{scat}}(r, \theta) = -p_0 \left(-i \frac{J'_{-1}(ka)}{H_{-1}^{(1)'}(ka)} H_{-1}^{(1)}(kr) e^{-i(\theta-\theta_0)} + \right. \\ \left. + \frac{J'_0(ka)}{H_0^{(1)'}(ka)} H_0^{(1)}(kr) + \right. \\ \left. + i \frac{J'_1(ka)}{H_1^{(1)'}(ka)} H_1^{(1)}(kr) e^{i(\theta-\theta_0)} \right) \quad (\text{S56})$$

or

$$p^{\text{scat}}(r, \theta) = \gamma_{-1} H_{-1}^{(1)}(kr) e^{-i(\theta-\theta_0)} + \gamma_0 H_0^{(1)}(kr) + \gamma_1 H_1^{(1)}(kr) e^{i(\theta-\theta_0)}. \quad (\text{S57})$$

Using Eq. (S14) the monopole moment can be calculated as

$$M = \frac{4}{ik^2 c^2} \frac{J'_0(ka)}{H_0^{(1)'}(ka)} p_0 \quad (\text{S58})$$

and after substituting $p_0 = p^{\text{inc}}$ for $x = 0$ and $\theta = 0$ the monopole component of the polarizability tensor appears as

$$\alpha_{pp}^{\text{cyl}} = \frac{4}{ik^2 c^2} \frac{J'_0(ka)}{H_0^{(1)'}(ka)}. \quad (\text{S59})$$

Evaluating the derivatives $J'_0(ka) = J_{-1}(ka) = -J_1(ka)$ and $H_0^{(1)'}(ka) = -H_1^{(1)}(ka)$ [3] leads to

$$\alpha_{pp}^{\text{cyl}} = \frac{4}{ik^2 c^2} \frac{J_1(ka)}{H_1^{(1)}(ka)}. \quad (\text{S60})$$

For the dipole moment we can perform an analogous process by substituting $\gamma_{-1,1}$ from (S56) into (S16). Due to symmetry, it suffices to consider only a single component of the dipole moment. We consider incident wave propagation parallel to the x-axis with $\theta_0 = 0$ so that $e^{i\theta_0} = 1$, yielding

$$D_x = \frac{4}{k^3 c^2} \left(\frac{J_1'(ka)}{H_1^{(1)'}(ka)} + \frac{J_{-1}'(ka)}{H_{-1}^{(1)'}(ka)} \right) p_0, \quad (\text{S61})$$

which can be further simplified to

$$D_x = \frac{8}{k^3 c^2} \frac{J_1'(ka)}{H_1^{(1)'}(ka)} p_0. \quad (\text{S62})$$

Substituting the expression $p_0 = \rho_0 c v_0$ results in the final equation

$$D_x = \frac{8\rho_0}{k^3 c} \frac{J_1'(ka)}{H_1^{(1)'}(ka)} v_0, \quad (\text{S63})$$

which gives us the polarizability tensor component

$$\alpha_{vv}^{\text{cyl}} = \frac{8\rho_0}{k^3 c} \frac{J_1'(ka)}{H_1^{(1)'}(ka)}. \quad (\text{S64})$$

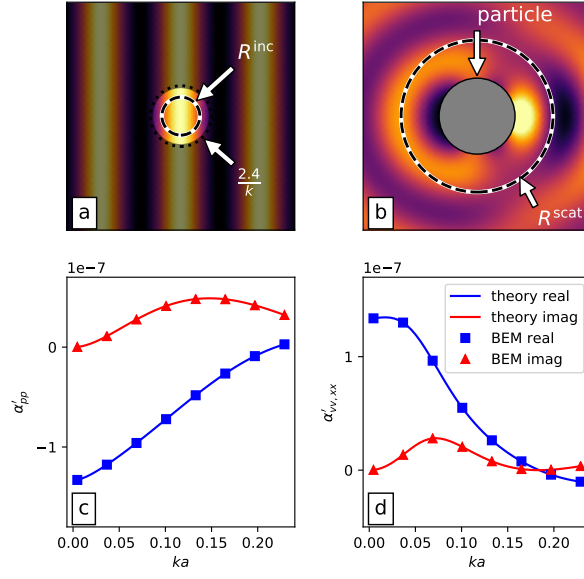
Due to the symmetry of a cylinder no Willis coupling is present and we can write the polarizability tensor as

$$\boldsymbol{\alpha}_{\text{cyl}} = \begin{bmatrix} \alpha_{pp}^{\text{cyl}} & 0 \\ 0 & \alpha_{vv}^{\text{cyl}} \end{bmatrix} = \begin{bmatrix} \frac{4}{ik^2 c^2} \frac{J_1(ka)}{H_1^{(1)}(ka)} & 0 \\ 0 & \frac{8\rho_0}{k^3 c} \frac{J_1'(ka)}{H_1^{(1)'}(ka)} \end{bmatrix} \quad (\text{S65})$$

and its inverse as

$$\boldsymbol{\alpha}_{\text{cyl}}^{-1} = \begin{bmatrix} \frac{ik^2 c^2}{4} \frac{H_1^{(1)}(ka)}{J_1(ka)} & 0 \\ 0 & \frac{k^3 c}{8\rho_0} \frac{H_1^{(1)'}(ka)}{J_1'(ka)} \end{bmatrix}. \quad (\text{S66})$$

Fig. 2(c, d) shows analytically (solid lines) and numerically determined (square and triangle markers) polarizability of a cylinder. Here the cylinder radius $a = 50$ mm, $c = 343$ m/s and $\rho_0 = 1.2$ kg/m³. The analytical solution accurately matches the results extracted from the numerically calculated scattered field. The extracted off-diagonal components have a maximum dimension of 10^{-12} , which is equal to zero within numerical precision and hence the symmetry condition $\boldsymbol{\alpha}' = \boldsymbol{\alpha}'^T$ [2] is trivially satisfied. This results validates the extraction method in combination with the custom BEM code.



Supplementary Figure 2. Scattering from a cylinder. a: Illustration of chosen value of R^{inc} , for incident pressure field without particle. Dark region above $r = \frac{2.4}{k}$ can cause Eq. (S8) to become singular and should be avoided. b: Illustration of chosen value of R^{scat} , for the scattered pressure field from a cylinder. c: Monopole polarizability of a cylinder α'_{pp} given by theory (solid lines) and determined with BEM (square and triangle markers). d: Dipole polarizability of a cylinder α'_{vv} .

SUPPLEMENTARY NOTE 5:

RESONATOR-CYLINDER COUPLING

Analytical Coupling of Cylinder and Resonator in 1D

The meta-atom consists of a resonator inside a cylindrical body, and both objects contribute significantly to scattering. Furthermore the incident field for each object is influenced by the other, which implies that a coupled model is required.

General Coupling Model

The incident field of cylinder and resonator models can be expressed as

$$\begin{aligned}\check{p}_{\text{inc}}^{\text{cyl}} &= \check{p}_{\text{inc}} + \check{p}_{\text{scat}}^{\text{res}} \\ \check{p}_{\text{inc}}^{\text{res}} &= \check{p}_{\text{inc}} + \check{p}_{\text{scat}}^{\text{cyl}}\end{aligned}\tag{S67}$$

taking the influence by each other into account. Considering the cylinder the scattered field can be calculated as

$$\begin{bmatrix} \check{p} \\ \check{\mathbf{v}} \end{bmatrix}_{\text{scat}}^{\text{cyl}} = \underbrace{\begin{bmatrix} \frac{1}{2} & \frac{1}{2} \\ -\frac{1}{i2a\rho_0\omega} & \frac{1}{i2a\rho_0\omega} \end{bmatrix} \begin{bmatrix} f_M(r_1) & f_D(r_1, \theta_1) \\ f_M(r_2) & f_D(r_2, \theta_2) \end{bmatrix}}_{\mathbf{E}} \begin{bmatrix} M \\ \mathbf{D} \end{bmatrix}^{\text{cyl}}\tag{S68}$$

where $f_M(r)$ and $f_D(r, \theta)$ are the parts of (S13) and S15 corresponding to monopole and dipole moment as

$$f_M(r) = -\frac{ik^2c^2}{4}H_0^{(1)}(kr)\tag{S69}$$

and

$$f_D(r, \theta) = -\frac{ik^3c^2}{4}H_1^{(1)}(kr)\cos(\theta).\tag{S70}$$

For symmetrical aperture the coordinates of inlets are $r_1 = r_2 = a$ and $\theta_1 = \theta_2 + \pi$, which implies

$$\begin{aligned}f_M(r_1) &= f_M(r_2) = f_M(a) = f_M \\ -f_D(r_1, \theta_1) &= f_D(r_2, \theta_1) = f_D(a) = f_D\end{aligned}\tag{S71}$$

and

$$\mathbf{E} = \begin{bmatrix} f_M & 0 \\ 0 & \frac{f_D}{ia\rho_0\omega} \end{bmatrix}.\tag{S72}$$

After substituting the moments with polarizability tensor $\boldsymbol{\alpha}$ and incident field $\mathbf{u}^{\text{inc}} = \begin{bmatrix} \check{p}^{\text{inc}} & \check{\mathbf{v}}^{\text{inc}} \end{bmatrix}^T$ we end up with

$$\mathbf{u}_{\text{scat}}^{\text{cyl}} = \mathbf{E}\boldsymbol{\alpha}_{\text{cyl}}\mathbf{u}_{\text{inc}}^{\text{cyl}} \quad (\text{S73})$$

which incorporated into Eq. (S67) results in

$$(\mathbf{E}\boldsymbol{\alpha}_{\text{cyl}})^{-1}\mathbf{u}_{\text{scat}}^{\text{cyl}} = \mathbf{u}_{\text{inc}} + \mathbf{u}_{\text{scat}}^{\text{res}}. \quad (\text{S74})$$

After completing the same consideration for the resonator we obtain the following two equations

$$\begin{aligned} \mathbf{u}_{\text{inc}} &= (\mathbf{E}\boldsymbol{\alpha}_{\text{cyl}})^{-1}\mathbf{u}_{\text{scat}}^{\text{cyl}} - \mathbf{u}_{\text{scat}}^{\text{res}} \\ \mathbf{u}_{\text{inc}} &= (\mathbf{E}\boldsymbol{\alpha}_{\text{res}})^{-1}\mathbf{u}_{\text{scat}}^{\text{res}} - \mathbf{u}_{\text{scat}}^{\text{cyl}} \end{aligned} \quad (\text{S75})$$

which we combine to a system of equations

$$\begin{bmatrix} \mathbf{u}_{\text{inc}} \\ \mathbf{u}_{\text{inc}} \end{bmatrix} = \begin{bmatrix} (\mathbf{E}\boldsymbol{\alpha}_{\text{cyl}})^{-1} & -\mathbf{I} \\ -\mathbf{I} & (\mathbf{E}\boldsymbol{\alpha}_{\text{res}})^{-1} \end{bmatrix} \begin{bmatrix} \mathbf{u}_{\text{scat}}^{\text{cyl}} \\ \mathbf{u}_{\text{scat}}^{\text{res}} \end{bmatrix}. \quad (\text{S76})$$

The scattered pressure can be calculated from the monopole and dipole moments (S13), (S15) and we get

$$\begin{bmatrix} \mathbf{u}_{\text{inc}} \\ \mathbf{u}_{\text{inc}} \end{bmatrix} = \begin{bmatrix} (\mathbf{E}\boldsymbol{\alpha}_{\text{cyl}})^{-1} & -\mathbf{I} \\ -\mathbf{I} & (\mathbf{E}\boldsymbol{\alpha}_{\text{res}})^{-1} \end{bmatrix} \begin{bmatrix} \mathbf{E} & \mathbf{0} \\ \mathbf{0} & \mathbf{E} \end{bmatrix} \begin{bmatrix} \begin{bmatrix} M & D \end{bmatrix}_{\text{cyl}}^T \\ \begin{bmatrix} M & D \end{bmatrix}_{\text{res}}^T \end{bmatrix} \quad (\text{S77})$$

and after matrix multiplication we end up with

$$\begin{bmatrix} \check{p}_{\text{inc}} \\ \check{v}_{\text{inc}} \\ \check{p}_{\text{inc}} \\ \check{v}_{\text{inc}} \end{bmatrix} = \begin{bmatrix} \begin{bmatrix} \alpha_{pp} & \alpha_{pv} \\ \alpha_{vp} & \alpha_{vv} \end{bmatrix}_{\text{cyl}}^{-1} & -\mathbf{E} \\ -\mathbf{E} & \begin{bmatrix} \alpha_{pp} & \alpha_{pv} \\ \alpha_{vp} & \alpha_{vv} \end{bmatrix}_{\text{res}}^{-1} \end{bmatrix} \begin{bmatrix} M_{\text{cyl}} \\ D_{\text{cyl}} \\ M_{\text{res}} \\ D_{\text{res}} \end{bmatrix}. \quad (\text{S78})$$

Coupling between Cylinder and Helmholtz Resonator in the Absence of Willis Coupling

When the structure has mirror symmetry, the Willis coupling terms α_{pv} and α_{vp} are zero for the Helmholtz resonator. The Willis coupling terms of the cylinder are always zero, so

we end up with a simplified system of equations

$$\begin{bmatrix} \check{p}_{\text{inc}} \\ \check{v}_{\text{inc}} \\ \check{p}_{\text{inc}} \\ \check{v}_{\text{inc}} \end{bmatrix} = \begin{bmatrix} (\alpha_{pp}^{\text{cyl}})^{-1} & 0 & -f_M & 0 \\ 0 & (\alpha_{vv}^{\text{cyl}})^{-1} & 0 & -\frac{f_D}{ia\rho_0\omega} \\ -f_M & 0 & (\alpha_{pp}^{\text{res}})^{-1} & 0 \\ 0 & -\frac{f_D}{ia\rho_0\omega} & 0 & (\alpha_{vv}^{\text{res}})^{-1} \end{bmatrix} \begin{bmatrix} M_{\text{cyl}} \\ D_{\text{cyl}} \\ M_{\text{res}} \\ D_{\text{res}} \end{bmatrix} = \mathbf{B}^{-1} \begin{bmatrix} M_{\text{cyl}} \\ D_{\text{cyl}} \\ M_{\text{res}} \\ D_{\text{res}} \end{bmatrix} \quad (\text{S79})$$

where the matrix \mathbf{B} is the total coupling matrix, which connect the incident field to the individual monopole and dipole moments. In absence of Willis coupling the monopole and dipole moments are completely uncoupled from each other and this allows to separate them into two independent matrix equations

$$\begin{bmatrix} \check{p}_{\text{inc}} \\ \check{p}_{\text{inc}} \end{bmatrix} = \begin{bmatrix} (\alpha_{pp}^{\text{cyl}})^{-1} & -f_M \\ -f_M & (\alpha_{pp}^{\text{res}})^{-1} \end{bmatrix} \begin{bmatrix} M_{\text{cyl}} \\ M_{\text{res}} \end{bmatrix} \quad (\text{S80})$$

and

$$\begin{bmatrix} \check{v}_{\text{inc}} \\ \check{v}_{\text{inc}} \end{bmatrix} = \begin{bmatrix} (\alpha_{vv}^{\text{cyl}})^{-1} & -\frac{f_D}{ia\rho_0\omega} \\ -\frac{f_D}{ia\rho_0\omega} & (\alpha_{vv}^{\text{res}})^{-1} \end{bmatrix} \begin{bmatrix} D_{\text{cyl}} \\ D_{\text{res}} \end{bmatrix} \quad (\text{S81})$$

The monopole moments can be now obtained by matrix inversion as

$$\begin{bmatrix} M_{\text{cyl}} \\ M_{\text{res}} \end{bmatrix} = \frac{1}{(\alpha_{pp}^{\text{cyl}})^{-1}(\alpha_{pp}^{\text{res}})^{-1} - f_M^2} \begin{bmatrix} (\alpha_{pp}^{\text{res}})^{-1} & f_M \\ f_M & (\alpha_{pp}^{\text{cyl}})^{-1} \end{bmatrix} \begin{bmatrix} \check{p}_{\text{inc}} \\ \check{p}_{\text{inc}} \end{bmatrix} \quad (\text{S82})$$

and summed to give the total monopole moment

$$M_{\text{tot}} = M_{\text{cyl}} + M_{\text{res}}. \quad (\text{S83})$$

The resulting equation

$$M_{\text{tot}} = \frac{(\alpha_{pp}^{\text{cyl}})^{-1} + (\alpha_{pp}^{\text{res}})^{-1} + 2f_M}{(\alpha_{pp}^{\text{cyl}})^{-1}(\alpha_{pp}^{\text{res}})^{-1} - f_M^2} \check{p}_{\text{inc}} \quad (\text{S84})$$

gives the uncoupled monopole component of the total polarizability tensor

$$\alpha_{pp}^{\text{tot}} = \frac{(\alpha_{pp}^{\text{cyl}})^{-1} + (\alpha_{pp}^{\text{res}})^{-1} + 2f_M}{(\alpha_{pp}^{\text{cyl}})^{-1}(\alpha_{pp}^{\text{res}})^{-1} - f_M^2}. \quad (\text{S85})$$

The dipole moment can be determined in the same way from

$$\begin{bmatrix} D_{\text{cyl}} \\ D_{\text{res}} \end{bmatrix} = \frac{1}{(\alpha_{vv}^{\text{cyl}})^{-1}(\alpha_{vv}^{\text{res}})^{-1} - (\frac{f_D}{ia\rho_0\omega})^2} \begin{bmatrix} (\alpha_{vv}^{\text{res}})^{-1} & \frac{f_D}{ia\rho_0\omega} \\ \frac{f_D}{ia\rho_0\omega} & (\alpha_{vv}^{\text{cyl}})^{-1} \end{bmatrix} \begin{bmatrix} \check{v}_{\text{inc}} \\ \check{v}_{\text{inc}} \end{bmatrix} \quad (\text{S86})$$

as a sum

$$D_{tot} = D_{cyl} + D_{res}. \quad (\text{S87})$$

It gives us the total dipole moment as

$$D_{tot} = \frac{(\alpha_{vv}^{cyl})^{-1} + (\alpha_{vv}^{res})^{-1} + \frac{2f_D}{ia\rho_0\omega}}{(\alpha_{vv}^{cyl})^{-1}(\alpha_{vv}^{res})^{-1} - \left(\frac{f_D}{ia\rho_0\omega}\right)^2} \check{v}_{inc} \quad (\text{S88})$$

and the corresponding component of the polarizability tensor

$$\alpha_{vv}^{tot} = \frac{(\alpha_{vv}^{cyl})^{-1} + (\alpha_{vv}^{res})^{-1} + \frac{2f_D}{ia\rho_0\omega}}{(\alpha_{vv}^{cyl})^{-1}(\alpha_{vv}^{res})^{-1} - \left(\frac{f_D}{ia\rho_0\omega}\right)^2}. \quad (\text{S89})$$

Finally the total polarizability tensor is defined as

$$\boldsymbol{\alpha}^{tot} = \begin{bmatrix} \alpha_{pp}^{tot} & 0 \\ 0 & \alpha_{vv}^{tot} \end{bmatrix}. \quad (\text{S90})$$

Willis Coupling with two Apertures

To get the Willis coupling in the particle the symmetry of the resonator has to be disturbed. This can be easily achieved by changing the ratio of the aperture sizes to be unequal. This implies the appearance of Willis coupling term α_{pv} and α_{vp} in $\boldsymbol{\alpha}^{res}$ and the coupling matrix \mathbf{B}^{-1} is written as

$$\begin{bmatrix} \check{p}_{inc} \\ \check{v}_{inc} \\ \check{p}_{inc} \\ \check{v}_{inc} \end{bmatrix} = \begin{bmatrix} (\alpha_{pp}^{cyl})^{-1} & 0 & -f_M & 0 \\ 0 & (\alpha_{vv}^{cyl})^{-1} & 0 & -\frac{f_D}{ia\rho_0\omega} \\ -f_M & 0 & (\alpha_{pp}^{res})^{-1} & (\alpha_{pv}^{res})^{-1} \\ 0 & -\frac{f_D}{ia\rho_0\omega} & (\alpha_{vp}^{res})^{-1} & (\alpha_{vv}^{res})^{-1} \end{bmatrix} \begin{bmatrix} M_{cyl} \\ D_{cyl} \\ M_{res} \\ D_{res} \end{bmatrix} = \mathbf{B}^{-1} \begin{bmatrix} M_{cyl} \\ D_{cyl} \\ M_{res} \\ D_{res} \end{bmatrix} \quad (\text{S91})$$

Now the monopole and dipole moment equations can not be treated separately and the total matrix \mathbf{B}^{-1} has to be inverted

$$\begin{bmatrix} M_{cyl} \\ D_{cyl} \\ M_{res} \\ D_{res} \end{bmatrix} = \mathbf{B} \begin{bmatrix} \check{p}_{inc} \\ \check{v}_{inc} \\ \check{p}_{inc} \\ \check{v}_{inc} \end{bmatrix} = [\beta_{ij}] \begin{bmatrix} \check{p}_{inc} \\ \check{v}_{inc} \\ \check{p}_{inc} \\ \check{v}_{inc} \end{bmatrix}. \quad (\text{S92})$$

From the uncoupled case we know that $M_{tot} = M_{cyl} + M_{res}$ and $D_{tot} = D_{cyl} + D_{res}$ and we can write the total moments as

$$\begin{bmatrix} M_{tot} \\ D_{tot} \end{bmatrix} = \begin{bmatrix} (\beta_{11} + \beta_{13} + \beta_{31} + \beta_{33}) & (\beta_{12} + \beta_{14} + \beta_{32} + \beta_{34}) \\ (\beta_{21} + \beta_{23} + \beta_{41} + \beta_{43}) & (\beta_{22} + \beta_{24} + \beta_{42} + \beta_{44}) \end{bmatrix} \begin{bmatrix} \check{p}_{inc} \\ \check{v}_{inc} \end{bmatrix} \quad (\text{S93})$$

Finally the total polarizability tensor for presence of Willis coupling is obtained as

$$\boldsymbol{\alpha}^{tot} = \begin{bmatrix} (\beta_{11} + \beta_{13} + \beta_{31} + \beta_{33}) & (\beta_{12} + \beta_{14} + \beta_{32} + \beta_{34}) \\ (\beta_{21} + \beta_{23} + \beta_{41} + \beta_{43}) & (\beta_{22} + \beta_{24} + \beta_{42} + \beta_{44}) \end{bmatrix}. \quad (\text{S94})$$

Willis Coupling with one Aperture

When the resonator has only one aperture, the polarizability tensor is simplified, but at the same time it becomes non-invertible as it has a zero determinant. In this case the inversion can be avoided by multiplication of the corresponding coupling matrix rows with $\boldsymbol{\alpha}_{\text{res}}$

$$\begin{bmatrix} \mathbf{u}_{\text{inc}} \\ \boldsymbol{\alpha}_{\text{res}} \mathbf{u}_{\text{inc}} \end{bmatrix} = \begin{bmatrix} \boldsymbol{\alpha}_{\text{cyl}}^{-1} & -\mathbf{E} \\ -\boldsymbol{\alpha}_{\text{res}} \mathbf{E} & \boldsymbol{\alpha}_{\text{res}} \boldsymbol{\alpha}_{\text{res}}^{-1} \end{bmatrix} \begin{bmatrix} \begin{bmatrix} M & D \end{bmatrix}_{\text{cyl}}^T \\ \begin{bmatrix} M & D \end{bmatrix}_{\text{res}}^T \end{bmatrix}. \quad (\text{S95})$$

We can expand it as

$$\begin{bmatrix} \check{p}_{\text{inc}} \\ \check{v}_{\text{inc}} \\ \alpha_{pp}^{\text{res}} \check{p}_{\text{inc}} + \alpha_{pv}^{\text{res}} \check{v}_{\text{inc}} \\ \alpha_{vp}^{\text{res}} \check{p}_{\text{inc}} + \alpha_{vv}^{\text{res}} \check{v}_{\text{inc}} \end{bmatrix} = \begin{bmatrix} (\alpha_{pp}^{\text{cyl}})^{-1} & 0 & -f_M & 0 \\ 0 & (\alpha_{vv}^{\text{cyl}})^{-1} & 0 & -\frac{f_D}{ia\rho_0\omega} \\ -\alpha_{pp}^{\text{res}} f_M & -\frac{\alpha_{pv}^{\text{res}} f_D}{ia\rho_0\omega} & 1 & 0 \\ -\alpha_{vp}^{\text{res}} f_M & -\frac{\alpha_{vv}^{\text{res}} f_D}{ia\rho_0\omega} & 0 & 1 \end{bmatrix} \begin{bmatrix} M_{\text{cyl}} \\ D_{\text{cyl}} \\ M_{\text{res}} \\ D_{\text{res}} \end{bmatrix} = \mathbf{B}'^{-1} \begin{bmatrix} M_{\text{cyl}} \\ D_{\text{cyl}} \\ M_{\text{res}} \\ D_{\text{res}} \end{bmatrix} \quad (\text{S96})$$

and analogously to the two aperture case form the total polarizability tensor

$$\boldsymbol{\alpha}^{tot} = \begin{bmatrix} \left(\begin{array}{c} \beta_{11} + \beta_{31} + \\ +\alpha_{pp}^{\text{res}} (\beta_{13} + \beta_{33}) + \\ +\alpha_{pv}^{\text{res}} (\beta_{14} + \beta_{34}) \end{array} \right) & \left(\begin{array}{c} \beta_{12} + \beta_{32} + \\ +\alpha_{pv}^{\text{res}} (\beta_{13} + \beta_{33}) + \\ +\alpha_{vv}^{\text{res}} (\beta_{14} + \beta_{34}) \end{array} \right) \\ \left(\begin{array}{c} \beta_{21} + \beta_{41} + \\ +\alpha_{pp}^{\text{res}} (\beta_{23} + \beta_{43}) + \\ +\alpha_{pv}^{\text{res}} (\beta_{13} + \beta_{33}) \end{array} \right) & \left(\begin{array}{c} \beta_{22} + \beta_{42} + \\ +\alpha_{vp}^{\text{res}} (\beta_{23} + \beta_{43}) + \\ +\alpha_{vv}^{\text{res}} (\beta_{13} + \beta_{33}) \end{array} \right) \end{bmatrix}. \quad (\text{S97})$$

SUPPLEMENTARY NOTE 6:

EFFECTIVE LENGTH AND RADIATIVE LOSSES CORRECTION

The commonly used formulas for radiative damping and mass [3], are specific to circular geometries, and require modification for the case of our meta-atom. The radiative losses dictate the amplitudes of the polarizability tensor components and are of crucial importance for correctly determining Willis coupling coefficients. Furthermore the radiative mass is represented by adjusting the effective length of the apertures to correctly match the numerical results. This influences the resonant frequency.

For finetuning of these parameter we spanned a grid in parameter space over $w = [3, 12]$ mm and $l = [5, 10]$ mm where for every parameter combination the polarizability tensor was numerically determined. The numerical results were used for nonlinear optimization of the effective length correction coefficient c_{eff} and radiation loss coefficient c_{rad} . These coefficients are incorporated into the model through the equations

$$l_{\text{eff}} = l + c_{\text{eff}} \quad (\text{S98})$$

and

$$K_{\text{eq}} = i\omega^3 c_{\text{rad}} \frac{\rho_0 A}{c} + \omega^2 \rho_0 l_{\text{eff}} - \frac{K}{V} A, \quad (\text{S99})$$

which implies that

$$\boldsymbol{\alpha} = f(c_{\text{eff}}, c_{\text{rad}}, \omega \dots). \quad (\text{S100})$$

The optimization function is based on the Willis coupling component α_{pv} and is defined as

$$f_{\text{opt}}(c_{\text{eff}}, c_{\text{rad}}) = \|\alpha_{pv}^{\text{BEM}}(\omega) - \alpha_{pv}^{\text{analyt}}(\omega, c_{\text{eff}}, c_{\text{rad}})\|_2 \longrightarrow \min. \quad (\text{S101})$$

Minimizing this function for every point in (l, w) space gives us a c_{eff} -surface and a c_{rad} -surface. These surfaces represent the optimal values for the evaluated points, which can be now approximated with simple terms in l, w -space. This terms were found by the means of linear regression and the resulting function are

$$c_{\text{eff}}(l, w) \approx w (C_0^{\text{eff}} + C_1^{\text{eff}} \cdot w + C_2^{\text{eff}} \cdot w^2 + C_3^{\text{eff}} \cdot w \cdot l) \quad (\text{S102})$$

with coefficients

$$\begin{aligned}
C_0^{\text{eff}} &= 2.36 \\
C_1^{\text{eff}} &= -1.58 \times 10^2 \text{ m}^{-1} \\
C_2^{\text{eff}} &= 4.71 \times 10^3 \text{ m}^{-2} \\
C_3^{\text{eff}} &= 8.47 \times 10^2 \text{ m}^{-2}
\end{aligned} \tag{S103}$$

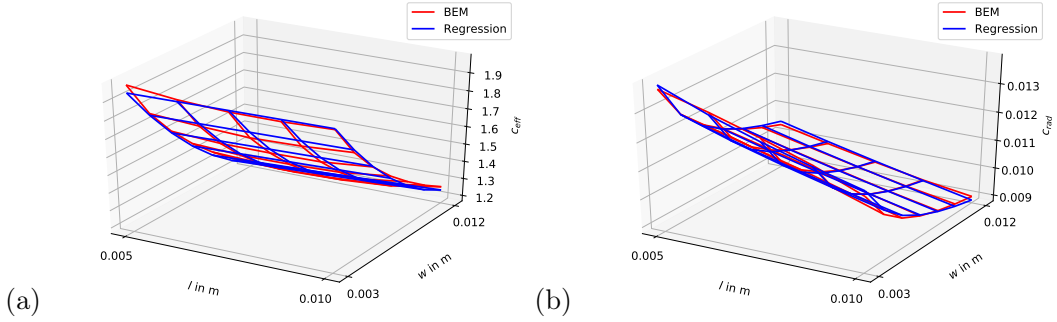
and

$$c_{\text{rad}}(l, w) \approx C_0^{\text{rad}} + \frac{C_1^{\text{rad}}}{\sqrt{w}} + C_2^{\text{rad}} \cdot l + \frac{C_3^{\text{rad}}}{w \cdot l} \tag{S104}$$

with coefficients

$$\begin{aligned}
C_0^{\text{rad}} &= 9.3 \times 10^{-3} \\
C_1^{\text{rad}} &= 2.32 \times 10^{-4} \sqrt{\text{m}} \\
C_2^{\text{rad}} &= -2.7 \times 10^{-1} \text{ m}^{-1} \\
C_3^{\text{rad}} &= 2.61 \times 10^{-8} \text{ m}^2
\end{aligned} \tag{S105}$$

These equations were optimized to have a minimal number of terms and to produce a maximum error of less than 3%. A comparison between the fitted functions with the numerically calculated results is shown in Fig. 3. These expressions are substituted into Eqs. (S98) and (S99) for calculation of the polarizability tensor for the resonator with one aperture.



Supplementary Figure 3. Results of nonlinear optimization and subsequent linear regression for c_{eff} (a) and c_{rad} (b) in l, w -space.

SUPPLEMENTARY NOTE 7:

TAILORING THE WILLIS COUPLING BY VARYING META-ATOM GEOMETRY

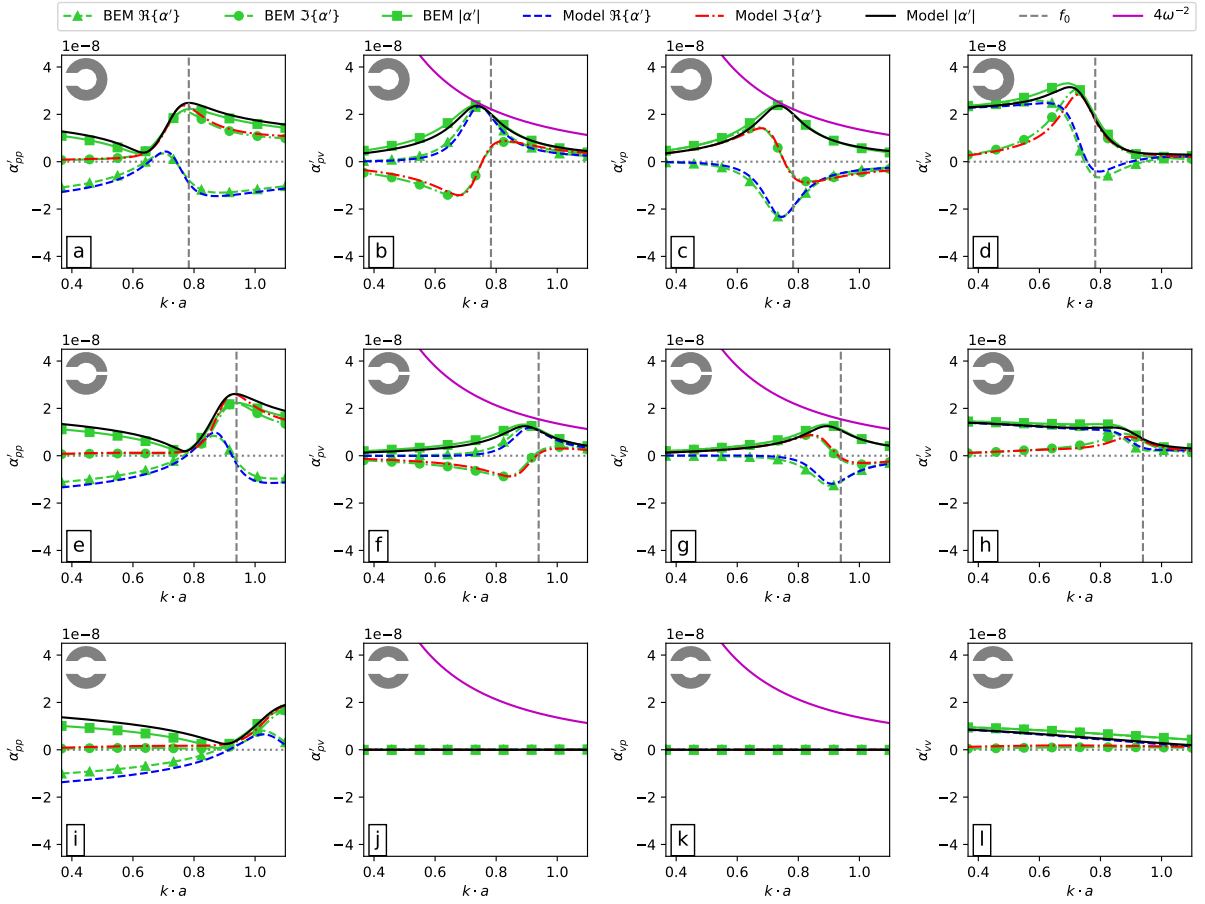
Here we demonstrate how Willis coupling can be tailored by controlling the geometric parameters of the meta-atom. First, a single aperture meta-atom with $\frac{w_1}{w_2} = \infty$ is considered, similar to the experimentally investigated sample. Fig. 4(a-d) illustrates the normalized polarizability components α'_{pp} , α'_{pv} , α'_{vp} , and α'_{vv} determined analytically (blue, red and black lines) and numerically (green lines with markers). Theoretical and numerical polarizabilities are in perfect agreement. The maximum magnitude of Willis coupling is reached, as shown by α'_{pv} and α'_{vp} touching the theoretical bound (magenta line) in Fig. 4(b,c).

Next, a meta-atom with the same parameters but an additional smaller aperture is considered ($\frac{w_1}{w_2} = 4$). The resulting polarizability is shown in Fig. 4(e-h), where theory perfectly matches the BEM results. Two important effects are observable. First, the eigenfrequency (and therefore the frequency of peak Willis coupling) is shifted, which can be understood through Eq. (S40). Second, the Willis coupling amplitude is reduced, see Fig. 4(f,g), since the asymmetry of the particle is weaker. Furthermore, the profile of α'_{pp} in Fig. 4(e) shows no significant difference from Fig. 4(a). In contrast, the profile of α'_{vv} is strongly reduced in amplitude close to the resonator eigenfrequency. The effect of decreased Willis coupling (see Fig. 4(f,g)) is of practical importance, since it can be used to tailor the Willis coupling to required values.

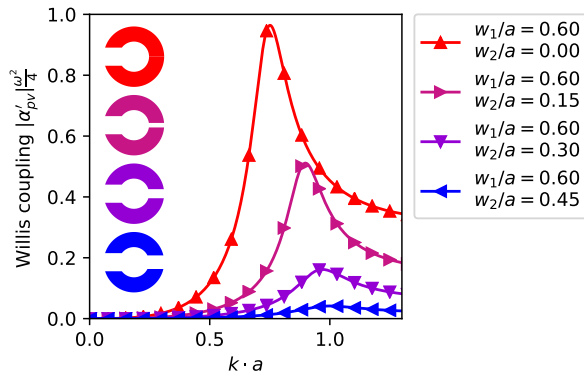
A special case is the symmetrical double aperture meta-atom, where $\frac{w_1}{w_2} = 1$. Its polarizability given in Fig. 4(i-l) differs significantly from the asymmetrical meta-atoms discussed above. The resonance frequency is further shifted due to the change of the resonator parameters (see Eq. (S40)). The Willis coupling is zero, which agrees with the expectations due to the symmetry of the structure. The α_{pp} component in Fig. 4(i) shows no significant change compared to previous parameter choices. Interestingly, α_{vv} no longer has a peak and moreover, it approaches the polarizability of a cylinder given by Eq. (S66). In this case two design points could be of interest, one in the peak of α_{pp} by $ka = 1.15$ and one in the zero dip of it by $ka = 0.75$ (see Fig. 4(i)). Especially in the zero dip, a regime with a dipole response of a cylinder, but without any or with extremely weak monopole response is obtained.

The ratio $\frac{w_1}{w_2}$ allows Willis coupling to be engineered, however changing the ratio of widths also shifts the peak frequency, as can be observed in Fig. 5. To obtain a meta-atom of the

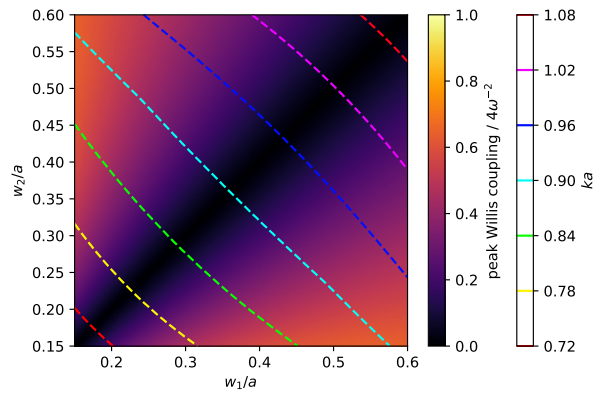
same size and with constant peak frequency varying only Willis coupling requires adjustment of additional parameters. This relation can be observed in Fig. 6, which considers neck widths in the range $0.15 \leq \frac{w}{a} \leq 0.6$. This range is limited to avoid very narrow slits which would lead to high thermo-viscous losses. The colored background refers to peak Willis coupling normalized to the theoretical bound and the contours illustrate the peak frequencies. Taking for example a meta-atom of size $a = 20$ mm: engineering of different Willis coupling peak magnitudes at $ka = 0.9$ equates to choosing w_1 and w_2 from Fig. 6 along the dashed teal like corresponding to $ka = 0.9$.



Supplementary Figure 4. Meta-atom polarizability determined by theory (blue, red and black lines) and numerically (green lines with markers): a, b, c, d: Single aperture meta-atom with $a = 20$ mm, $l = 10$ mm and $w = 12$ mm. e, f, g, h: Double aperture meta-atom with $a = 20$ mm, $l = 10$ mm and $w_1 = 12$ mm and $w_2 = 3$ mm. i, j, k, l: Symmetrical double aperture meta-atom with $a = 20$ mm, $l = 10$ mm and $w_1 = 3$ mm and $w_2 = 3$ mm.



Supplementary Figure 5. Willis coupling of four different meta-atom geometries through variation of w_2 . Peak Willis coupling and peak frequency are changed.



Supplementary Figure 6. Design space of double aperture meta-atom: Willis coupling normalized to the maximum bound as colored background and contour lines of peak frequencies as colored dashed lines.

SUPPLEMENTARY REFERENCES

1. Jordaan, J. *et al.* Measuring Monopole and Dipole Polarizability of Acoustic Meta-Atoms. *Applied Physics Letters* **113**, 224102. ISSN: 0003-6951 (Nov. 2018).
2. Quan, L., Ra'di, Y., Sounas, D. L. & Alù, A. Maximum Willis Coupling in Acoustic Scatterers. *Physical Review Letters* **120**. ISSN: 0031-9007, 1079-7114. doi:10.1103/PhysRevLett.120.254301. <https://link.aps.org/doi/10.1103/PhysRevLett.120.254301> (2018) (June 20, 2018).
3. Kinsler, L. E. *Fundamentals of acoustics* 568 pp. ISBN: 978-0-471-84789-2 (Wiley, 2000).
4. Crow, B. C., Cullen, J. M., McKenzie, W. W., Koju, V. & Robertson, W. M. Experimental realization of extraordinary acoustic transmission using Helmholtz resonators. *AIP Advances* **5**, 027114 (Feb. 1, 2015).
5. Dosch, H. G. Radiative feedback in Helmholtz resonators with more than one opening. *The Journal of the Acoustical Society of America* **140**, 3576–3581. ISSN: 0001-4966 (Nov. 1, 2016).